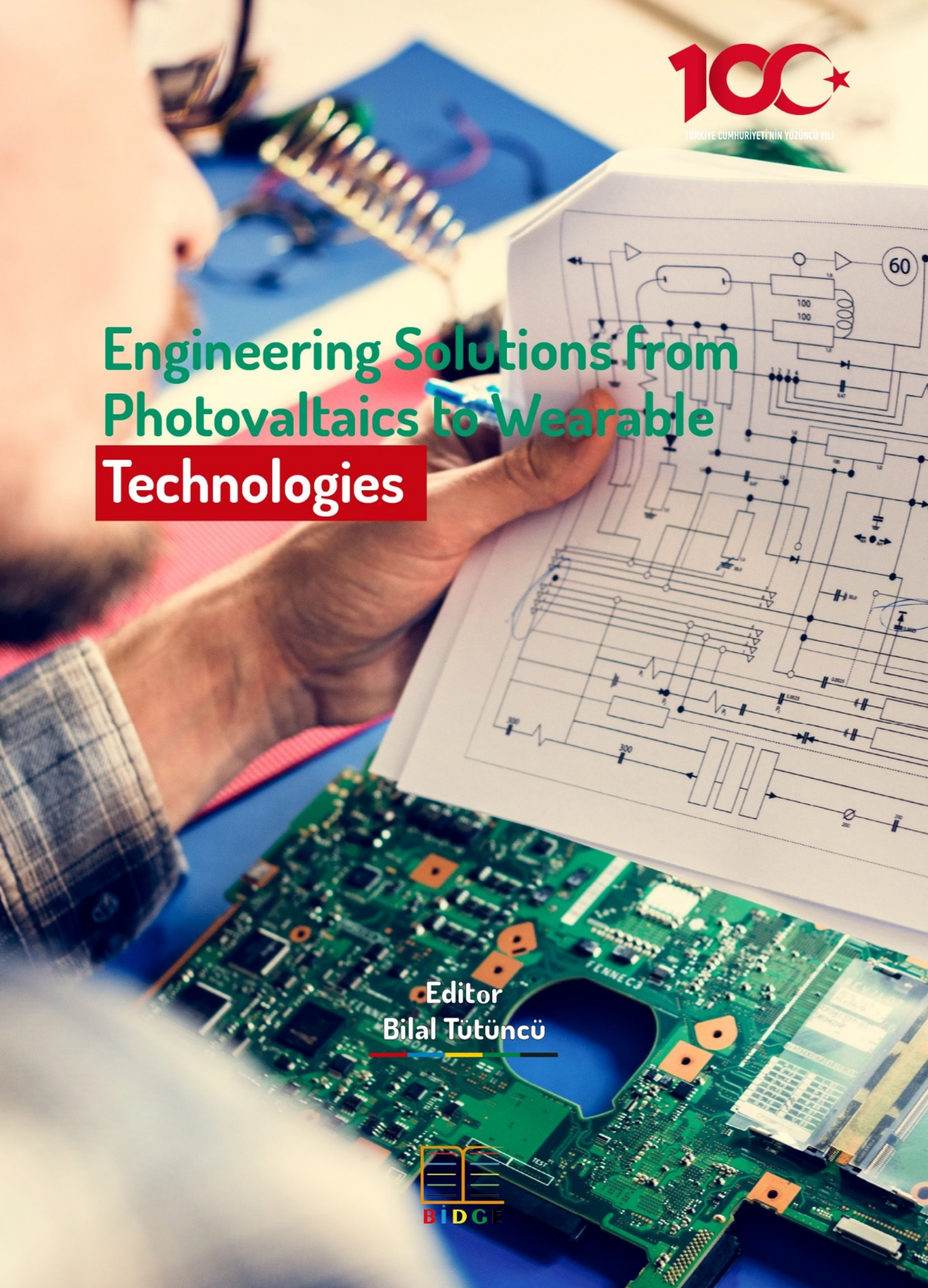

TÜRKİYE CUMHURİYETİ'NİN YÜZÜNCÜ YILI

Engineering Solutions from Photovaltaics to Wearable Technologies

Editor
Bilal Tütüncü

BİDGE

BIDGE Publications

Engineering Solutions from Photovaltaics to Wearable Technologies

Editor: Doç Dr. Bilal Tütüncü

ISBN: 978-625-372-569-3

Page Layout: Gözde YÜCEL

1st Edition:

Publication Date: 25.12.2024

BIDGE Publications,

Certificate No: 71374

www.bidgeyayinlari.com.tr - bidgeyayinlari@gmail.com

Krc Bilişim Ticaret ve Organizasyon Ltd. Şti.

Güzeltepe Mahallesi Abidin Daver Sokak Sefer Apartmanı No: 7/9 Çankaya / Ankara

Content

CHAPTER I

Experimental Obtaining of Temperature and Performance Analysis of Three-Phase Induction Motor Rotor Bar Failure

Asım Gökhan YETGİN[1]
Ahmet ÇİFCİ[2]

1. INTRODUCTION

Induction motors are ubiquitous in industrial settings, prized for their simple construction, robustness, low operational costs, ease of maintenance, high efficiency, and reliability (Singh et al., 2016). Squirrel cage induction motors, representing 90% of all electric motors, dominate the industrial landscape as the primary means of converting electrical energy into mechanical energy (Chisedzi & Muteba, 2023). These motors are produced across a wide power spectrum, from small wattage to megawatts, finding application in diverse fields (Wu et al., 2022), including hazardous environments

[1] Assoc. Prof. Dr., Burdur Mehmet Akif Ersoy University, Faculty of Engineering and Architecture, Department of Electrical and Electronics, Burdur/Türkiye, Orcid: 0000-0003-3971-0504, agyetgin@mehmetakif.edu.tr

[2] Asst. Prof. Dr., Burdur Mehmet Akif Ersoy University, Faculty of Engineering and Architecture, Department of Electrical and Electronics, Burdur/Türkiye, Orcid: 0000-0001-7679-9945, acifci@mehmetakif.edu.tr

such as oil refineries and blower installations (Chisedzi & Muteba, 2023). Common applications include pumps, conveyors, machine tools, centrifugal machines, presses, elevators, packaging equipment, petrochemical and natural gas plants, grain elevators, shredders, and coal plants (Kathir, Balakrishnan & Manikandan, 2014).

Despite their inherent robustness, prolonged exposure to harsh operating conditions can lead to the degradation of induction motors. Early fault detection and diagnosis are crucial for mitigating the impact on productivity and minimizing financial losses (Vanga et al., 2023). Incipient faults are often asymptomatic but can lead to significant issues, including production line interruptions, damage to adjacent machinery, and, in severe cases, complete system failure, resulting in substantial economic consequences (Maloma, Muteba & Nicolae, 2017). Even minor faults can reduce efficiency, increase operating temperature (leading to reduced insulation lifespan), elevate vibration levels, and shorten bearing life (Chehaidia et al., 2022).

Faults in electric motors can be broadly classified into five categories: stator faults, stator winding connection faults, eccentric faults, rotor bar faults, and bearing and gearbox faults (Bahgat, Elhay & Elkholy, 2024). Additional fault types include overload, single-phase drop, unbalanced supply, locked rotor, ground fault, overvoltage, and undervoltage (Kolla & Varatharasa, 2000). These faults manifest in various ways, including motor overheating, vibration, noise, and changes in motor current signatures. Therefore, early detection and accurate identification of these faults are critical for implementing timely maintenance strategies, preventing catastrophic failures, and ensuring optimal machine performance (Bahgat, Elhay & Elkholy, 2024).

According to the Electric Power Research Institute (EPRI), the distribution of failures in induction motors is as follows: 41% bearing faults, 36% winding faults, 9% rotor faults, and 14% other faults. Similarly, the Motor Reliability Working Group of IEEE-IAS reports these figures as 44%, 26%, 8%, and 22%, respectively

(Umap & Bobade, 2020). Faults in induction motors are further categorized as either internal or external (Bahgat, Elhay & Elkholy, 2024). The types of faults found in induction motors are detailed in Figure 1 of the source, though not specified here (Bahgat, Elhay & Elkholy, 2024).

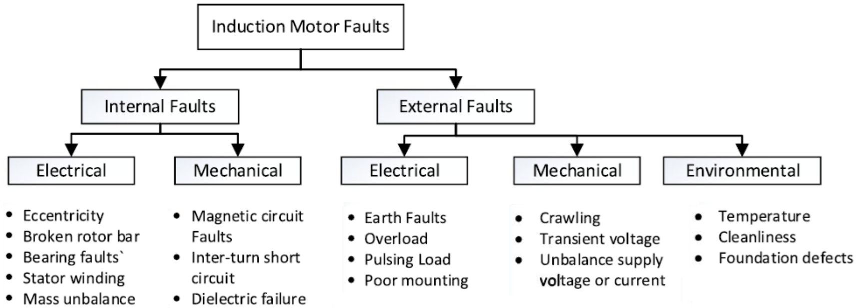

Figure 1: Induction motor fault types

Early detection and diagnosis of motor faults will help prevent larger problems. There are many methods to detect faults in induction motors. Some of these are measurement of magnetic flux, measurement of vibration, measurement of noise/acoustic noise, surge test and motor current signature analysis (Kathir, Balakrishnan & Ganesan, 2012)

Other common approaches to fault detection are the use of signal processing techniques. Among the various approaches examined, one can resort to the use of time-frequency representations, time scale analysis, polynomial phase transformation, Hilbert transform, Concordia transform, supply voltage modulation analysis, center of mass analysis, statistical moment analysis, and principal component analysis. In addition, artificial neural networks, fuzzy logic and expert systems are used in motor fault detection (Pires et al., 2012).

2. INDUCTION MOTOR FAULTS

Operational electrical or mechanical faults in induction motors often result in asymmetrical operating conditions. Rotor faults, a common issue in these motors, are broadly categorized as either mechanical or electrical in nature. While mechanical faults occur more frequently, electrical asymmetries within the rotor cage pose a significant diagnostic challenge due to the inaccessibility of rotor current measurements during operation (Nemec et al., 2016). Although initial symptoms of induction motor failures may be subtle, they can precipitate substantial problems, including reduced efficiency, increased energy consumption, degraded performance, and accelerated long-term deterioration of motor components (Kathir, Balakrishnan & Manikandan, 2014). The following section details the commonly encountered faults in induction motors.

2.1. Eccentricity Faults

Eccentricity faults in induction motors arise from variations in the air gap between the stator and rotor during operation. These faults are responsible for a significant portion, approximately 80%, of mechanical failures in these motors. An eccentric rotor induces excessive mechanical stress, ultimately leading to bearing fatigue. While manufacturers strive to minimize asymmetry during production and assembly, inherent imperfections persist. As illustrated in Figure 2, eccentricity faults can be categorized into three types: static eccentricity, dynamic eccentricity, and a combination of both, referred to as mixed eccentricity.

Static eccentricity is characterized by a constant air gap length as the rotor rotates, but with an uneven distribution of the gap at different radial positions, as depicted in Figure 2(b). Dynamic eccentricity, on the other hand, is defined by a periodically fluctuating air gap at a fixed circumferential location, as shown in Figure 2(c). Mixed eccentricity, representing a combination of both static and dynamic eccentricity, is illustrated in Figure 2(d) (Li et al., 2021).

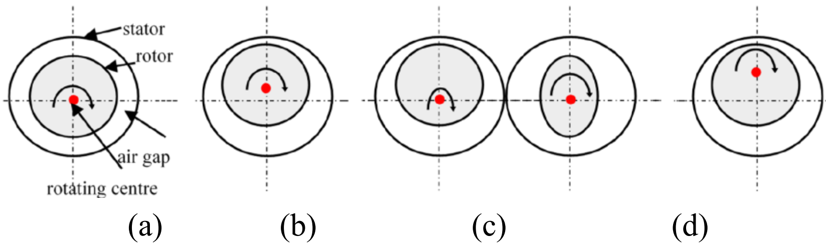

Figure 2: Axial eccentricity failures (a) healthy case (b) static eccentricity (c) dynamic eccentricity (d) mix eccentricity

Static eccentricity can be attributed to factors such as improper machine assembly or significant bearing wear. In this condition, the configuration of the air gap between the stator and rotor remains consistent along the stator circumference, regardless of whether the machine is at rest or in operation. This characteristic is visually represented in Figure 3 (Petryna, Duda & Sulowicz, 2021).

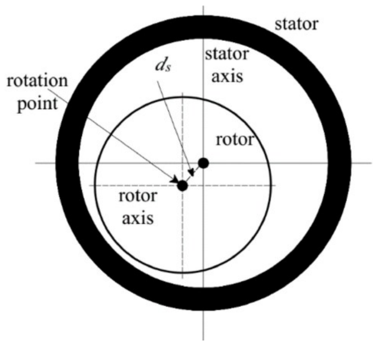

Figure 3: Static eccentricity

The possible negative effects of static eccentricity are:

• Shaft torque decreases

• Unbalanced magnetic tension forces occur

In contrast to static eccentricity, during dynamic eccentricity, the position of the minimum air gap width shifts along the stator circumference as the machine operates. This dynamic behavior is illustrated in Figure 4 (Petryna, Duda & Sulowicz, 2021).

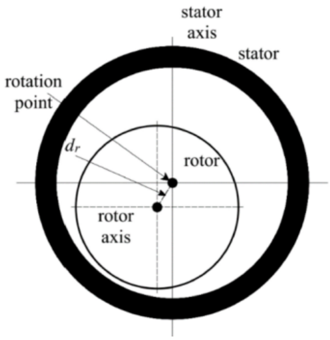

Figure 4: Dynamic eccentricity

2.2. Bearing and Gear Failure

The primary factors contributing to bearing failures are contamination and corrosion. Given that induction motors are frequently deployed in harsh environments, they are often exposed to detrimental elements such as foreign materials, water, acids, and moisture, which significantly contribute to bearing degradation. In such industrial settings, contamination and corrosion accelerate bearing failures. Contamination, often in the form of dirt and other foreign materials, infiltrates the bearing lubrication. These particles, ranging in hardness from relatively soft to diamond-like, possess an abrasive nature that leads to pitting and abrasion, causing measurable wear on the bearing balls and raceways. Corrosion, on the other hand, can be initiated by exposure to water, acids, degraded lubrication, and even condensation resulting from improper handling during installation. As the chemical reaction progresses, it erodes particles, generating an abrasive effect similar to that caused by contamination (Önel & Benbouzid, 2008).

Bearing misalignment, shown in Figure 5 in four figures, is also a common result of faulty bearing assembly (Önel & Benbouzid, 2008).

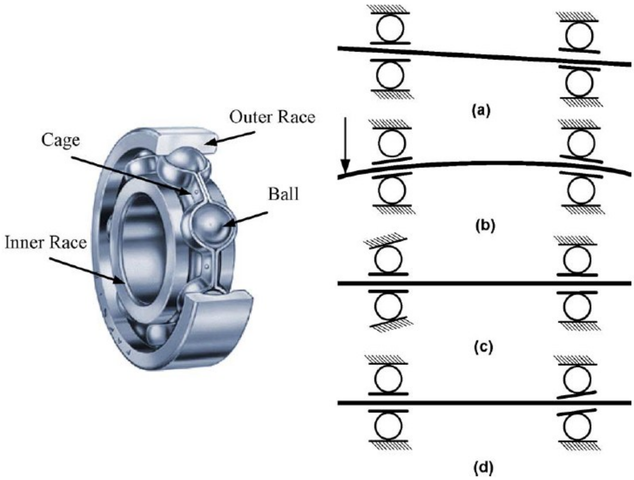

Figure 5: (a) Misalignment (out of line) (b) shaft deflection (c) bent or tilted outer ring (d) bent or tilted inner ring

2.3. Winding Failures

Stator winding faults can be categorized into five distinct types: winding-to-winding, coil-to-coil, line-to-ground, line-to-line, and open circuit faults. Among these, winding-to-winding faults, also known as stator turn faults, are considered the most problematic, as they often cascade into other fault types (Shashidhara & Raju, 2013). Figure 6 visually depicts the various winding faults that can occur within stator windings.

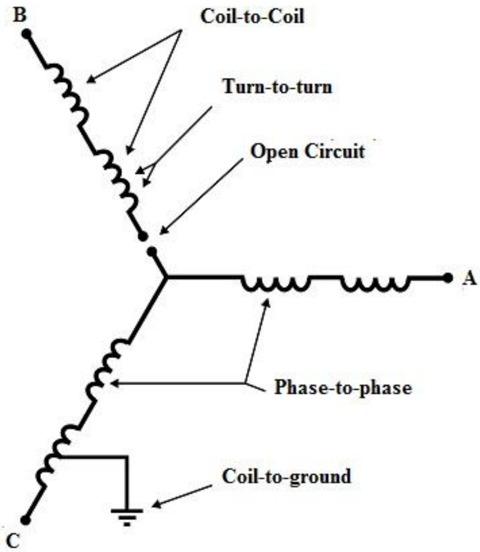

Figure 6: Winding failures

Stator winding faults are intrinsically linked to the degradation of stator winding insulation. These faults can be triggered by insulation failure between two turns within the same phase, between coils within the same phase, between two different phases, or between a phase and ground. Such failures lead to current imbalances, causing excessive current in the affected phase and impacting the remaining phases. This significant current imbalance is coupled with thermal stresses that further degrade the stator winding insulation and electrodynamic stresses that affect the end winding bonding and stator wedging, ultimately compromising the motor's reliability (Kocman & Nowak, 2019).

2.4. Broken Rotor Bar Failure

The presence of broken rotor bars (BRBs) raises safety concerns, reduces torque output, and destabilizes motor operation (Misra et al., 2022). BRB failures can be attributed to a multitude of factors, including mechanical, thermal, residual, environmental, or dynamic stresses. In squirrel cage induction motors, an undetected BRB failure leads to current redistribution from the broken bar to adjacent healthy bars, causing an increase in current flow within them. This can generate electric arcs and elevate temperatures, potentially melting these bars and causing further rotor damage. Consequently, the production line is negatively impacted, resulting in economic losses (Chisedzi & Muteba, 2023).

Furthermore, the centrifugal forces generated during motor rotation can dislodge small fragments of broken rotor bars, which, upon contact, can damage the stator winding and lamination. Additionally, adjacent broken bars cause uneven heating of the rotor bars, potentially leading to eccentricity and an unbalanced magnetic pull, which, in turn, can induce further rotor bar breakage and increase the nominal current due to the increased load on the adjacent bars. This results in a decreased average torque value (Misra et al., 2022).

BRB failures also contribute to increased core losses due to localized saturation. When a rotor bar breaks, the current that would normally flow through it is diverted to adjacent bars, causing current fluctuations in the neighboring bars. This induces an asymmetrical magnetic field. As expected, an increase in the number of broken rotor bars corresponds to a rise in core losses and stator copper losses, while rotor copper losses decrease. Consequently, the total losses of the induction motor increase with the rising number of broken rotor bars (Faiz & Takbash, 2013).

Although broken rotor bars may not immediately cause a squirrel cage induction motor to fail, they can trigger severe secondary effects, such as asymmetrical rotor operation leading to unbalanced currents, torque pulsations, increased losses, and a reduction in average torque (Muteba, 2023). Visual representations of varying numbers of broken rotor bar failures are provided in Figure 7.

Figure 7: Rotor structures with different broken bar numbers (Liu et al., 2022)

Other types of faults that may occur in asynchronous motors are normal output, overload, overvoltage, low voltage, single phase drop, voltage imbalance. These faults may cause the temperature of the motor to increase, abnormal noise, vibrations and decrease in motor performance (Vanga et al., 2023).

3. MATERIAL AND METHODS

In this section, a failure was created in the rotor bars of a three-phase squirrel cage induction motor with 1, 2 and 3 broken bars. The results obtained for each faulty case were compared with the healthy motor. The performance analyses of each motor were obtained by performing no-load operation, short-circuit operation and loaded operation tests of the healthy and faulty motors. In addition, motor temperatures were recorded and compared with a thermal camera during each operation.

The experimental setup used is given in Figure 8 (a), and the experimental connection diagram is given in Figure 8 (b).

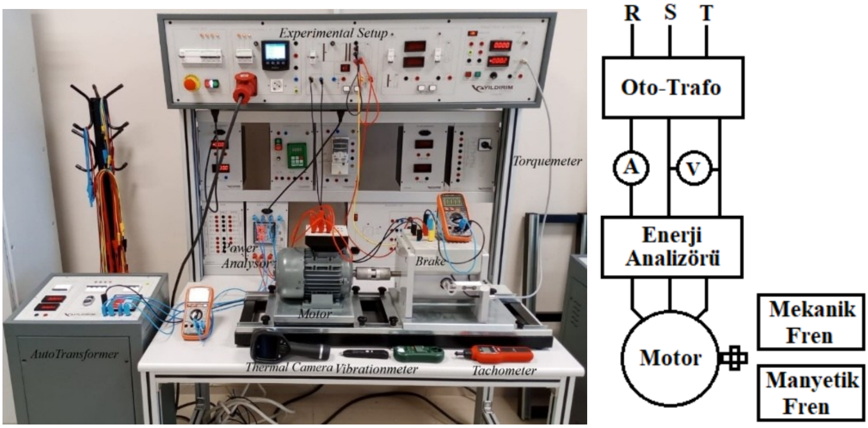

(a) (b)

Figure 8: a) Experimental connection setup b) experimental connection diagram

In the experiments, a FLIR E5 model thermal camera, a magnetic powder brake for the load, tachometer, a power analyzer, an autotransformer and measuring instruments were used.

The no-load tests were performed at the nominal voltage of 400 volts. The short-circuit tests were performed at the nominal current of 2.5 Amperes. The loaded tests were performed at the nominal voltage of 400 volts and the motor was loaded to full load.

The nameplate values of the motor used are given in Table 1.

Table 1: Nameplate of the motor used

Parameters	Values
Voltage	400 V
Frequency	50 Hz
Connection	Star
Current	2.5 A
Power	1100 W
Speed	1415 rpm
Pole pair	2

The image of the motor used in the experiments is given in Figure 9(a), the stator structure of the healthy motor is given in

Figure 9(b) and the rotor structure of the healthy motor is given in Figure 9(c).

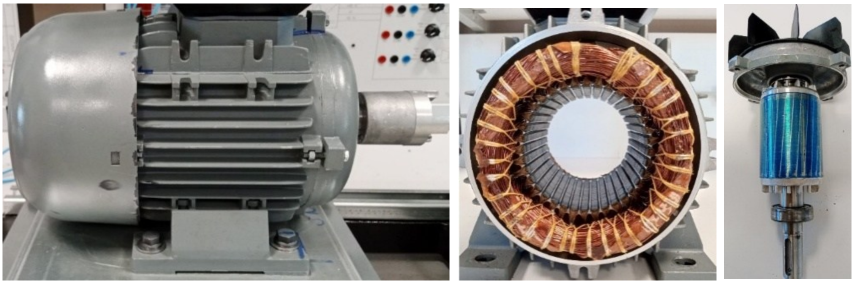

(a) (b) (c)

Figure 9: a) Motor used in experiments b) stator structure c) rotor structure

The 1, 2 and 3 broken rotor motors created in the study are given in Figure 10. The diameter of the broken bar created is 6 mm and their depth is as deep as the slot depth. In addition, the brokens were created as complete brokens.

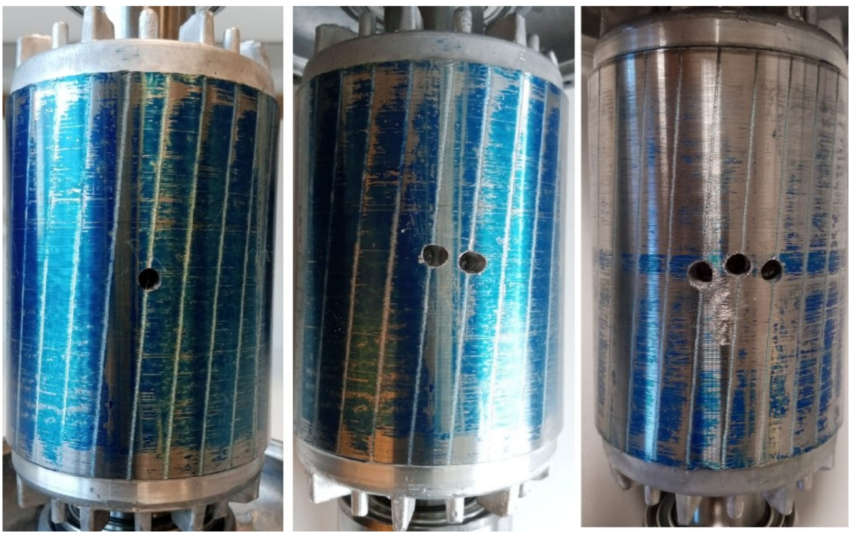

Figure 10: Created 1, 2 and 3 broken rotor structures

The equations given below are used to obtain the parameters (impedance, equivalent resistance, equivalent reactance, iron resistance and magnetization reactance) in the single-phase equivalent circuit model of the induction motor.

The single-phase equivalent circuit model of the induction motor is given in Figure 11.

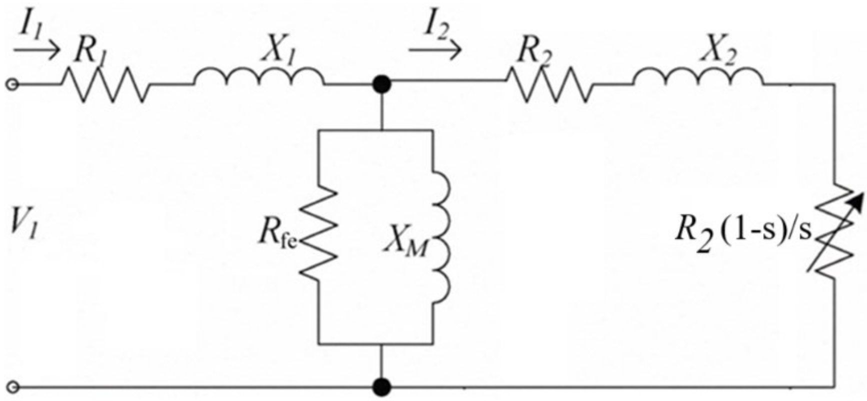

Figure 11: Induction motor single phase equivalent circuit (Lee et al., 2012)

The equivalent impedance (Z_k) value is obtained by Equation (1). Here V_k is the short circuit voltage and I_k is the short circuit current.

$$Z_k = \frac{V_k}{I_k} \tag{1}$$

The equivalent resistance value (R_k) is found in Equation (2) using copper losses (P_k) and short circuit current.

$$P_k = 3 * \mathrm{I_k}^2 * R_k \tag{2}$$

The equivalent reactance (X_k) value is calculated with the help of Equation (3).

$$X_k = \sqrt{Z_k^{\,2} - R_k^{\,2}} \tag{3}$$

After calculating the impedance, equivalent resistance and equivalent reactance values of the motor, the stator and rotor resistances (R_1, R_2) and leakage reactance (X_1, X_2) values are calculated as follows.

$$R_1 = R_2 = \frac{R_k}{2} \tag{4}$$

$$X_1 = X_2 = \frac{X_k}{2} \tag{5}$$

With the help of the data obtained from the no-load test, the iron resistance (R_{fe}) and magnetization reactance (X_m) are calculated and are given in Equations (6) and (7), respectively. In the equations, P_{fe} represents the iron losses, V_1 represents the voltage applied to the stator, and I_0 represents the no-load current.

$$P_{fe} = \frac{3 * V_1^2}{R_{fe}} \tag{6}$$

$$X_m = \frac{V_1}{I_o * \text{Sin}\,\varphi_0} \tag{7}$$

4. OBTAINED RESULTS

In this section, the values obtained as a result of the experiments of healthy and broken rotor motors are given in two parts: performance analysis and thermal analysis.

4.1. Performance Analysis

Each motor was tested under no-load operation, short-circuit operation and loaded operation. The results obtained are given below for comparison. Load operation tests were performed at nominal voltage and magnetic powder brake was used as the load.

Table 2: Results of no-load test of healthy and 1, 2 and 3 broken rotor motors

Experiments	Current [A]	Voltage [V]	Power [W]	Speed [rpm]	Power Factor
Healthy Motor	1.79	400	112	1499.3	0.09
1 BRB	1.82	400	114	1499.4	0.09
2 BRB	1.84	400	127	1499.1	0.1
3 BRB	1.87	400	130	1499	0.1

When Table 2 is examined, it is seen that as the number of broken bar increases, there is a slight increase in the no-load current and accordingly an increase in iron losses. It is seen that the power factor values are close to each other.

Table 3: Short circuit operation test results of healthy and 1, 2 and 3 broken rotor motors

Experiments	Current [A]	Voltage [V]	Power [W]	Power Factor
Healthy Motor	2.5	70.7	189	0.62
1 BRB	2.5	73.9	198	0.62
2 BRB	2.5	74.6	200	0.62
3 BRB	2.5	74.9	204	0.63

When Table 3 is examined, there is a slight increase in copper losses. It is seen that the power factor value does not change, and the short circuit voltage value increases slightly as the number of broken rotors increases. It is seen that there is an increase in the total of iron and copper losses, which will result in more heating of the motor and a significant decrease in efficiency.

Loaded operation tests for each motor were conducted at a nominal voltage of 400 volts. Loading was performed using a magnetic powder brake. Each motor was loaded at a nominal full load value. The obtained speeds were around 1420 rpm.

The impedance, equivalent resistance and equivalent reactance values calculated using the values obtained from the no-load and short-circuit test results are given in Figure 12. The changes in iron resistance and magnetization reactance are given in Figure 13.

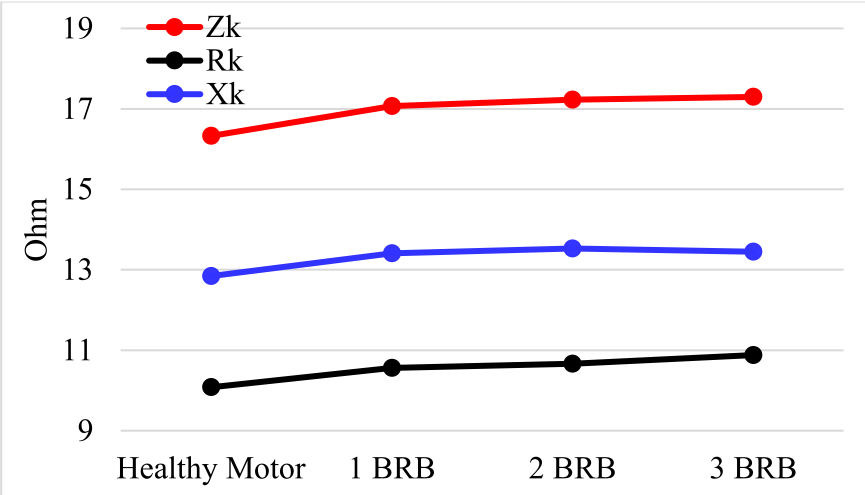

Figure 12: Impedance, resistance and reactance changes of healthy and broken rotor motors

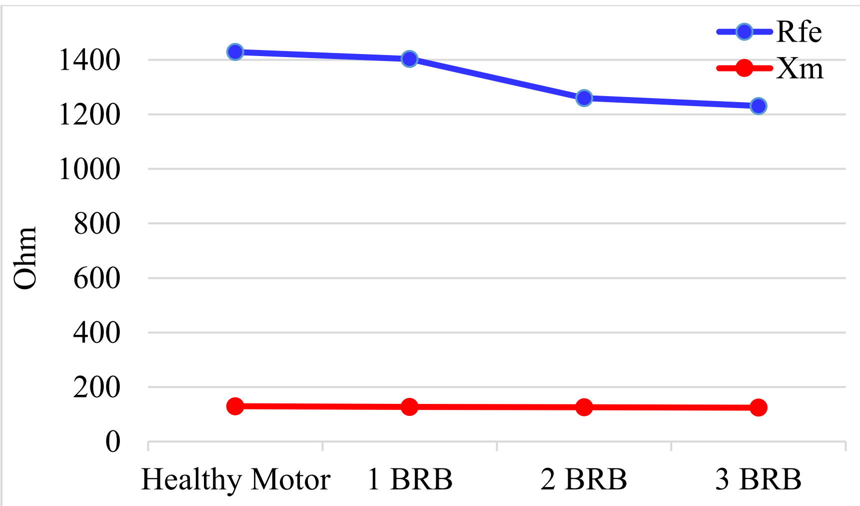

Figure 13: Iron resistance and magnetization reactance changes of healthy and broken rotor motors

When Figure 12 is examined, it is seen that the impedance, equivalent resistance and equivalent reactance values increase with the increase in the number of broken bars in the rotor. In Figure 13, it is seen that both the iron resistance and the magnetization reactance tend to decrease.

Another important parameter in the performance evaluation of the induction motor is the efficiency analysis. The efficiency changes obtained using the loss power values obtained from the experiments are given in Figure 14. When the figure is examined, it is seen that the efficiency value decreases with the increase in the number of broken rotors bars. It is seen that the efficiency value of the motor with 3 broken rotor bars decreases by 2.3% compared to the healthy motor.

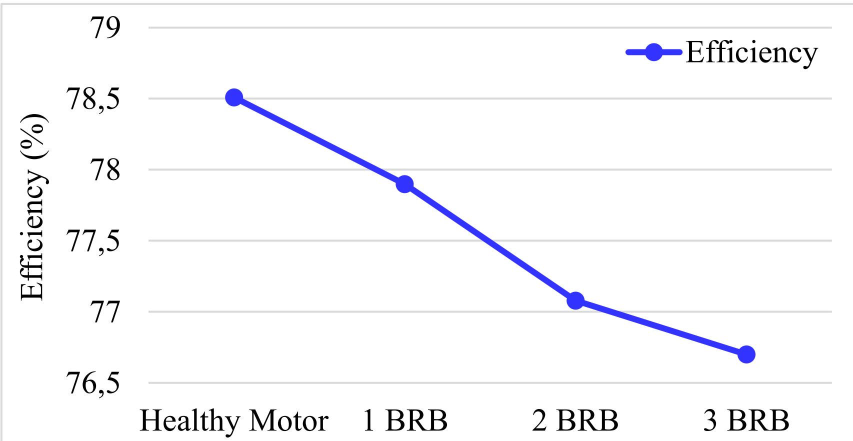

Figure 14: Efficiency changes of healthy and broken rotor motors

4.2. Thermal Analysis

An increase in temperature in induction motors can lead to failures in the machine and a decrease in useful life. Therefore, the thermal behavior of the induction motor is considered a critical criterion on the basis of which the motor is selected. It becomes very important to predict the temperature behavior at the critical points of the induction motor (Cabral & Adouni, 2020).

The lifespan of an induction motor is contingent upon a multitude of factors, including operational load, duty cycle, environmental stressors, installation practices, temperature distribution, and manufacturing imperfections. Elevated motor temperatures can lead to significant issues and ultimately result in motor failure. Given their widespread use in applications such as electric vehicles, hybrid electric vehicles, chillers, land and marine propulsion systems, fans, mills, extruders, brake release mechanisms, compressors, shredders, crushers, blowers, and cranes, induction motors are subjected to various operating conditions. The annual failure rate for induction motors is typically between 3-5%, while for large industrial motors, this rate climbs to 12%. A substantial portion of these failures is attributed to the continuous heating of various motor components during operation. Thermal analysis has demonstrated that a majority of motor failures are either directly or indirectly linked to the sustained heating of various motor parts during operation. Overheating leads to the degradation of stator insulation and alterations in the rotor resistance value (Sudha et al., 2020).

Temperature changes were obtained during the no-load operation, short-circuit operation and loaded operation experiments of the healthy motor, 1, 2 and 3 broken rotor motors. A Flir E5 camera was used to take thermal images. The temperature values in the section where the maximum temperature value was located were taken into account in the measurements. The measurements were taken by leaving a fixed distance from the setup where the experiments were carried out, and the same distance was maintained for each experiment.

In thermal measurements, no-load and loaded tests were performed for 30 minutes. However, due to the high current in short circuit tests, the tests were performed to end in 60 seconds. The time scale in the graphs was drawn by taking these periods into account.

Thermal images obtained from the no-load operation test are given in Figure 15 (a-d) for the healthy motor and the motor with broken rotor.

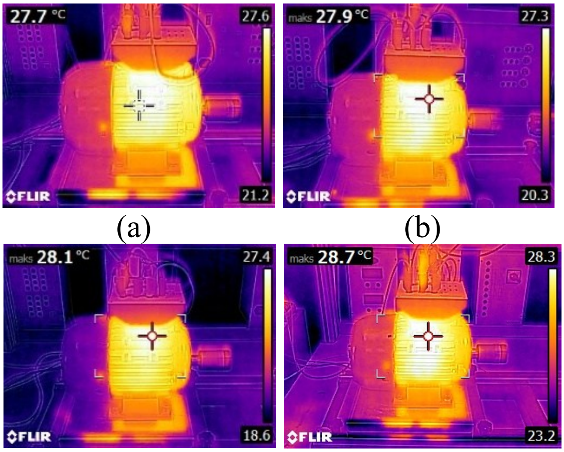

(a) (b)

(c) (d)

Figure 15: Thermal images obtained from the no-load test a) healthy motor b) motor with 1 broken c) motor with 2 brokens d) motor with 3 brokens

Thermal images obtained from the short circuit test are given in Figure 16 (a-d) for the healthy motor and the motor with broken rotor.

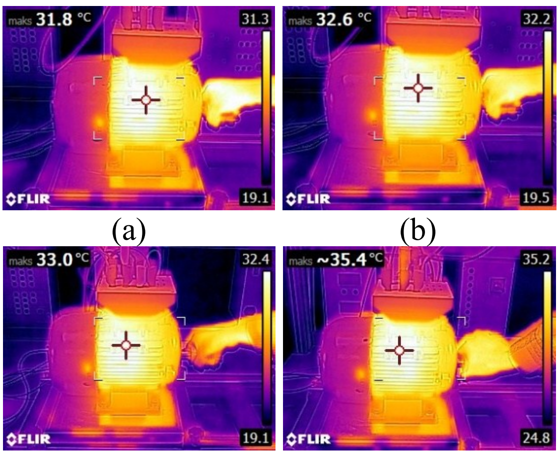

(a) (b)

(c) (d)

Figure 16: Thermal images obtained from the short circuit operation test a) healthy motor b) motor with 1 broken c) motor with 2 brokens d) motor with 3 brokens

Thermal images obtained from the loaded operation test are given in Figure 17 (a-d) for the healthy motor and the motor with broken rotor.

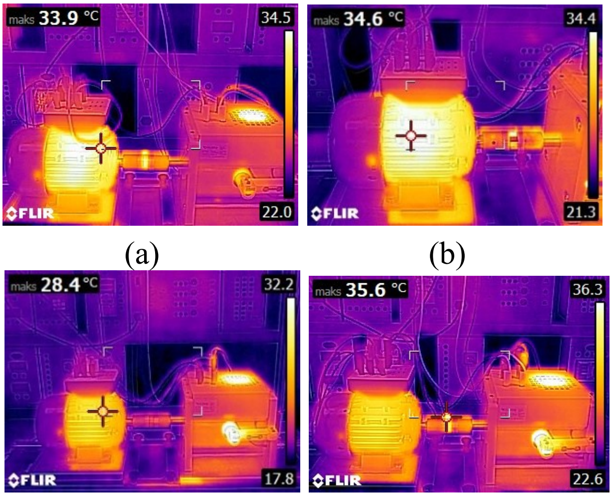

(a) (b)

(c) (d)

Figure 17: Thermal images obtained from the loaded operation test a) healthy motor b) motor with 1 broken c) motor with 2 brokens d) motor with 3 brokenss

The time-temperature changes obtained from the no-load operation test of the healthy motor and the motors with 1, 2 and 3 broken rotors are given in Figure 18. It is understood that the initial temperatures in the experiments were around room temperature and the temperature values in the motors increased as time progressed. The test period was limited to 30 minutes. It is seen that the motor temperature values increased as the number of broken bars increased. It was determined that the temperature change of the motor with 3 broken bars increased by 5.244% compared to the healthy motor in the 30th minute.

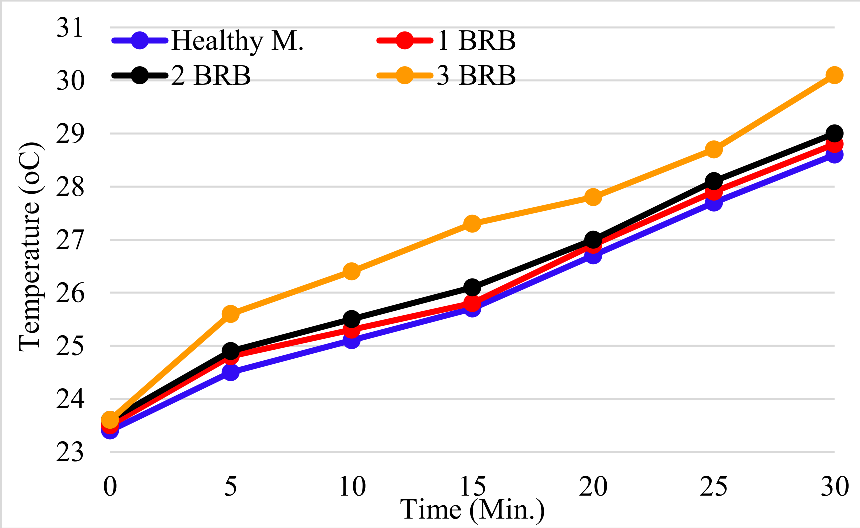

Figure 18: Time-temperature variations obtained from the no-load test for healthy and broken rotor motors

Figure 19 shows the time-temperature changes during the loaded operation tests of healthy and broken rotor motors. The loaded operation tests were limited to 30 minutes. It is seen that the temperature values increase rapidly in the loaded operation tests. Again, it shows that the 3 broken bar motor increased by 6.199% compared to the healthy motor in the 30th minute.

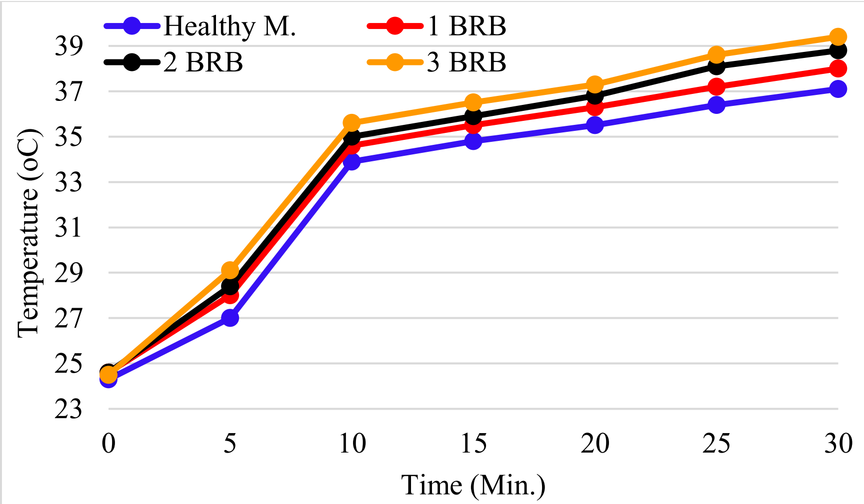

Figure 19: Time-temperature variations obtained from the loaded operation test for healthy and broken rotor motors

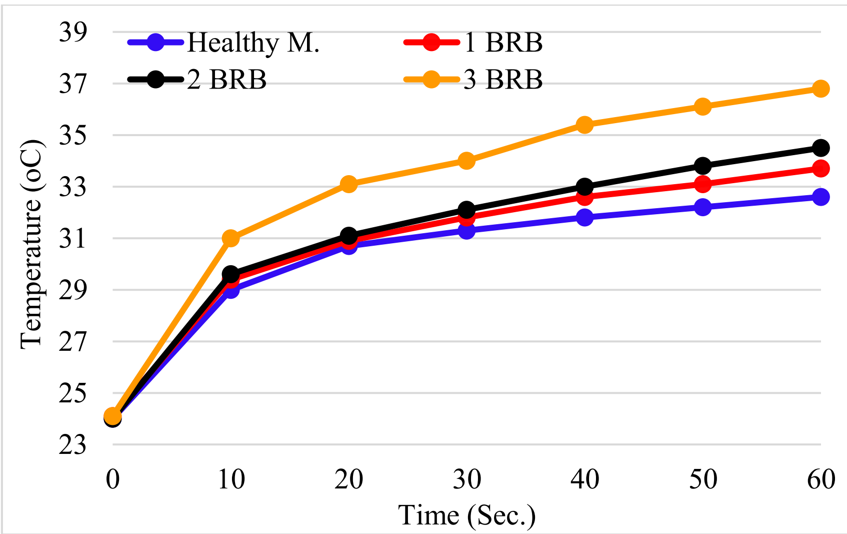

Figure 20: Time-temperature variations obtained from short circuit operation test for healthy and broken rotor motors

In Figure 20, the temperature changes in the short circuit operation test for each motor are given. Here, due to the high current values, the experiments were completed within 60 seconds. When Figure 20 is examined, it is seen that the high current value during the short circuit test caused the temperature values to be high. It is seen that the rapid increase in the current value in the short circuit test caused the temperature values to increase rapidly after the 10th second. Again, it is seen that the temperature values in the 3 broken bar motor are higher than the healthy, 1 and 2 broken bar motors. It is also seen that the temperatures in the short circuit test reach the temperature values in the loaded operation before 1 minute is up.

5. CONCLUSION

Three-phase squirrel cage induction motors are the most commonly used motors in industrial applications. Despite their robust structure, motor failures can occur over time due to both external and internal effects. One of the most important of these failures is the broken rotor bar failure. Early detection of these failures will help prevent further growth of the failure and will contribute to the prevention of financial losses for the business.

In the study, faults were created in the rotor section of a three-phase squirrel cage induction motor in such a way that there would be 1, 2 and 3 broken rotor bars. Both performance and thermal analyses of the faulty motors and the healthy motor were performed. In this context, operation, short circuit operation and loaded operation experiments were performed, and performance analyses were performed for each motor. Thermal images of each motor were also obtained and compared during the experiments.

The results obtained showed that with the increase in the number of broken rotor bars, the iron and copper losses of the motor increased, and as a result, the motor efficiency decreased. The resistance and reactance values increased depending on the number of broken bars. As a result of the thermal analysis, it was observed that the temperature values obtained in the no-load and loaded operation experiments increased as the number of broken rotor bars increased.During short circuit operation, it was observed that the temperature values increased rapidly due to the high current value, and again depending on the number of broken bars, the temperatures were higher than in the healthy motor.

"This study was supported by Burdur Mehmet Akif Ersoy University Scientific Research Projects Commission. Project Number: 0821-MP-22"

6. REFERENCES

Bahgat, B. H., Elhay, E. A. & Elkholy, M. M. (2024). Advanced fault detection technique of three phase induction motor: comprehensive review. *Discover Electronics*, *1*(9), 1-25.

Cabral, P. & Adouni, A. (2020). Induction motor thermal analysis based on lumped parameter thermal network. *In International Congress on Engineering - Engineering for Evolution, KnE Engineering*, 2020, 451–464.

Chehaidia, S. E., Cherif, H., Alraddadi, M., Mosaad, M. I. & Bouchelaghem, A. M. (2022). Experimental diagnosis of broken rotor bar faults in ınduction motors at low slip via hilbert envelope and optimized subtractive clustering adaptive neuro-fuzzy ınference system. *Energies*, 15, 1-22.

Chisedzi, L. P. & Muteba, M. (2023). Detection of broken rotor bars in cage induction motors using machine learning methods. *Sensors*, *23*, 1-13.

Faiz, J. & Takbash, A. M. (2013). Derating of three-phase squirrel-cage inductıon motor under broken bars fault. *Facta Unıversitatis Series: Automatic Control and Robotics*, *12*(3), 147-156.

Kathir, I., Balakrishnan, S. & Manikandan, B. V. (2014). Broken rotor bar detection using high frequency loss calculation of induction motor. *Applied Mechanics and Materials*, 573, 728-733.

Kathir, P. I., Balakrishnan, S. & Ganesan, S. (2012). Detection of rotor fault in an induction motor under standstill condition-a power quality perspective. *Procedia Engineering*, 38, 3200-3214.

Kocman, S. & Nowak, S. (2019). Analysis of the stator winding fault of induction motor using comsol multiphysics. *IEEE 20th International Scientific Conference on Electric Power Engineering (EPE)*, 15-17 May 2019, Kouty nad Desnou, Czech Republic, (pp. 1-6).

Kolla, S. & Varatharasa, L. (2000). Identifying three-phase induction motor faults using artificial neural networks. *ISA Transactions*, 39, 433-439.

Lee, K., Frank, S., Sen, P. K. Palese, L. G., Alahmad, M., Waters, C. & Durham, C. W. (2012). Estimation of induction motor equivalent circuit parameters from nameplate data. *IEEE North American Power Symposium (NAPS)*, 09-11 September 2012, Champaign, IL, USA, (pp. 1-6).

Li, H., Zou, Z., Sun, X., Gu, F. & Ball, A. D. (2021). A numerical study of rotor eccentricity and dynamic load in induction machines for motor current analysis based diagnostics. *Maintenance, Reliability and Condition Monitoring*, *1*(2), 71-86.

Liu, X., Yan, Y., Hu, K., Zhang, S., Li, H., Zhang, Z. & Shi, T. (2022). Fault diagnosis of rotor broken bar in induction motor based on successive variational mode decomposition. *Energies*, 15, 1-16.

Maloma, E., Muteba, M. & Nicolae, D. V. (2017). Effect of rotor bar shape on the performance of three phase induction motors with broken rotor bars. *IEEE International Conference on Optimization of Electrical and Electronic Equipment (OPTIM) & Intl Aegean Conference on Electrical Machines and Power Electronics (ACEMP)*, 25-27 May 2017, Brasov, Romania, (pp. 364-369).

Misra, S., Kumar, S., Sayyad, S., Bongale, A., Jadhav, P., Kotecha, K., Abraham, A. & Gabralla, L. A. (2022). Fault detection in induction motor using time domain and spectral imaging-based transfer learning approach on vibration data. *Sensors*, 22, 1-16.

Muteba, M. (2023). Analysis of a three-phase induction motor with a double-triple-layer stator winding configuration operating with broken rotor bar faults. *Machines*, 11, 1-20.

Nemec, M., Drobnic, K., Fiser, R. & Ambrozic, V. (2016). Simplified model of induction machine with broken rotor bars. *IEEE*

International Power Electronics and Motion Control Conference (PEMC), 25-28 September 2016, Varna, Bulgaria, (pp. 1085-1090).

Önel, I. & Benbouzid, M. (2008). Induction motor bearing failure detection and diagnosis: park and concordia transform approaches comparative study. *IEEE/ASME Transactions on Mechatronics*, *13*(2), 257-262.

Petryna, J., Duda, A. & Sułowicz, M. (2021). Eccentricity in induction machines-a useful tool for assessing its level. *Energies*, 14, 1-26.

Pires, V. F., Amaral, T. G., Foitol, D., Fiser, R., Ambrozicand, V. & Martins, J. F. (2012). Rotor fault diagnosis in ınduction motors using s-transform. *IEEE International Conference on Industrial Technology*, 19-21 March 2012, Athens, Greece, (pp. 749-754).

Shashidhara, S. M. & Raju, P. S. (2013). Stator winding fault diagnosis of three-phase induction motor by park's vector approach. *International Journal of Advanced Research in Electrical, Electronics and Instrumentation Engineering*, *2*(7), 2901-2906.

Singh, A., Grant, B., DeFour, R. Sharma, C. & Bahadoorsingh, S. (2016). A review of induction motor fault modeling. *Electric Power Systems Research*, 133, 191–197.

Sudha, B., Vadde, A., Manickavasagam, K. & Kadambi, G. R. (2020). Characterization of temperature and productive torque for frame squirrel cage induction motor. *Journal of Engineering Research EMSME*, Special Issue, 35-46.

Umap, A. A. & Bobade, C. M. (2020). Detection and classification of faults in induction motor using wavelet and fuzzy controller. *International Journal of Advance Research and Innovative Ideas in Education IJARIIE*, *6*(4), 674-691.

Vanga, J., Ranimekhala, D. P., Jonnala, S., Jamalapuram, J., Gutta, B., Gampa, S. R. & Alluri, A. (2023). Fault classification of three phase induction motors using bi-lstm networks. *Journal of Electrical Systems and Information Technology*, *10*(28), 1-15.

Wu, Y., Sun, S., An, Q. & Lie, X. (2022). Treatment strategy research on a squirrel-cage induction motor with broken rotor bar faults. *Sensors*, 22, 1-22.

CHAPTER II

Effect of Inertia Weight Variations on Particle Swarm Optimization for Controller Design

Hasan BAŞAK[1]
Kadri DOĞAN[2]

1. Introduction

The goal of the entire optimization process is to find the best possible outcomes. Meta-heuristic optimization methods are recommended when addressing NP-hard problems. These algorithms are effective instinctively. At least they can locate a workable, quick solution in the search space, while there is no assurance that they will always arrive at the optimal one (Aydilek et al. 2017). Numerous scientific domains make extensive use of meta-heuristic optimization techniques. Kennedy and Eberhart initially presented particle swarm optimization (PSO), a stochastic population-based technique. The PSO algorithm emulates the

[1] Asist. Prof. Dr., Artvin Çoruh University, Faculty of Engineering, Elektrical Electronics Engineering, Artvin/Turkiye, Orcid: 0000-0002-3724-6819, hasanbasak@artvin.edu.tr
[2] Assoc. Prof. Dr., Artvin Çoruh University, Faculty of Engineering, Basic Science, Artvin/Turkiye, Orcid: 0000-0002-6622-3122, dogankadri@artvin.edu.tr

behavior of swarms in nature. It imitates fish and bird swarm behaviors. When these creatures seek food or defend themselves against enemies, they display social behaviours. These swarm characteristics served as the inspiration for the particle swarm optimization technique. Swarms in PSO are made up of particles. Every particle has values for position, velocity, and optimum position. The swarm has a global best value and is made up of particles. These numbers are utilised to determine the particles' subsequent locations and velocities. As a result, the particles travel to the more ideal solution and the algorithm converges. The pace of convergence influences the quality of the results. The algorithm's run time may rise and fail to reach the global optimum if convergence is too slow. Otherwise, if the algorithm is very fast, this can cause it to get stuck at a local minimum.

PID controllers have consistently had a prominent position in industrial applications because of their low cost and simplicity of use. In a variety of domains, metaheuristic algorithms have emerged as strong strategies for PID controller tuning. In order to optimize the parameters of PID-based control mechanisms, researchers have looked into a variety of artificial intelligence approaches (Ekinci, Hekimoğlu & Izci (2021; Ayinla et al. (2024). In this study, we investigate different inertia weights, including constant, random, linearly decreasing, nonlinearly decreasing, and a weight based on the best global and local fitness values, for the controller design of a system.

2. Methodology

2.1. Particle swarm algorithm

The term "swarm intelligence" is used to define algorithms by drawing inspiration from the behaviours of animal colonies. The PSO algorithm is a swarm intelligence method used to solve optimization problems (Arumugam and Rao, 2008**.** The biggest advantage of the PSO algorithm is its simplicity in application because it only requires the adjustment of a few parameters. The

PSO algorithm consists of particles moving within a search space, and each particle represents a potential solution. Each particle's position vector, Pos_i, velocity vector, Vel_i, the position of the particle that has achieved the best objective function, $Pbest_i$, and the best particle position in the swarm, P_{gbest} are represented. In each update, the velocity of each particle is updated using the best position of the swarm and the particle as follows.

$$Vel_i\,(t+1) = wVel_i(t) + c_1r_1\big(Pbest_i(t) - Pos_i(t)\big) + c_2r_2(P_{gbest}(t) - Pos_i(t))) \tag{1}$$

$$Pos_i(t+1) = Pos_i(t) + Vel_i(t+1) \tag{2}$$

where inertia weight w has a significant influence on both discovery and extraction procedures of the PSO algorithm. The random values r_1 and r_2 fall between 0 and 1. The acceleration coefficients c_1 and c_2 establish the rate of acceleration that will be applied to each particle's social and cognitive values, respectively. The flowchart of the PSO algorithm is given in Figure 2.

2.2. Inertia weight approaches in PSO

The inertia weight w in Equation (1) plays a crucial role in the convergence profile of the PSO algorithm. (Shi and Eberhart, 1998) reported that the selection of a large inertia weight is necessary for global search, while a small inertia weight benefits local search. Furthermore, Van den Bergh (2001) analyzed the impact of w by setting $c_1 = c_2 = 0$. If w is greater than one, the particle will accelerate to a maximum velocity. If w is less than 1.0, the particle will slow down gradually until its velocity reaches zero.

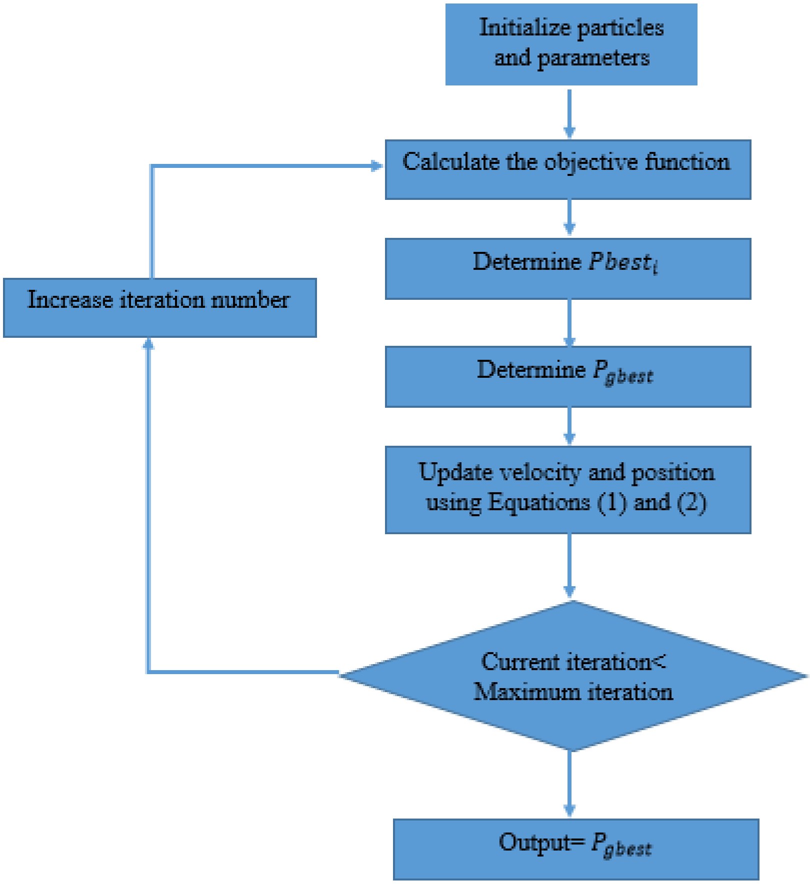

Figure 1: Flowchart of the PSO algorithm.

As a result, the choice of inertia weight influences the convergence and efficiencies of the PSO. Different inertia weight approaches are proposed in the literature and a list of inertia weights can be found in (Nickabadi, Ebadzadeh & Safabakhsh, 2011). We present some of the inertia weights in Table I. The constant inertia weight is set to 0.7, while the random inertia weight varies between 0.5 and 1. w_3 is a linearly decreasing inertia weight, starting from 0.9 and decreasing to a minimum value of 0.4. Moreover, w_4 follows a nonlinear, time-decreasing strategy. w_5 uses values based on the global best fitness and the average local best fitness.

Table 1: Various inertia weight approaches

Inertia Weight	Reference
$w_1 = 0.7$	(Shi & Eberhart, 1998)
$w_2 = \frac{1 + rand()}{2}$	(Eberhart & Shi, 2001)
$w_3 = (w_{max} - w_{\min})\frac{(T_{max} - t)}{T_{max}} + w_{\min}$	(Arasomwan & Adewumi, 2013)
$w_4 = \left(\frac{2}{iter}\right)^{0.3}$	(Fan & Chiu, 2007)
$w_5 = 1.1 - \frac{FGbest}{(FPbest_i)_{average}}$	(Arumugam & Rao, 2008)

3. System description and PID optimization

3.1. Model

This part tunes the PID controller using an example of a DC motor system. The major objective is to efficiently manage the motor's speed. To develop a mathematical model, the mechanical stress is expressed as a constant torque (τ_L) and this system is considered to be linear. The speed of the DC motor is controlled by regulating the armature voltage $v_a(t)$. This produces an electromechanical force while armature current $i_a(t)$ adjusts proportionally to the rotational speed (Ayinla et al., 2024; Izci and Ekinci, 2023). To model the DC motor, the following differential expressions characterizing the motor's speed and torque dynamics are provided:

$$v_a(t) = i_a(t)R_a + L_a\frac{di(t)}{dt} + E_b \tag{3}$$

Under constant flux conditions, the motor's induced voltage E_b is linearly related to the angular velocity ω as illustrated below:

$$E_b = K_b \frac{d\theta(t)}{dt} = K_b \, \omega(t) \tag{4}$$

A total torque consists of the impact of the inertia and fractional torques which is given by

$$T_E - T_L = J \frac{d\omega(t)}{dt} + B \, \omega(t) = K_m i_a(t) \tag{5}$$

where R_a and L_a are the resistance and inductance of the DC motor respectively. E_b is the back electromotive force, K_b is the constant, θ is the angular velocity, ω is the motor shaft velocity, T_E, T_L are the electric and load torques respectively, J indicates the motor's moment of inertia. B and K_m are frictional and torque constants respectively. Applying Laplace transform to equations (1-3) (with zero initial conditions) which leads to

$$v(s) = (L_a s + R_a) i_a(s) + E_b(s) \tag{6}$$

$$E_b(s) = K_b \omega(s) \tag{7}$$

$$T_E(s) - T_L(s) = (Js + b)\omega(s) = K_m i_a(s) \tag{8}$$

Simplifying equations (4) and (6) results in

$$i_a(s) = \frac{v(s) - K_b \omega(s)}{L_a s + R_a} \tag{9}$$

$$\omega(s) = \frac{T_E(s) - T_L(s)}{Js + B} = \frac{K_m}{Js + B} i_a(s) \tag{10}$$

The DC motor’s transfer function can be expressed as follows:

$$G_p(s) = \frac{\omega(s)}{v(s)} = \frac{K_m}{(L_a s + R_a)(Js + B) + K_b K_m}, \; T_L(s) = 0 \tag{11}$$

Table 1 gives the parameter values of the DC motor, which is adopted from (Izci and Ekinci, 2023).

Table 2. Parameter vaules.

Symbol	Definition	Value
R_a	Armature resistance	0.4 Ω
L_a	Armature inductance	2.7 H
J	The moment of inertia	0.0004 kg m^2
B	The frictional constant	0.0022Nms/rad
K_m	Torque constant	0.015 N m/A
K_b	Back electromotive constant	0.05 Vs

3.2. PSO variant based PID controller design

The PID controllers maintain a desired setpoint of closed-loop systems. The PID controller has proportional (K_p), integral (K_i), and derivative (K_d) parameters (Karl & Tore, 1995). The transfer function of the PID controller is given as

$$C_{PID}(s) = K_p + K_i \frac{1}{s} + K_d s \tag{12}$$

The ITAE objective function is common in the litature (Ekinci, Hekimoğlu & Izci, 2021). The ITAE function is given as presented in Equation. (13). The settings are given in Table 2.

$$\text{ITAE} = \int_0^{tsim} t\,|e(t)|dt \tag{13}$$

The optimization process of PSO-based-PID controller gains was started by using the initialisation. This step involved combining the PSO algorithm with a MATLAB/Simulink model. For each candidate in the population, the PID gains were given as a vector, $K = (Kp, Ki, Kd)$ corresponding to each candidate in the neighbourhood. There were N randomly selected candidates in the population. A time-domain simulation of the DC motor speed control system with unity feedback and the suggested PID controller was performed for each choice. For every candidate, the ITAE values were computed. Since different candidates typically resulted in varying speed outputs and ITAE values, the N best solutions with the lowest ITAE values were selected for the next iteration and updated before returning to the PSO algorithm. This process was continued until the maximum number of iterations was reached. The candidate with the lowest ITAE value was recorded as the optimal PID controller, and Table 4 presents the obtained PID parameters for the controllers.

Table 3. Settings of the PSO variants algorithm for tuning controllers

Setting	Value
c_1, c_2	2
w_{Max}, w_{Min}	0.9, 0.4
Population size	10
Maximum iteration	20
Lower pound	[0.001 0.001 0.001]
Upper bound	[20 20 20]
Dimension	3
Simulation	1s

Table 4. Optimal PID settings found using the PSO variants algorithm

Controller	(Kp, Ki, Kd)
PIDw1	20.0000, 4.5991, 3.4689
PIDw2	20.0000, 4.6769, 3.4658
PIDw3	20.0000, 5.1601, 3.5204
PIDw4	20.0000, 5.3782, 3.5210
PIDw5	20.0000, 5.3441, 3.5349

4. Results and discussion

This section presents the optimised PID controller's simulation results. Convergence curves of the ITAE objective function using the PSO algorithm with different inertia weights is ilustrate in Figure 3.

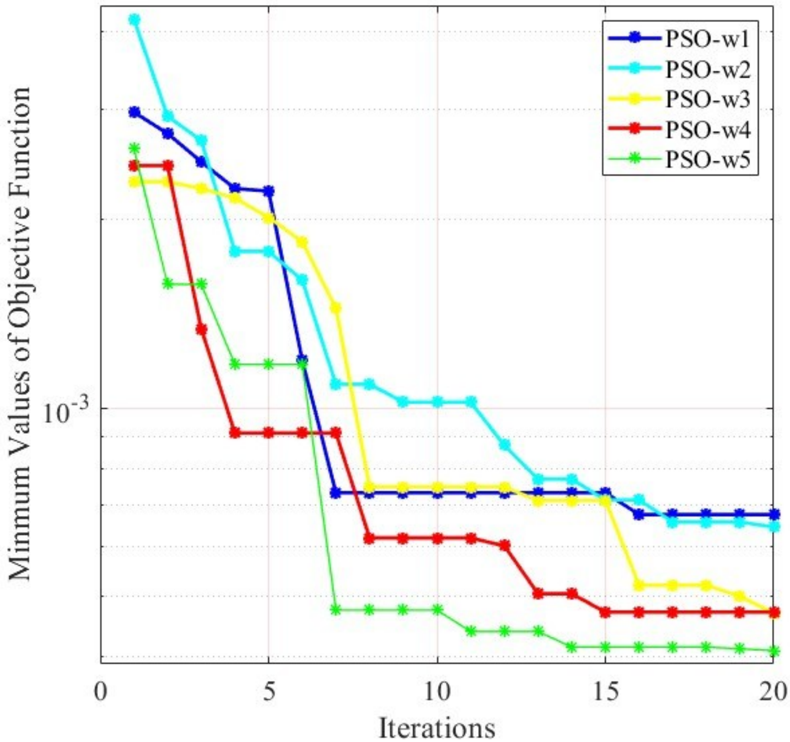

Figure 2. Convergence curves of the objective function using the PSO algorithm with different inertia weights

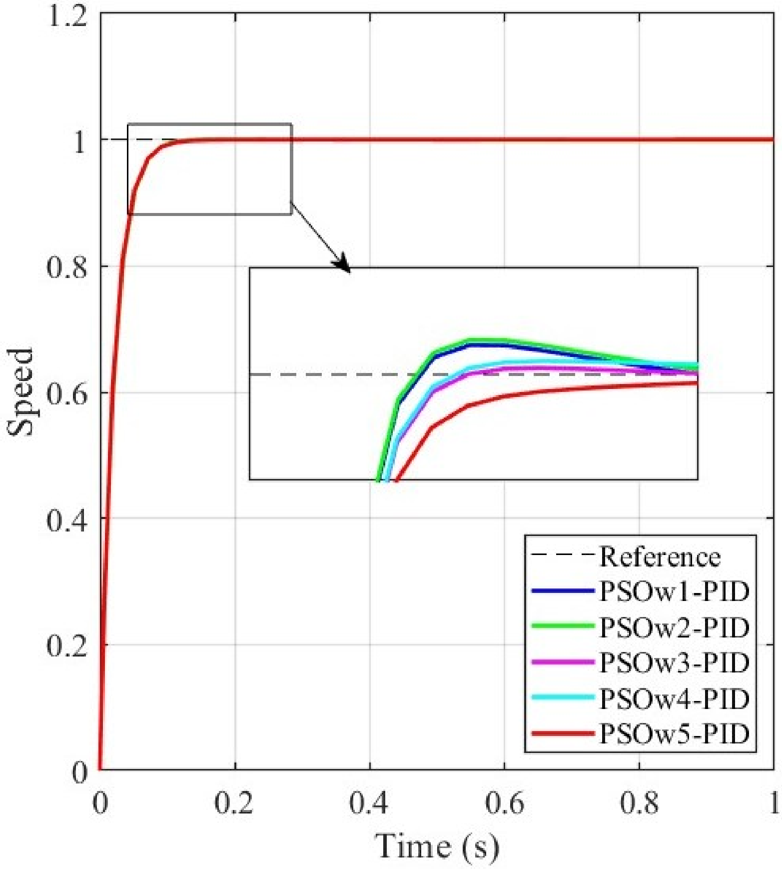

Figure 3. Responses of the PSO variants-based PID-controlled system.

The closed-loop responses in terms of time and frequency are shown in Figures 3 and 4 respectively. The corresponding results are reported in Tables 5 and 6. Rise time is the time it takes for the system's output to rise from 10% to 90% of its final value. A rise time of 0.045998 seconds was achieved by the PSOw5 algorithm, enabling the system to reach its final value the fastest. This indicates that the system performs well in terms of speed. Settling time refers to the time when the output remains within a certain percentage (2%) of its final value. The PSOw1 algorithm achieved the lowest settling time, with a value of 0.081339 seconds, allowing the system to reach a steady state quickly without oscillating around the final value. The lowest overshoot (0.0058681%) and steady-state error (6.3138e-05) were obtained by the PSOw5 algorithm. Overall, the PSOw5-based PID controller demonstrates excellent time-domain performance.

Table 5. Time-domain performance analysis.

	tr	ts	OS (%)	Ess (%)
PSOw1-PID	0.046534	**0.081339**	0.11907	0.064333
PSOw2-PID	0.046573	0.081387	0.12144	0.057354
PSOw3-PID	0.046114	0.081824	0.027973	0.015591
PSOw4-PID	0.046132	0.08197	0.022091	0.003133
PSOw5-PID	**0.045998**	0.081975	**0.0058681**	**6.3138e-05**

Table 6. Frequency-domain performance analysis

	Gain margin(dB)	Phase margin(deg)	Bandwidth (Hz)
PSOw1-PID	Inf	-180	48.1982
PSOw2-PID	Inf	-180	48.1601
PSOw3-PID	Inf	-180	48.8157
PSOw4-PID	Inf	-180	48.8215
PSOw5-PID	Inf	-180	**48.9906**

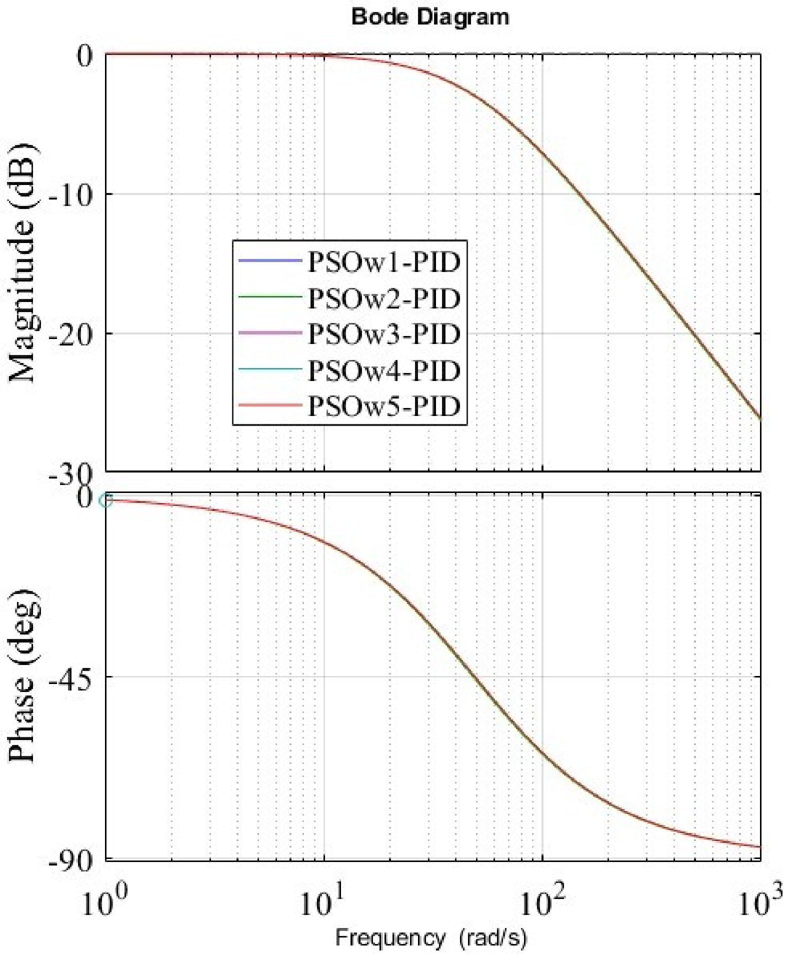

Figure 4. Bode plots of the PSO-based PID-controlled DC motor.

Frequency domain analysis was conducted as follows. The gain margin indicates how much the system's gain can be increased before it becomes unstable. An infinite gain margin (∞ dB) suggests that the system is highly stable and can tolerate a significant increase in gain without becoming unstable. The phase margin indicates the stability of the system by showing how much phase lag it can tolerate before reaching instability. A phase margin of 180° means that the system is extremely stable. According to Table 6, all controllers achieve infinite gain margin and a -180° phase margin. The PSOw5-based controller provides the highest bandwidth among the algorithms.

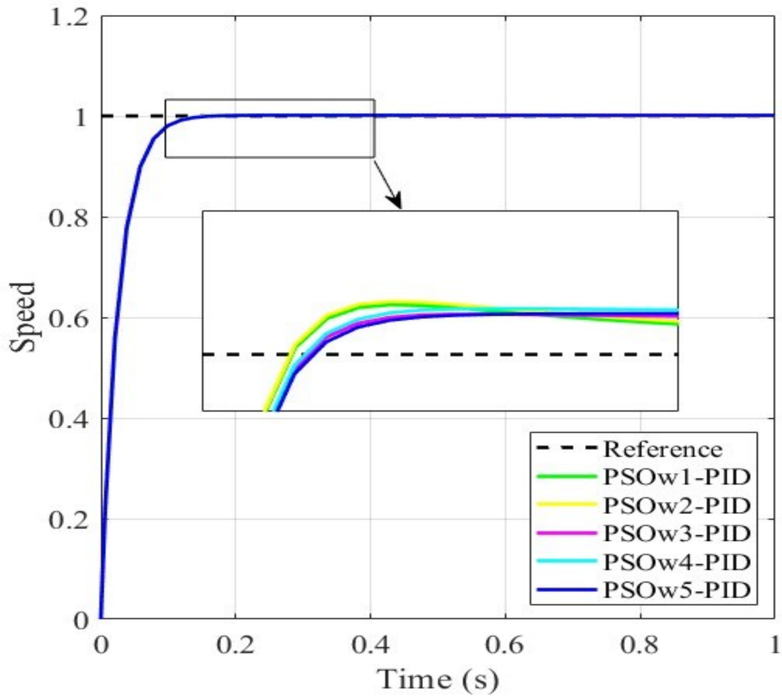

Figure 5. Analysis of *closed-loop responses with parameters,* $R_a = 0.30$ *and* $K_m = 0.012$

Table 7. Performance evaluation with parameters, $R_a = 0.30$ *and* $K_m = 0.012$

	tr	ts	OS (%)	Ess (%)
PSOw1-PID	0.056645	**0.0987**	0.12408	**0.049567**
PSOw2-PID	0.056702	0.098743	0.12713	0.057943
PSOw3-PID	0.056251	0.09995	0.03306	0.10811
PSOw4-PID	0.056308	0.10022	0.029513	0.13059
PSOw5-PID	**0.056147**	0.10034	**0.016301**	0.12691

The DC motor's electrical resistance (R_a) and torque constant (K_m) were varied by ±25% and ±20%, respectively, to perform the robustness analysis. This leads to four different types of parametric uncertainties. Figures 5, 6, 7 and 8 show the closed-loop step responses for all conditions. Tables 7, 8, 9 and 10 present the simulation findings for the time-domain performance assessment. The best values attained in the table are highlighted in bold. It is evident from the table that the PSOw1 and PSOw5-based PID controllers make the system robust. Despite varying parameters in the DC motor system, the proposed PSOw5-PID controller provides the lowest rise and overshoot for all testing conditions. For $R_a = 0.30$ *and* $K_m = 0.012$, the PSOw1-PID controller exhibits a settling time of 0.0987 seconds and a steady-state error of 0.049567%, respectively.

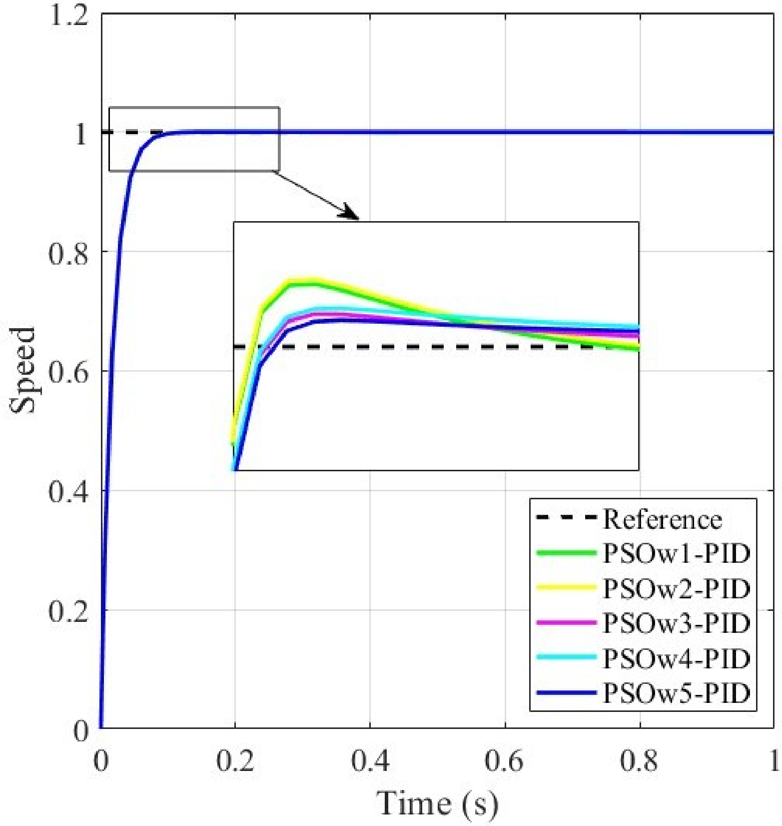

Figure 6. Analysis of *closed-loop responses with* $R_a = 0.30$ *and* $K_m = 0.018$.

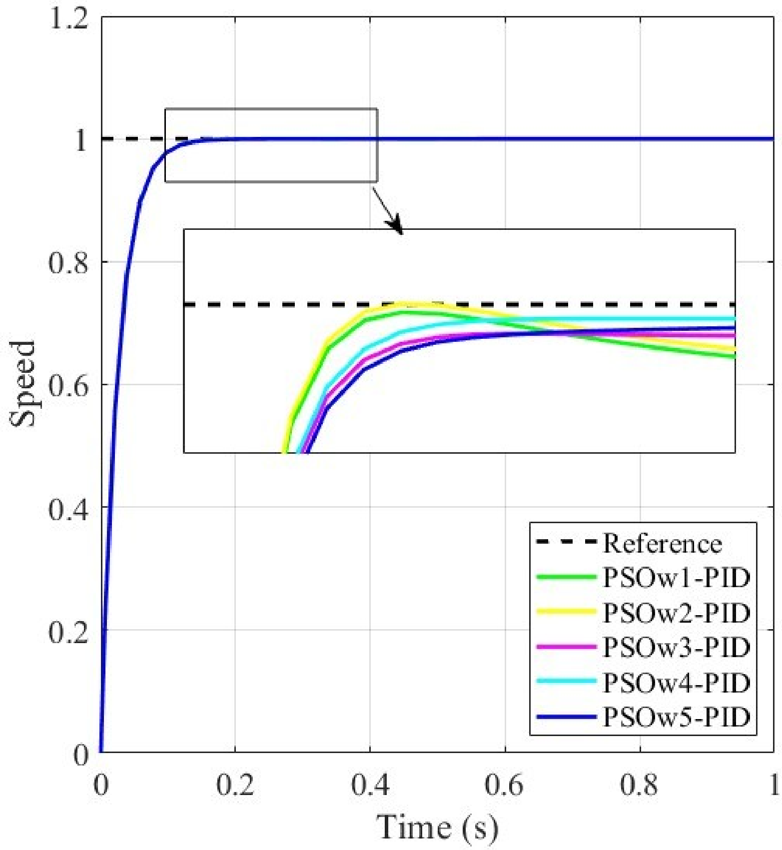

Figure 7. Analysis of *closed-loop responses with* $R_a = 0.50$ *and* $K_m = 0.012$

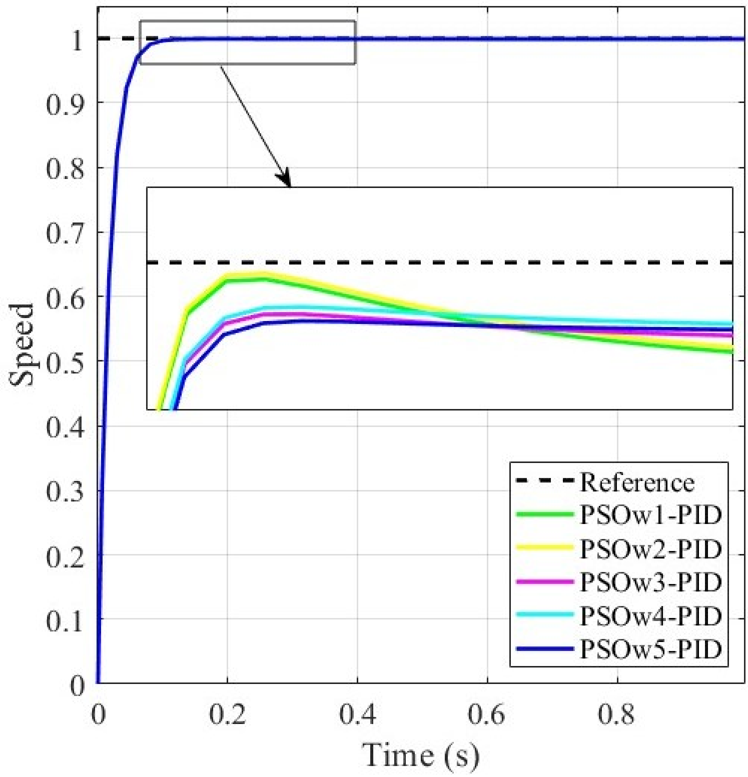

Figure 8. Analysis of *closed-loop responses with* $R_a = 0.50$ *and* $K_m = 0.018$

Table 8. Performance evaluation of condition II: $R_a = 0.30$ *and* $K_m = 0.018$

	tr	ts	OS (%)	Ess (%)
PSOw1-PID	0.038898	**0.06807**	0.13971	0.038862
PSOw2-PID	0.03893	0.068113	0.14186	0.033129
PSOw3-PID	0.03853	0.068394	0.051471	**0.0012387**
PSOw4-PID	0.038543	0.068511	0.045389	0.016615
PSOw5-PID	**0.038429**	0.068493	**0.028822**	0.014111

Table 9. Performance evaluation of condition III: $R_a = 0.50$ *and* $K_m = 0.012$

	tr	ts	OS (%)	Ess (%)
PSOw1-PID	0.056642	**0.099051**	0.092271	0.10266
PSOw2-PID	0.056701	0.099122	0.094798	0.093808
PSOw3-PID	0.056254	0.10037	0.0018215	0.040969
PSOw4-PID	0.056314	0.10066	**0**	**0.017213**
PSOw5-PID	**0.056151**	0.10077	**0**	0.021142

Table 10. Performance evaluation of condition IV: $R_a = 0.50$ *and* $K_m = 0.018$

	tr	ts	OS (%)	Ess (%)
PSOw1-PID	0.038881	**0.068238**	0.11675	0.1398
PSOw2-PID	0.038913	0.068285	0.11853	0.13374
PSOw3-PID	0.038515	0.068568	0.027564	0.097524
PSOw4-PID	0.038529	0.068693	0.020934	**0.081268**
PSOw5-PID	**0.038415**	0.068668	**0.0047536**	0.083944

5. Conclusions

This study investigates efficiency of the particle swarm optimization (PSO) with different inertia weights. Inertia weight determines the convergence success rate in the PSO algorithm. We have employed five inertia weights including constant random linearly decreasing, nonlinearly decreasing local global best fitness values basis. We use PSO variants to estimate the parameters of the PID controller to regulate DC motor speed. The PSO with global-average, local fitness-based inertia weight method (PSOw5) outperformed various time-domain performance criteria and delivered improved objective function values, demonstrating its effectiveness in controlling DC motor speed. Additionally, the closed-loop step response of the PSO with global-average, local fitness-based inertia weight controller demostrated its capability to regulate motor speed under different parametric conditions. When compared to other inertia weight approaches, the PSOw5-based PID approach achieved the best transient response specifications, such as speed rise time and overshoot. This study evaluates the potential of different inertia weight approaches in PSO algorithms for enhancing controller performance in controlling DC motor speed. By using this recent metaheuristic algorithm, the speed control of DC motors can be made more accurate and efficient.

Acknowledgement

This study was supported by Artvin Çoruh University Scientific Research Unit (BAP, Turkey) Project No: 2024.F14.02.01.

References

Arasomwan, M. A., & Adewumi, A. O. (2013). On the performance of linear decreasing inertia weight particle swarm optimization for global optimization. *The Scientific World Journal*, *2013*(1), 860289.

Arumugam, M. S., & Rao, M. V. C. (2008). On the improved performances of the particle swarm optimization algorithms with adaptive parameters, cross-over operators and root mean square (RMS) variants for computing optimal control of a class of hybrid systems. Applied Soft Computing, 8(1), 324-336.

Aydilek, İ. B., Nacar, M. A., GümüŞÇü, A., & Salur, M. U. (2017, September). Comparing inertia weights of particle swarm optimization in multimodal functions. In *2017 International Artificial Intelligence and Data Processing Symposium (IDAP)* (pp. 1-5). IEEE.

Ayinla, S. L., Amosa, T. I., Ibrahim, O., Rahman, M. S., Bahashwan, A. A., Mostafa, M. G., & Yusuf, A. O. (2024). Optimal control of DC motor using leader-based Harris Hawks optimization algorithm. Franklin Open, 6(100058), 100058.

Eberhart, R. C., & Shi, Y. (2001, May). Tracking and optimizing dynamic systems with particle swarms. In *Proceedings of the 2001 congress on evolutionary computation (IEEE Cat. No. 01TH8546)* (Vol. 1, pp. 94-100). IEEE.

Ekinci, S., Hekimoğlu, B., & Izci, D. (2021). Opposition based Henry gas solubility optimization as a novel algorithm for PID control of DC motor. *Engineering Science and Technology an International Journal*, *24*(2), 331–342.

Fan, S. K. S., & Chiu, Y. Y. (2007). A decreasing inertia weight particle swarm optimizer. Engineering Optimization, 39(2), 203-228.

Karl, J. A., & Tore, H. (1995). PID controllers: theory, design, and tuning. *Publisher: ISA*.

Kennedy, J., & Eberhart, R. (1995, November). Particle swarm optimization. In *Proceedings of ICNN'95-international conference on neural networks* (Vol. 4, pp. 1942-1948). IEEE.

Nickabadi, A., Ebadzadeh, M. M., & Safabakhsh, R. (2011). A novel particle swarm optimization algorithm with adaptive inertia weight. Applied soft computing, 11(4), 3658-3670.

Shi, Y., & Eberhart, R. (1998, May). A modified particle swarm optimizer. In 1998 IEEE international conference on evolutionary computation proceedings. IEEE world congress on computational intelligence (Cat. No. 98TH8360) (pp. 69-73). IEEE.

Taherkhani, M., & Safabakhsh, R. (2016). A novel stability-based adaptive inertia weight for particle swarm optimization. *Applied Soft Computing*, *38*, 281-295.

Van Den Bergh, F. (2001). An analysis of particle swarm optimizers, Ph.D. thesis. Department of Computer Science, University of Pretoria (South Africa).

CHAPTER III

Hardware Trojan Attack In The Automotive

Cumhur MELCİK[1]

Introduction

The automotive industry is undergoing a major transformation with the development of Electronics, electric vehicles, autonomous vehicles, hybrid vehicles are finding more and more space on the roads, the percentage of people preferring these vehicles is increasing day by day. Cars are rapidly becoming smart vehicles, like phones and televisions, and in the near future, cars will be fully connected to the internet and it will be possible to do many of the things we do on our phones, such as making phone calls, accessing news, online shopping, etc.(Wiener 2018) Many vehicles allow us to make phone calls today, and this development in the automotive sector is accelerating with the development of electronic

[1] Department of R&D, Koluman Otomotiv Endüstri A.Ş cumhur.melcik@koluman.com, ORCID ID: https://orcid.org/0009-0002-6108-4917

devices day by day. (Kent 2024)) We expect the development of electronic devices to take up a lot of space in the vehicle, but this is not the case, with the development of chip technology, the size of electronic devices is decreasing according to the work they do, every two years the electronic processor produced is twice as powerful as the previous processor, this is based on Moore's law(BOSCH, & Powers, C. (1991).). The electronic chips are located in the ECUs that electronically provide in-vehicle communication and vehicle control. There are billions of transistors and logic lines inside the chips, although the area on the chip is getting shorter, the logic lines are increasing, this increase makes it impossible to find or observe the logic lines that are changed or added to the chip. As chip technology continues to evolve, vulnerabilities are emerging, the most important and dangerous of these vulnerabilities is the so-called hardware Trojan attack, with this attack, logic gates added to the chip or on the PCB can create unwanted situations. The hardware Trojan , which is not added during the procurement process or production phase, or during the design phase, but added by malicious people, is triggered in unexpected situations, this triggering is used to crash the system or to age electronic components in a timely manner. As stated in this (Rouf 2010) article, it will be easier to intervene and collect data from outside in protocols that communicate with frequency in the vehicle, the trigger to be placed in the chip or system can trigger the system and make the system unusable. The most sensitive point in the vehicle is the CAN bus line because with this line, vehicle ECUs communicate with each other and transmit critical information.(Elkhail 2021)(Bozdal 2018)

ABAOUT CAN BUS

CAN (Controller Area Network) bus is a network that provides communication between in-vehicle sensors and ECUs. A modern vehicle can have more than 70 ECUs. ECUs provide control of critical parts in the vehicle such as engine, steering, brakes, etc. Not all in-vehicle communication works with CAN protocol, there are other communication protocols such as LIN, MOST, etc.(Payne 2019)

The devices on the CAN bus are called nodes. Figure(1) shows in-vehicle communication, each node consists of a CPU, a CAN controller and a transceiver that adapts the signal levels of the data sent and received by the node. All nodes can send and receive data, but not simultaneously. The system works asynchronously, meaning that a system does not have a clock signal. Each system has an ID, which determines which part of the system has priority. Priority systems have priority within the line, for example the Brake signal has priority over the Air Conditioner signal.(BOSCH, & Powers, C. (1991).)

The CAN Line has two 120 ohm resistors at both ends. The CANH wire has 3.5V CANL wire has 1.5V, the information sent in the system is sent as 1 and 0, 0 is the dominant signal in the system.

There is an OBD point in the vehicle where we can read the CAN line for vehicle diagnostics. By connecting from this point, we can find the vehicle fault and access the CAN information flowing in the vehicle. This connection point is available in all cars manufactured since 1989. OBD point is one of the most vulnerable places on the vehicle, OBD point is used to hack the vehicle.

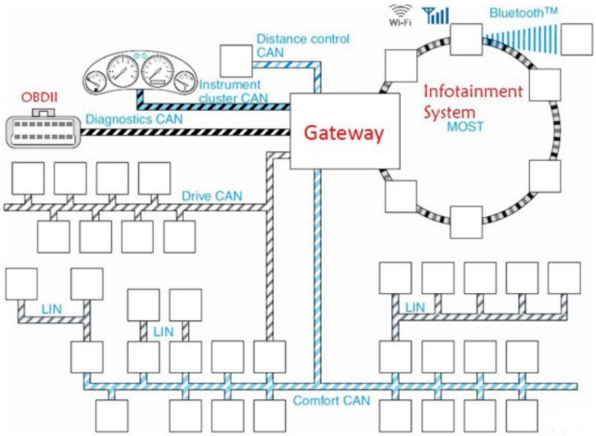

Figüre(1)(J. li 2016)

WHAT IS OBD.

OBD is used to detect and communicate electronic components on the vehicle. OBD appearance and pin arrangement are as in Figure (2). By connecting to the vehicle via the OBD system, it is possible to detect electronic communication errors of the vehicle, vehicles can be intervened on the same line, software can be installed on the vehicle, LOG records on the vehicle are received and CAN messages returning in the vehicle are read.

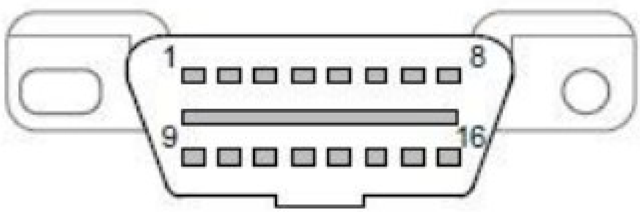

Figure(2)(Malekian 2016)

HARDWARE TROJAN.

Hardware Trojans are logic gates that are not part of the system or chip design process but are added later for malicious activities. Logic gates added from outside and afterwards to the logic lines indicated in red in the logic gate in Figure (3) can trigger and affect the operation of the system.(Besser 2002))(Jain 2021)(Xiao 2016) It can even happen by connecting to the system remotely.(Subramani 2017)

With this system, which can be found in electronic devices, information, documents are used to transfer information to people who want to interfere with the system from outside. A hardware Trojan can remain passive during normal operation, but can become active in certain situations or in unlikely situations. This makes hardware Trojans difficult to detect. As chip technology advances, Trojan horses continue to become more difficult to detect and detect.

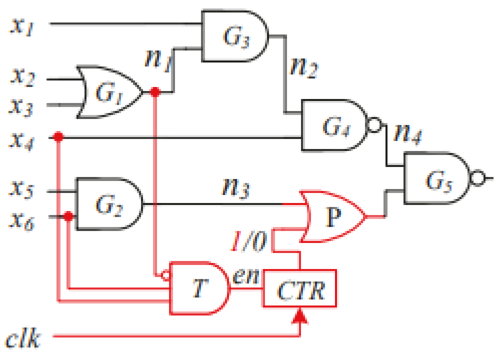

Figüre(3)(Jain 2021)

WHAT IS A CHIP.

Chips are the most important part of electronic development and the technologies that make our lives easier. Almost all of today's electronic devices use chips, cell phones, computers, tablets and automobiles are just a few examples. There are many types of chips; processor chips, graphics chips, memory chips, network chips, sensor chips, microcontroller chips and so on, which means that chips are found in every field of electronics.

Chips are made up of billions of transistors, according to Moore's law, every two years the number of transistors in a chip doubles while the cost of the chip remains the same.(Hemani 2000) This increase has made it almost impossible to control the transistors in the chip.

Method

Impact On The Automotive System.

Electronic components in the automotive system are potential infiltration points for a Hardware Trojan , the collapse of the electronic system can cause accidents with loss of life, and research at the University of California has shown that they can cause the vehicle's brakes to lock up while driving (Payne 2019).These situations cause civilian vehicles and vehicles produced for the defense industry to become unusable or planned obsolescence. Extra logic gates that can be added to the chips inside the vehicle ECUs or on the PCB can be triggered in unwanted situations and cause vehicles to crash, the same system can leak the information inside the vehicle.(Xiao 2016) Especially the wireless connection of new vehicles to the internet is a major threat to vehicle security and privacy, In-car camera or exterior cameras can leak images outside the vehicle with Hardware Trojan . For this, it would be better to use communication systems that will not interfere with the vehicle from outside, especially in military vehicles. For this, it would be correct to prefer wired communication protocols such as Can Bus, which is used in most vehicles.

Trojan horse attacks will be a greater danger especially for vehicles connected to the internet, and it is quite possible that the vehicles will become unusable with the software updates that the vehicles receive remotely. The news that the Tesla brand vehicle became unusable with the update it received(Kent 2024) supports this situation.

If we give a simple example, the smd receiver circuit added to the chip or pcb in the in-vehicle ECU can be designed to be triggered from the outside, this design becomes a circuit triggered by certain frequencies. With the frequency sent to this circuit from outside, in-vehicle communication may collapse, or with the trigger added to the chip, the ECU may become unusable or leak signals to the outside.

THINGS TO WATCH OUT FOR.

SUPPLY CHAIN

Hardware Trojans are hidden in the chip, the hidden logic lines are usually activated in rare circumstances and it may not be possible to detect the Trojan inserted in the chip. This is why the supply chain is important.

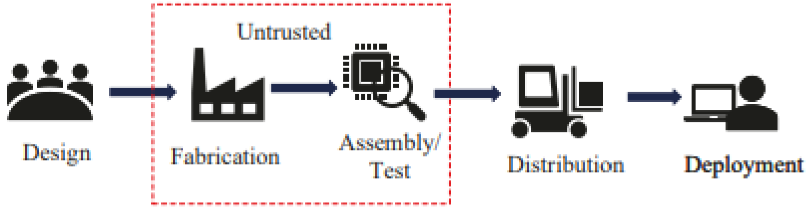

Figure 4(Jain 2021)

Hardware Trojans can be added during design or due to weaknesses in the transfer process (Shield 2015), Suppliers should be reliable suppliers, products purchased for cost reduction may have irreversible consequences later. A trusted supplier must also have trusted sub-suppliers.

TANSFER PROCESS OF THE PRODUCTS MUST BE RELIABLE

Recently most of the products arrive by sea, this increases the time in the product transfer, as the time increases, the risks for the product can increase, the product can be intercepted in the transfer process and the chips inside the products can be removed and chips with Hardware Trojan Horse added can be added.

DOUBLE PROTECTION IN CRITICAL

Brains that control important components such as Engine, Transmission, Brake, Gas can be double protected. With this protection, two brains supplied from different suppliers can be used and the other brain can control the system when the other brain fails or is deactivated, in case of an attack in this way, the system survives the possible attack without damage due to the fact that there are two different suppliers and two different brains.

CHIP PRODUCTION.

It would be the easiest way for companies and countries to produce their own chips, so that the hardware Trojan cannot be put into the chip production without being in the design, it should not be forgotten that the control of the system depends on the chips.

Results and Discussion

Rapid electronic developments in the automotive sector create risks such as hardware Trojan horses and software Trojan horses that threaten vehicle safety. Competition in the automotive sector, the development of electronic products and the competition due to the inadequacy of the market to access these products lead companies to different companies, malicious people who intervene in this process can place trigger mechanisms in the chip. These trigger mechanisms remain dormant for a long time without being noticed, triggering the system in difficult situations, damaging the ECUs of vehicles or causing electronic devices to fail earlier with long planned obsolescence. For this reason, chip production stages should be well monitored and the security of subcontractors should be well ensured. In future studies, two different brains from two different suppliers can control each other in critical brains.

References

Elkhail, A. A., Refat, R. U. D., Habre, R., Hafeez, A., Bacha, A., & Malik, H. (2021). Vehicle Security: A survey of security issues and vulnerabilities, malware attacks and defenses. IEEE Access, 9, 162401–162437. https://doi.org/10.1109/access.2021.3130495

Bozdal, M., Randa, M., Samie, M., & Jennions, I. (2018). Hardware Trojan enabled denial of service attack on CAN bus. Procedia Manufacturing, 16, 47–52. https://doi.org/10.1016/j.promfg.2018.10.158

Rouf, I., Miller, R., Mustafa, H., Taylor, T., Oh, S., Xu, W., Gruteser, M., Trappe, W., & Seskar, I. (2010). Security and privacy vulnerabilities of in-car wireless networks: a tire pressure monitoring system case study. USENIX Security Symposium, 21. http://cse.sc.edu/~wyxu/papers/TPMS2010.pdf

Wiener, G. (2018b). Cyberterrorism and ransomware attacks. Greenhaven Publishing LLC.

Besser, L., & Gilmore, R. (2002). Practical RF circuit design for modern wireless systems: Passive Circuits and Systems Passive Circuits and Systems, Volume 1. Artech House.

Kent, Lauren. "Chechen Warlord Accuses Elon Musk of "Remotely Disabling" His Cybertruck." CNN, CNN, 20 Sept. 2024, edition.cnn.com/2024/09/20/business/chechnya-kadyrov-musk-tesla-cybertruck-disabled/index.html. Accessed 23 Sept. 2024.

Jain, Ayush, et al. "Survey of Recent Developments for Hardware Trojan Detection." IEEE Xplore, 1 May 2021, ieeexplore.ieee.org/document/9401143.

Subramani, K. S., Antonopoulos, A., Abotabl, A. A., Nosratinia, A., & Makris, Y. (2017). ACE: Adaptive channel estimation for detecting analog/RF trojans in WLAN transceivers. 2017 IEEE/ACM International Conference on Computer-Aided Design (ICCAD). https://doi.org/10.1109/iccad.2017.8203848

Hemani, A., Jantsch, A., Kumar, S., Postula, A., ESDlab, Dept. of Electronics, Royal Institute of Technology, KTH, Electrum, 164 40 Kista, Sweden, School of Engineering, Jönköping, Sweden, University of Queensland, Brisbane, Australia, Öberg, J., Millberg, M., & Lindqvist, D. (2000). Network on a Chip: An architecture for billion transistor era [Journal-article]. https://d1wqtxts1xzle7.cloudfront.net/32403620/noc_billion-libre.pdf?1391560486=&response-content-disposition=inline%3B+filename%3DNetwork_on_a_Chip_An_architecture_for_bi.pdf&Expires=1727162481&Signature=HvBmnmoDFzG67RmSAPC4vJB-8ZqmNJNt9z57Oc8kXCXUme7UyLrQGOX~3qlA1eqMEkfkxPjDdSLobsfDyk-9SFk23h49FHTXbXTTF42o5n3w8YIML8uAH6fVezD~04bmKAUSXncGWmxUI6GXBG1OHbcvsIi3P0Bdhc81AHTqJCgPTYQsvtPmXoRuipiVlv0-nnH8x63w5BuA10I875HQKRBKxd6zPsFbZYvgG~W7eiKHErQCwNGZ-V0uycfMdDZf-0JfLNvoddsw15Kxe6hlam3K9Zx87gwg2pmqqq3MAvdx8kK6gKwBOyNzunWEotHXYWGvdFMl6R2ghf6EY9wK4w__&Key-Pair-Id=APKAJLOHF5GGSLRBV4ZA

Xiao, K., Forte, D., Jin, Y., Karri, R., Bhunia, S., & Tehranipoor, M. (2016). Hardware trojans. ACM Transactions on Design Automation of Electronic Systems, 22(1), 1–23. https://doi.org/10.1145/2906147

Shield, J., Hopkins, B. D., Beaumont, M. R., & North, C. J. (2015). Hardware Trojans - A systemic threat. Artificial Intelligence and Symbolic Computation, 45–51. https://crpit.scem.westernsydney.edu.au/confpapers/CRPITV161Shield.pdf

Xiao, K., Forte, D., Jin, Y., Karri, R., Bhunia, S., & Tehranipoor, M. (2016b). Hardware trojans. ACM Transactions on Design Automation of Electronic Systems, 22(1), 1–23. https://doi.org/10.1145/2906147

IEEE Xplore Full-Text PDF: (n.d.). https://ieeexplore.ieee.org/stamp/stamp.jsp?arnumber=8993719

(N.d.). Psu.edu. Retrieved October 7, 2024, from https://citeseerx.ist.psu.edu/document?repid=rep1&type=pdf&doi=54d1273ed7830c01d74025b75da6f44988058a40

BOSCH, & Powers, C. (1991). CAN Specification. Robert Bosch GmbH. http://esd.cs.ucr.edu/webres/can20.pdf

Payne, B. R. (2019). Car hacking: Accessing and exploiting the CAN bus protocol. Journal of Cybersecurity Education, Research and Practice, 2019(1). https://doi.org/10.62915/2472-2707.1045

J. Li, in Presentation slides on Hack In The Box Security Conference (HITBSecConf). CANsee-An Automobile Intrusion Detection System (2016) [Online] http://conference.hitb.org/hitbsecconf2016ams/materials/D2T1%20-%20Jun%20Li%20-%20CANSsee%20-%20An%20Automobile%20Intrusion%20Detection%20System.pdf

Malekian, R., Moloisane, N. R., Nair, L., Maharaj, B. T., & Chude-Okonkwo, U. a. K. (2016). Design and implementation of a wireless OBD II fleet management system. IEEE Sensors Journal, 17(4), 1154–1164. https://doi.org/10.1109/jsen.2016.2631542

Jain, A., Zhou, Z., & Guin, U. (2021, May 1). Survey of Recent Developments for Hardware Trojan Detection. IEEE Xplore. https://doi.org/10.1109/ISCAS51556.2021.9401143

CHAPTER IV

UWB Antenna Design Based on Jean Material for Wireless Body Area Network

Eray Mert TEKİN [1]
Ali AKDAĞLI [2]
Hakan İŞIKER [3]
İbrahim ÇELİK [4]

INTRODUCTİON

Wireless communication systems are a cornerstone of modern communication technologies. These systems enable data transmission through electromagnetic waves, allowing devices to communicate without physical connections. Today, various wireless

[1] Lect,, Mersin University, Vocational School of Technical Sciences, Department of Electricity and Energy , Orcid: 0000-0001-6578-1061
[2] Prof. Dr., Mersin University, Faculty of Engineering, Department of Electrical and Electronics, Orcid: 0000-0003-3312-992
[3] Asst. Prof., Mersin University, Faculty of Engineering, Department of Electrical and Electronics, Orcid: 000-0002-6465-8480
[4] Lect., Mersin University, Vocational School of Technical Sciences, Department of Electronics and Automation, Orcid: 0000-0002-0403-7316

communication protocols such as Wi-Fi, Bluetooth, and Zigbee are utilized in a wide range of applications, from smart home systems to industrial automation. With the miniaturization of mobile devices, microstrip patch antennas (MPAs), which can be easily integrated into these devices and are cost-effective, have become widely preferred. The majority of MPAs in the literature focus on regular geometries (Balanis, 2013:813). These geometries are presented in Figure 1.

(a) (b) (c) (d)

Figure 1. *MPA Geometries (a) Triangle (b) Circle (c) Square (d) Rectangle*

Wireless Body Area Networks (WBAN) are networks that enable wireless communication between sensors placed on or within the human body. These networks play a critical role in health monitoring, biomedical applications, and personal health devices (Pellegrini et al., 2013). Antennas used in WBANs must be compatible with the human body, flexible, and wearable, which is crucial for both system performance and user comfort. In wearable technologies, textile-based materials stand out as a preferred solution for antenna design (Mutlu and Kurnaz, 2020). The need for high-speed and reliable data transmission in WBAN systems has brought Ultra-Wideband (UWB) technology to the forefront in this field. The Federal Communications Commission (FCC) has designated the 3.1-10.6 GHz frequency range for UWB systems. However, this UWB frequency range overlaps with several narrowband communication systems, such as WLAN (5.15-5.85 GHz), WiMAX (3.3-3.7 GHz), X-band (7.25-7.75 / 7.9-8.4 GHz), and C-band (3.8-4.2 GHz). Numerous UWB Microstrip Patch Antenna (MPA) designs for WBAN applications are available in the literature. For example, Joshi et al. proposed a UWB MPA with a hexagonal patch. The antenna, measuring $46 \times 46 \times 1.5$ mm^3, uses FR4 as the substrate and operates within the 2.3-10.6 GHz range. Its ground plane features a semi-elliptical shape with a rectangular slot (Joshi, 2020). Similarly, Rahmatian et al. proposed a wearable UWB antenna with a frequency range of 3.9-10.75 GHz and dimensions of $61 \times 74 \times 3.5$ mm^3. The substrate material used is polydimethylsiloxane, a flexible material suitable for wearable applications (Rahmatian, 2019). In another study, Yang et al. designed a low-profile UWB antenna for WBAN applications. This antenna, with FR4 as the substrate, operates within the 2.5-24 GHz frequency range and has dimensions of $80 \times 80 \times 1$ mm^3 (Yang et al., 2018). Mahmood et al. developed a textile-based wearable UWB antenna for WBAN and breast cancer detection. The antenna operates within the 7–28 GHz bandwidth, with dimensions of $60 \times 50 \times 0.7$ mm^3. It is designed on denim fabric with a dielectric constant of 1.4 and a thickness of 0.7 mm. Shieldit textile material is used as the conductor (Mahmood, 2021). Singh et al. proposed a dual-band MPA designed on denim fabric. The experimentally measured MPA operates within the 3.01-5.30 GHz and 8.12-12.35 GHz frequency ranges, making it suitable for WiMAX (3.25-3.85 GHz), WLAN (5.15-5.35 GHz), and X-band (8-12 GHz) applications (Singh et al., 2017). UWB antennas, with their ability to operate over a wide frequency spectrum, provide high data rates with low power consumption. These features make UWB antennas an effective solution for WBAN applications, particularly for short-range wireless communication needs (Gürsoy and Bayer, 2020).

MATERYAL VE METOD

Microstrip Patch Antenna Design

The UWB MMPA design for WBAN consists of three main layers. The top and bottom layers are flexible FR4 material with a thickness of 0.2 mm. A circular patch model was preferred in the design as a radiating mobile. The patch and ground were corrected, and a copper conductor with a thickness of 35 µm was selected. Jean material was preferred in the middle layer due to its low cost, easy access and flexible structure. Jean is 0.8 mm. The design stages of UWB MMPA are shown in Figure 2. The design was carried out with CST Studio Suite, a full-wave solver based on finite integration technology (Access: 01.12.2024). The microstrip feeding method connected with a 50 ohm SMA component was preferred. The design stages are given in Figure 2. In the first stage, the radiating element consists of a 10 mm shaped patch and the back surface is completely copper-coated. The radius of the circular light element before its configuration was calculated using the expressions given below (Balanis, 2013).

$$f_r = \frac{f_1 + f_2}{2} \tag{1}$$

$$F = \frac{8{,}791\text{x}10^9}{f_r\sqrt{\varepsilon_r}} \tag{2}$$

$$\alpha = \frac{F}{\left\{1 + \frac{2h}{\pi\varepsilon_r F}\left[\ln\left(\frac{\pi F}{2h}\right) + 1{,}7726\right]\right\}^{1/2}} \tag{3}$$

Here f_1 is the first frequency, f_2 is the last frequency, a is the radius of the circular radiation element. f_r is in Hz, h is in cm. In the proposed study, a circle with a radius of approximately 1 cm was determined by selecting f_1 = 2 GHz and f_2 = 12 GHz. By making modifications on this circular radiation element, the best radiation was obtained with a radius of 8.2 mm. In the second stage, a slot with a radius of 2 mm was opened at the exact center of the patch. 4 slots with a radius of 1 mm were opened at 90-degree angles around this lobe. In the next stage, modifications were made on the ground plane to increase the performance. First, the length of the ground plane was reduced to 10 mm and a symmetrical slot with dimensions of 3.5 x 6 mm was opened from the center point. A circular lobe with a radius of 0.5 mm was added to the upper corner of the opened slot. The distance between the centers of these lobes is 1.5 mm. The lobes are added symmetrically with respect to the y-plane. At the end of the configuration of the ground plane, 8 lobes are added.

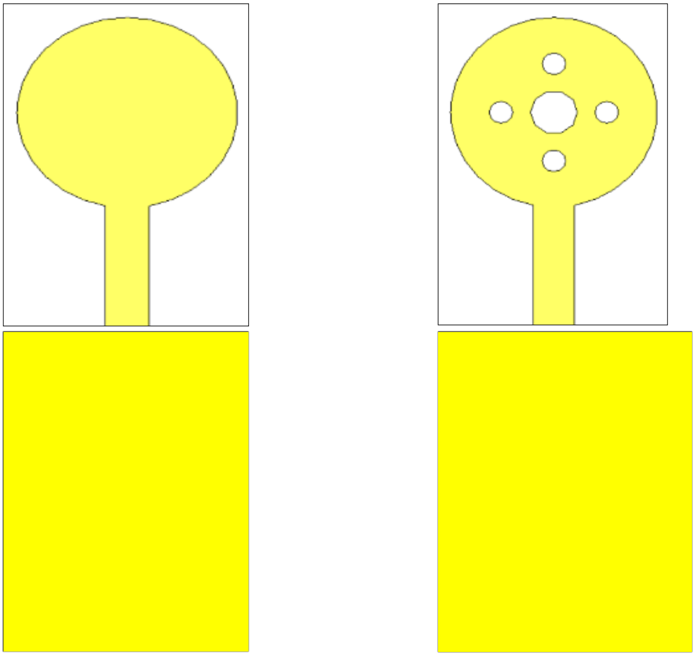

(a) (b)

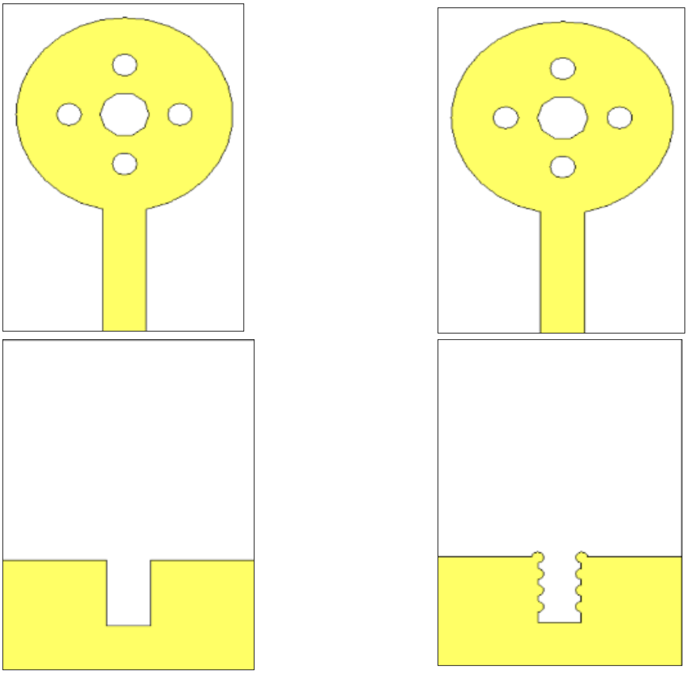

(c) (d)

Figure 2. *Proposed Jean-Based UWB MMPA Design Steps, (a) #1 Antenna, (b) #2 Antenna, (c) #3 Antenna, (d) #4 Antenna*

The completed Jean-Based UWB MMPA design given in Figure 3 has the dimensions of 30 x 20 x 1.4 mm^3. The Jean-based UWB MMPA design parameters are given in Table 1.

Table 1. *Jean Based UWB MMPA Design Parameters (mm)*

Ws=20	*Wf*=3.5	*L1*=1.5	*Ls*=30	*Lf*=11.3	*Lg*=10	*R1*=8.8	*hs*=0.2
Wg=20	*W1*=3.5	*L2*=0.5	*Lg*=10	*R2*=4	*R3*=2	*R4*=0.5	*hj*=0.8

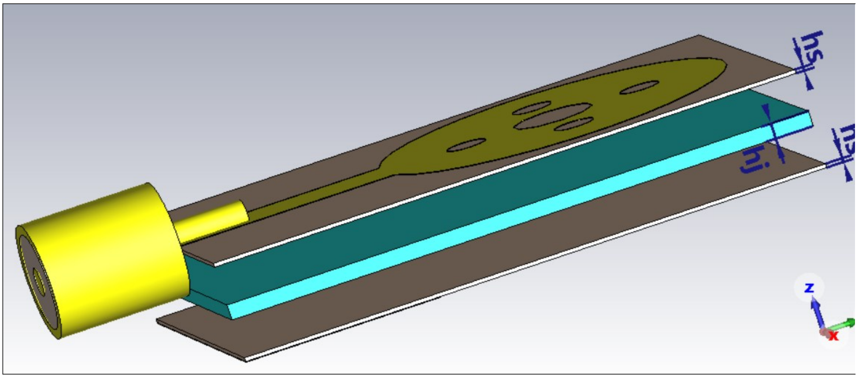

(a)

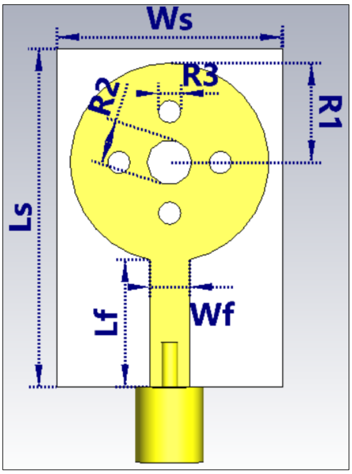

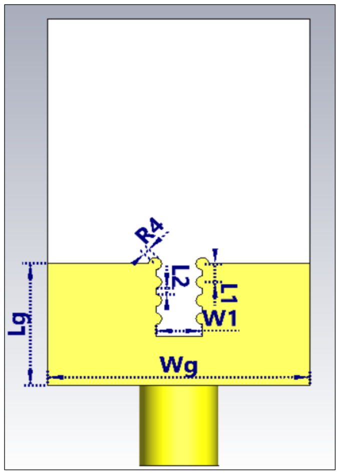

(b) (c)

Figure 3. *Designed Jean-Based UWB MMPA Geometry (a) Side View (b) Top View (c) Bottom View*

S_{11} graphs of the design stages are given in Figure 4. In order to summarize the performance of the designed antenna, voltage standing wave ratio (VSWR) and antenna gain change graphs are given in Figure 6. As seen in Figure 5, jean-based UWB MMPA radiates in the range of 3.08 GHz to 11.32 GHz. When S_{11} is below -10 dB, it is seen in Figure 6 that the antenna gain varies between 2.07 dB and 4.38 dB.

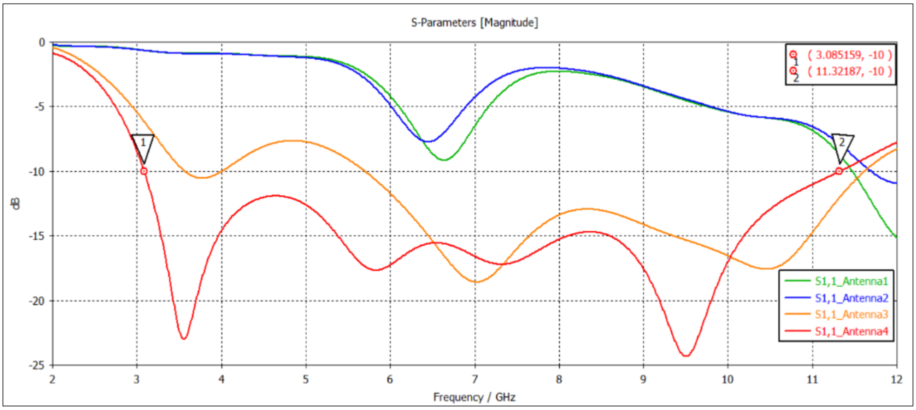

Figure 4. *S_{11} Graphs of Design Stages*

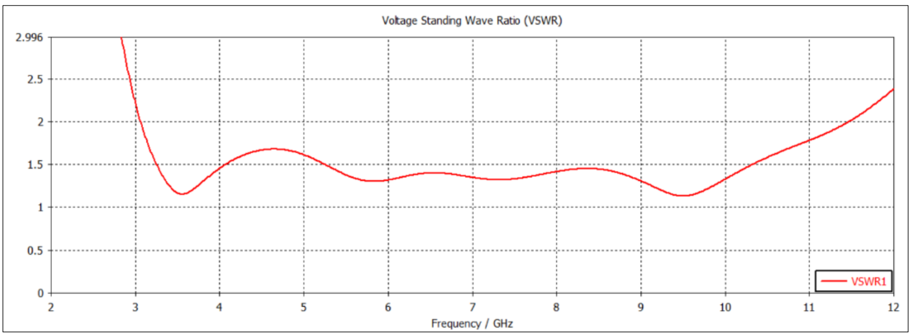

(a)

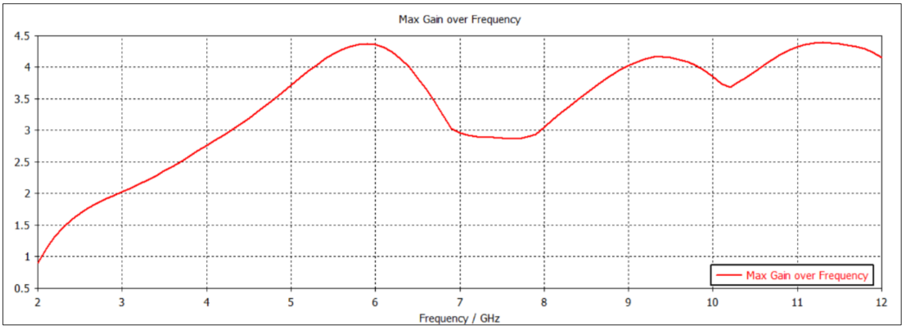

(b)

Figure 5. *Design Graphs (a) VSWR (b) Gain*

Table 2 compares the models in the literature with the simulated antenna. It is seen that all the antennas given in the table have good performance. However, the bandwidth of the study by Yang et al. is 21.5 GHz and it is larger than the size of the UWB MMPA proposed in this study. The nikrostrip antenna proposed by Irene and Rajesh takes up less space but its bandwidth is narrower. In general, it is seen that the proposed UWB MMPA takes up less space but its bandwidth is wider.

Table 2. *Comparative Results of Some UWB MMPA Designs in Literature*

	Frequency Band (GHz)	Gain (dB)	Dimension (mm)	Material
Rahmatian ve ark., 2019	3.9-10.75	≈0.25-4	61x74x3.5	PDSM
Yang ve ark., 2018	2.5-24	≈2.5-9	80x80x1	FR4
Mahmood, 2021	7-28	-	60 × 50 × 0.7	JEAN
Singh at al, 2017	3.01–5.30 & 8.12–12.35	3.693-5.46	40x 40 x 0.03	JEAN
Joshi ve Singhal, 2020	2.3-10.6	-	46x46x1.5	FR4
Bu Çalışma	**3.08-11.32**	**2.07-4.37**	**30 x 20 x 1.2**	**FR4+JEAN**

RESULTS AND DISCUSSION

A UWB MMPA design suitable for WBAN applications has been proposed. The design was carried out with CST Studio Suite software. A circular structure was preferred for the UWB MMPA design. Jean and FR4 materials were used due to their easy availability and low cost for agriculture. The proposed UWB MMPA radiates in the range of 3.08 - 11.32 GHz. The bandwidth is 8.24 GHz. The antenna gain varies between 2.07 dB and 4.37 dB during the operating frequency. UWB MMPA does not cover the operating bands such as ISM and UWB, which are among the WBAN frequency bands, and is also suitable for WiMax, WLAN, X-band applications.

REFERENCES

Balanis C.A., Anten Teorisi Analiz Ve Tasarım 3. Basımdan Çeviri, Ankara, Türkiye, 2013.

Gürsoy, G. S., & Bayer Keskin, S. E. (2021). Bant Çentik Karakteristiği Gösteren Ultra Geniş Bant Mikroşerit Anten Tasarımları Üzerine Bir İnceleme. Avrupa Bilim ve Teknoloji Dergisi(24), 314-320.

Pellegrini, A., Brizzi, A., Zhang, L., Ali, K., Hao, Y., Wu, X., & Sauleau, R. (2013). AntennasAnd Propagation for Body-Centric Wireless Communications at Millimeter-Wave Frequencies: A Review [Wireless Corner]. IEEE Antennas and Propagation Magazine, 55(4), 262-287.

Mutlu, M., & Kurnaz, Ç. (2020). Mikrodalga Görüntüleme Sistemleri için Mikroşerit Anten Tasarımı. Avrupa Bilim Ve Teknoloji Dergisi 129-137.

Joshi, A., & Singhal, R. (2020). Probe-Fed Hexagonal Ultra Wideband Antenna Using Flangeless SMA Connector. Wireless Personal Communications, 110(2), 973-982.

Rahmatian, P., Moradi, E., & Movahhedi, M. (2019, April). Single Notch Band UWB Off-Body Wearable Antenna with Full Ground Plane. In 2019 27th Iranian Conference on Electrical Engineering (ICEE) (Pp. 1228-1232). IEEE.

Yang, D., Hu, J., & Liu, S. (2018). A Low Profile UWB Antenna for WBAN Applications. IEEE Access, 6, 25214-25219.

Mahmood, S. N., Ishak, A. J., Saeidi, T., Soh, A. C., Jalal, A., Imran, M. A., & Abbasi, Q. H. (2021). Full ground ultra-wideband wearable textile antenna for breast cancer and wireless body area network applications. Micromachines, 12(3), 322.

Singh, V. K., Dhupkariya, S., & Bangari, N. (2017). Wearable ultra wide dual band flexible textile antenna for WiMax/WLAN application. Wireless Personal Communications, 95(2), 1075-1086.

https://www.3ds.com/products/simulia/cst-studio-suite (Access: 01.12.2024).

CHAPTER V

Artificial Intelligence-Based Methods for Arc Fault Diagnosis in Photovoltaic Systems: Challenges, Trends, and Future Directions

Kübra Nur AKPINAR[1]
Zühal POLAT[2]

Introduction

The effects of global warming are becoming increasing every day, making photovoltaic (PV) technologies a key resource in achieving the goals of "Climate Action" and "Affordable and Clean Energy," two of the Sustainable Development Goals. PV technologies are considered a vital alternative to carbon-based fuels for electricity generation, offering countries a clean energy source

[1] Dr., Marmara University, Vocational School of Technical Sciences, Department of Electricity and Energy, Istanbul /Türkiye, Orcid: 0000-0003-4579-4070, knur@marmara.edu.tr
[2] Asst.Prof., Marmara University, Vocational School of Technical Sciences, Department of Electricity and Energy, Istanbul /Türkiye, Orcid: 0000-0002-0234-4662, zuhalpolat@marmara.edu.tr

while ensuring energy security and independence (Lazaroiu et. al., 2023). To ensure the efficient and safe operation of PV systems, the likelihood of faults must be minimized.

Detecting faults in PV systems is essential, as undetected issues can lead to significant energy losses—sometimes up to 10% (Thakur et. al., 2023). Potential faults in a PV system include connection faults, arc faults, ground faults, line-to-line faults, and shading problems. (Al-Katheri et. al., 2022). Connection faults typically arise from errors during the production or assembly processes of PV modules, negatively affecting energy production efficiency. DC arc faults, particularly common in PV systems, occur due to sparks in the air or weak dielectric materials becoming conductive. These faults often result from loose electrical connections, inadequate insulation, or environmental factors such as humidity. Detecting and preventing such faults is critical for ensuring the safe and efficient operation of PV systems. Ground faults in a PV system generally occur due to damage to the protective insulation of normally live conductors, leading to reduced output voltage and power. If leakage currents affect a person, the consequences can be fatal. Line-to-line faults occur when there is a low-resistance connection between two points of different potentials in DC cables. These faults may result from insulation breakdown, corrosion-induced insulation failure, or mechanical damage. Such faults can lead to overcurrent, potentially damaging the DC system and conductors, increasing the risk of fire, and reducing overall efficiency. Shading effects, unique to PV panels, occur when certain modules are blocked from receiving sunlight. This reduces the current and, consequently, the maximum current of other series-connected panels. This effect can be mitigated using bypass diodes. Series arcs can form in cable connections, junction boxes, and PV modules, while parallel arcs occur when two conductors with different voltages are placed close together. Parallel arcs can disable the entire PV string where the fault occurs, often leading to bypass diode failures and even fires. Unlike the other faults mentioned in this section, arc faults are transient phenomena, and modeling their transient behavior requires complex techniques.

An example of faults that can occur in PV panels, as a representative DC system, is illustrated in Figure 1

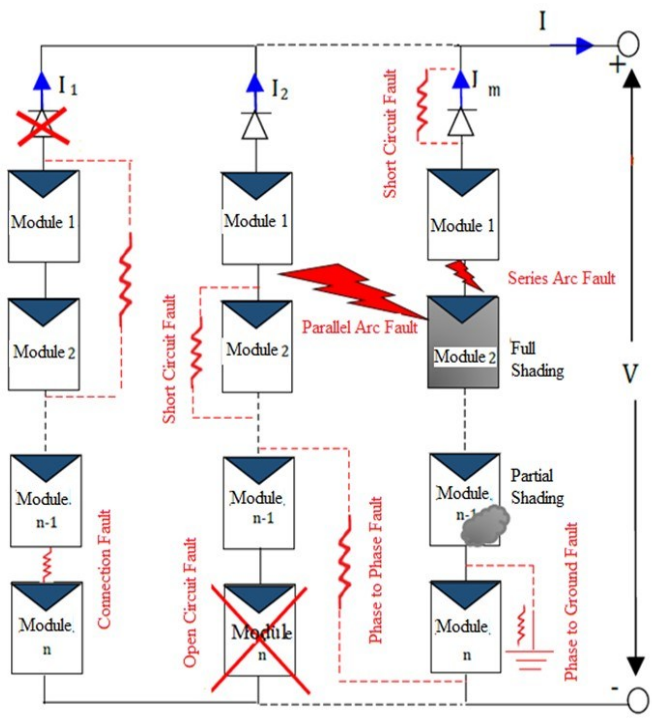

Figure 1. Fault Types in PV Systems

Arc faults in PV systems are especially critical among potential fault scenarios, as they can quickly develop into severe hazards, causing equipment damage, fires, and significant risks to human safety. (Islam et. al., 2023; Thakfan & Bin Salamah, 2024). An arc fault is defined as the sustained release of electrical energy through an insulating medium, often accompanied by partial electrode vaporization. This phenomenon typically arises from factors such as insulation degradation, weakened electrical connections, humidity, or reduced insulation strength in conductors. (Thakur et. al., 2023).

Traditional electrical protection devices often struggle to detect faults, especially at low current levels. In PV systems, factors such as temperature, irradiation, and pressure further complicate the detection of arc faults under variable conditions (Lu et. al., 2020). Advanced data processing and analysis techniques, particularly those leveraging Artificial Intelligence (AI) and Machine Learning (ML), are being employed to enhance the detection and classification of arc faults as distinct failure modes (Mellit & Kalogirou, 2022; Thakfan & Bin Salamah, 2024).

Fundamentals of Arc Faults in PV Systems

Types of Arc Faults

Two major categories of arc faults exist in PV systems, each with distinct signals and implications:

- *Series Arc Faults:* Series arc faults happen by poorly connected terminals and occur along the typical current path, frequently at regions of high resistance. Significant thermal energy may be produced by the intermittent sparking at the fault area, even if the current is still somewhat limited by the PV array characteristics (Wang et. al, 2024).

- *Parallel Arc Faults:* This can occur in PV systems between a conductor and ground or between positive and negative lines. There is a larger risk of surrounding materials being ignited by such arcs since they usually entail higher fault currents (Yuan et. al, 2022).

2.2 Arc Fault Characteristics

Since arc faults are characterized by their sudden and short-lived nature, they are challenging to identify. Several methods commonly used in the literature to define arc fault characteristics include:

- *High-Frequency Noise and Transients:* Arcing events produce broadband electromagnetic emissions, sometimes extending into the MHz range (Zhao et. al., 2023).
- *Intermittent, Rapid Fluctuations:* Arc contacts "make" and "break" continuously, leading to irregular current and voltage waveforms.

Advanced sensing and data analytics are essential to identify the irregular changes of an arc signal.

AI-Based Arc Fault Diagnosis Methods

Conventional Approaches

Arc fault detection methods typically involve monitoring threshold levels, where voltage or current exceeding set limits triggers an alarm (Thakfan & Bin Salamah, 2024; Lu et. al., 2018).

Other approaches include filtering specific frequency ranges to detect arc signals (Gao & Yu, 2022) and using techniques like Fast Fourier Transform (FFT) or wavelet transforms for spectral analysis (Lu et. al., 2018). However, PV systems often operate in noisy conditions due to inverter switching harmonics, changing weather, and partial shading (Osmani et. al, 2023). These factors can hide or mimic arc fault signals, leading to false alarms and reduced accuracy. Although these threshold-based or frequency-filtering techniques provide a foundation for detecting arc faults, they often struggle with varying environmental noise and partial shading. To address these challenges, researchers have explored AI-based methods that offer adaptive learning and robust pattern recognition capabilities.

AI-Based Approaches

Advantages of AI

AI-driven methods has some advantages. One of the most important advantage of these data-driven methods is their adaptive learning capability. More data could provide high accuracy to detect arc faults using only faulty and normal condition datasets. AI models can learn the data characteristics even under noisy and diverse operating environments (Wu, 2020). (Wu, 2020).

Data Types

In the detection of arc faults in PV systems, current and voltage data of the PV system, analysis of the current-voltage graph in time and frequency domains, drone images of the PV panel, and temperature analysis data on the PV panel can all be used as input data in AI algorithms. Depending on the input data type, the AI structures selected can be broadly classified as Machine Learning (ML) and Deep Learning (DL) algorithms.

Machine Learning Algorithms

In machine learning algorithms, measured or simulated arc fault data is subjected to preprocessing and feature extraction processes. In order for the raw data to work correctly according to variables such as the machine learning algorithm, data size, and data features, an appropriate preprocessing technique should be applied. There are several feature extraction methods for arc fault diagnosis in PV systems. Features can be analyzed in time-domain, frequency domain, and through statistical metrics. In time-domain analysis, the RMS value, peak amplitude, crest factor, and zero-crossing rate of the data are investigated (Lu et al., 2018). In frequency domain analysis, some transformations can be performed if necessary, such as Fourier transform, wavelet transform, or Stockwell transform. On the statistical metrics side, mean, variance, skewness, kurtosis, and signal entropy of the data are also widely used (Vergura, 2018). As a dimentional reduction technique, Principal Component Analysis (PCA) is a very useful and mostly applied method to eliminate noisy features that improves detection accuracy.

Support Vector Machines (SVMs), one of the machine learning techniques, are widely used ML algorithms with kernel functions (e.g., Radial Basis Function, RBF) that enable the classifier to model nonlinear relationships between signal features and the arc fault state (Cai & Wai, 2022). Decision Trees (DT) split data along features with the highest information gain, while Random Forest (RF) uses multiple decision trees to improve generalization and reduce overfitting (Amro et al., 2021; Luo et al., 2019). As ensemble methods, Gradient Boosting and AdaBoost combine multiple weak learners in a sequential manner, achieving robust performance in scenarios with rare events such as arc faults (Mellit & Kalogirou, 2022; Chen et al., 2018).

Deep Learning Approaches

Deep learning architectures, such as Convolutional Neural Networks (CNNs)—one of the most popular DL structures—apply convolution operations to raw data, automatically learning relevant features (Namatēvs, 2017). CNNs are also applied in many image classification areas, including PV panel arc fault diagnosis. Before training, a preprocessing step can be used on images for dimension reduction and filtering, enabling faster response times (Zhao et al., 2023; Lu et al., 2020). Convolutional layers effectively learn local patterns, while pooling layers reduce the computational load.

Images from satellites, drones, and I-V graphs are used as arc fault data in deep learning systems.

Recurrent Neural Networks (RNNs) and their variants such as Long Short-Term Memory (LSTM) or Gated Recurrent Units (GRUs) excel in modeling sequential dependencies, making them suitable for detecting intermittent or evolving arc faults over time (Wang et al., 2024; Saffari & Khodayar, 2024).

Deep learning algorithms with different applications and features can be combined by leveraging their best attributes and implementing them in a hybrid structure. Hybrid models—e.g., CNN-LSTM—combine the strengths of both approaches by extracting local features through convolutions and capturing temporal dynamics through recurrence (Abumohsen et al., 2024; Jalal et al., 2024).

Robustness and Real-Time Considerations

Especially enough trained AI algorithms are robust to environmental or power electronic noise. (Yuan et. al, 2022; Jalal et. al., 2024). FPGAs can handle high sampling rates in real time applications (Rodríguez-Andina et. al., 2015).

Implementation Considerations

All AI models are fundamentally data-dependent, as their learning process is inherently driven by the data they are trained on, which means that the quality and availability of the training data are critically important. However, generating arc fault data in real-time laboratory experiments is challenging. Producing arc faults under realistic operating conditions requires strict safety protocols. Moreover, carefully installed and regularly maintained PV systems rarely experience arcing, which can result in unstable datasets (Wiles, 2001). PV systems operate under highly variable conditions depending on environmental factors, grid specifications, and grid operations. Consequently, datasets obtained from laboratory experiments or simulations may not enable AI models to achieve high accuracy in real-world scenarios (Mellit & Kalogirou, 2022; Yuan et. al, 2022).

Data augmentation and preprocessing, including noise filtering to remove high-frequency interference (Chen et. al., 2019), normalization to scale data for reduced training complexity (Singh & Singh, 2020), and synthetic data generation to enhance robustness

(Modi et. al., 2024), can be applied during the AI training step, depending on sensor sampling rates and hardware capabilities.

Detection delay is a critical factor in arc fault detection because arcs can quickly happen into serious hazards if not addressed promptly. Embedded GPUs and specialized AI accelerators (ASICs etc.) and FPGAs enable fast, on-site inference with minimal delay (Capra et. al., 2020; Siegel et. al., 2018). Pruning, quantization, and knowledge distillation are examples of model compression approaches that further minimize model size and inference time. (Li et. al., 2023). Additionally, many regions are adopting standards for arc fault circuit interrupters (AFCIs), such as UL 1699B in the United States. These standards provide trustable detection with a high accuracy for arc signals while minimizing false alarms (Lu et. al. 2018). Ensuring explainability in decision-making will be critical for meeting regulatory requirements and supporting accountability (Hassan et. al., 2024, 2018; Lu et. al., 2018).

Challenges and Limitations

One driveback of AI-based tecniques is need to more data for well-train. Small sampling rate give a detailed information about the data and thus abrupt changes could not missed. On the other hand, large data sets could risk the overfitting. By avoiding this regularization techniques, careful hyperparameter tuning, and cross-validation are essential (Lu et. al., 2020; Yuan et. al, 2022). Arc faults in PV systems are not very common but has a damaged effect. Realizing the arc fault for thraining the AI-based algorithm in a real PV systems is economically not available. Synthetic data generation may cause an imbalance. (Chen et. al., 2018). There are many combinations in PV systems include the panel type, inverter type and design, array configuration and environmental factors such as dust, temperature and irradiance. Depending on the AI-architecture, transfer learning approaches offer solutions to different possibilities (Wang et. al, 2024; Jalal et. al., 2024). PV systems are used to connect to the grid or directly feed the consumers. In remote or off-grid PV systems, hardware limitations may restrict the complexity of AI models. Architecture and hardware optimizations can address these constraints (Capra et. al., 2017; Mao et. al., 2024). As PV systems integrate into smart grids, cybersecurity is another important issue. Security attacks could manipulate sensor streams or AI models themselves, compromising detection reliability (Ye et. al., 2021).

Current Trends and Future Directions

Today, the development of low-power and high-performance computing modules such as Google Coral allows AI engineers to run more complex AI models such as quantization and knowledge distillation (Verhelst et. al., 2017; Alhussain, 2024; Li et. al., 2023). Because of dataset differences, models that have been trained perform poorly when used in other scenarios. Reusing knowledge obtained from a source domain to boost learning in a target domain is the goal of transfer learning. Pretrain models can leverage large datasets to initialize network weights and speed up convergence (Wang et. al, 2024; Jalal, 2024). Domain Adversarial Training methods aligning feature distributions between source and target domains can mitigate the negative effects of domain shifts (Li & Tan, 2023). Researchers use to data from thermal imaging, acoustic sensors, and advanced power quality meters to detect the full spectrum of arc-fault signals (Lu et. al., 2018). Mixing heterogeneous data using AI can support detection confidence. It is important to understand the cause of an alert as AI-driven fault detection systems become a crucial part of safety-critical processes. Technicians can test or debug detections by using techniques like SHAP (SHapley Additive exPlanations) or LIME (Local Interpretable Model-Agnostic Explanations), which can disclose model reasoning (Hakkoum et. al. 2024). In PV systems integration to a smart grid, arc fault detection and higher-level grid control could improve all system performance monitoring arc fault signals and degradation patterns to schedule proactive maintenance (Mahmoud et. al., 2021; Chen et. al., 2018), coordinating arc fault detection with other protection mechanisms to isolate problematic arrays or reconfigure power flows in real time.

Conclusion

Arc faults are a critical challenge and research focus for ensuring the safety and reliability of photovoltaic (PV) systems. Traditional detection methods rooted in threshold or frequency based analyses are often ill suited to the diverse environmental conditions, system variations, and noise common in PV arrays. AI-based approaches, however, have shown significant promise by learning complex arc fault signatures and adapting to new operating scenarios.

Crucial to this success is thorough data collection and preprocessing, which ensure that AI-based algorithms receive high-quality inputs. In PV systems, these algorithms must handle fluctuating solar irradiance, varying temperatures, and hardware differences across multiple installations. Beyond collecting robust datasets, it is also vital to assess the risk of model overfitting, where algorithms can accurately recognize stable and variable signals in training but fail in new situations. Implementing advanced regularization techniques can bolster reliability in real-world applications.

Meanwhile, practical deployment in off-grid or remote sites demands careful attention to hardware constraints and cybersecurity measures. Locales with limited connectivity or energy resources benefit from compressed and optimized models that reduce computational load. As power infrastructures become increasingly interconnected, safeguarding sensitive data is equally essential. Secure communication protocols and strong encryption can defend system integrity while maintaining operational performance.

By integrating considerations like high-quality data practices, strategies against overfitting, hardware optimization, and robust cybersecurity, AI-driven arc fault detection can significantly enhance the resilience and efficiency of next-generation PV systems.

References

Abumohsen, M., Owda, A. Y., Owda, M., & Abumihsan, A. (2024). Hybrid machine learning model combining of CNN-LSTM-RF for time series forecasting of Solar Power Generation. *e-Prime-Advances in Electrical Engineering, Electronics and Energy*, *9*, 100636. https://doi.org/10.1016/j.prime.2024.100636

Ahmed, S. F., Alam, M. S. B., Hassan, M., Rozbu, M. R., Ishtiak, T., Rafa, N., ... & Gandomi, A. H. (2023). Deep learning modelling techniques: current progress, applications, advantages, and challenges. *Artificial Intelligence Review*, *56*(11), 13521-13617.Springer.

Alhussain, A. (2024). Efficient Processing of Convolutional Neural Networks on the Edge: A Hybrid Approach Using Hardware Acceleration and Dual-Teacher Compression. *University of Central Florida*. Graduate Thesis.

Al-Katheri, A. A., Al-Ammar, E. A., Alotaibi, M. A., Ko, W., Park, S., & Choi, H. J. (2022). Application of artificial intelligence in PV fault detection. *Sustainability, 14*(21), 13815. https://doi.org/10.3390/su142113815

Amro, A., Al-Akhras, M., Hindi, K. E., Habib, M., & Shawar, B. A. (2021). Instance reduction for avoiding overfitting in decision trees. *Journal of Intelligent Systems*, *30*(1), 438-459. https://doi.org/10.1515/jisys-2020-0061

Cai, X., & Wai, R. J. (2022). Intelligent DC arc-fault detection of solar PV power generation system via optimized VMD-based signal processing and PSO–SVM classifier. *IEEE Journal of*

Photovoltaics, *12*(4), 1058-1077. 10.1109/JPHOTOV.2022.3166919.

Capra, M., Bussolino, B., Marchisio, A., Masera, G., Martina, M., & Shafique, M. (2020). Hardware and software optimizations for accelerating deep neural networks: Survey of current trends, challenges, and the road ahead. *IEEE Access*, *8*, 225134-225180. 10.1109/ACCESS.2020.3039858.

Chen, S., Li, X., Meng, Y., & Xie, Z. (2019). Wavelet-based protection strategy for series arc faults interfered by multicomponent noise signals in grid-connected photovoltaic systems. *Solar Energy*, *183*, 327-336. https://doi.org/10.1016/j.solener.2019.03.008.

Chen, Z., Han, F., Wu, L., Yu, J., Cheng, S., Lin, P., & Chen, H. (2018). Random forest based intelligent fault diagnosis for PV arrays using array voltage and string currents. *Energy conversion and management*, *178*, 250-264. https://doi.org/10.1016/j.enconman.2018.10.040.

Hakkoum, H., Idri, A., & Abnane, I. (2024). Global and local interpretability techniques of supervised machine learning black box models for numerical medical data. *Engineering Applications of Artificial Intelligence*, *131*, 107829. https://doi.org/10.1016/j.engappai.2023.107829.

Hassan, I., Alhamrouni, I., Younes, Z., Azhan, N. H., Mekhilef, S., Seyedmahmoudian, M., & Stojcevski, A. (2024). Explainable Deep Learning Model for Grid Connected Photovoltaic System Performance Assessment for Improving System

Relaibility. *IEEE Access*. https://doi.org/10.1109/ACCESS.2024.3452778.

Islam, M., Rashel, M. R., Ahmed, M. T., Islam, A. K., & Tlemçani, M. (2023). Artificial intelligence in photovoltaic fault identification and diagnosis: A systematic review. *Energies*, *16*(21), 7417. https://doi.org/10.3390/en16217417.

Kumar, P., Kumar, M., & Bansal, A. K. (2024). Automatic Fault Detection of Photovoltaic Modules Using Recurrent Neural Network. *Russian Electrical Engineering*, *95*(4), 321-334. https://doi.org/10.3103/S1068371224700330.

Lazaroiu, A. C., Gmal Osman, M., Strejoiu, C. V., & Lazaroiu, G. (2023). A comprehensive overview of photovoltaic technologies and their efficiency for climate neutrality. *Sustainability*, *15*(23), 16297. https://doi.org/10.3390/su152316297

Li, Z., Li, H., & Meng, L. (2023). Model compression for deep neural networks: A survey. *Computers*, *12*(3), 60. https://doi.org/10.3390/computers12030060

Lu, S., Sahoo, A., Ma, R., & Phung, B. T. (2020, October). DC series arc fault detection using machine learning in photovoltaic systems: Recent developments and challenges. In 2020 8th International Conference on Condition Monitoring and Diagnosis (CMD) (pp. 416-421). IEEE. 10.1109/CMD48350.2020.9287192

Lu, S., Phung, B. T., & Zhang, D. (2018). A comprehensive review on DC arc faults and their diagnosis methods in photovoltaic systems. Renewable and Sustainable Energy Reviews, 89, 88-98. https://doi.org/10.1016/j.rser.2018.03.010

Mahmoud, M. A., Md Nasir, N. R., Gurunathan, M., Raj, P., & Mostafa, S. A. (2021). The current state of the art in research on predictive maintenance in smart grid distribution network: Fault's types, causes, and prediction methods—A systematic review. *Energies*, *14*(16), 5078. https://doi.org/10.3390/en14165078

Mao, Y., Weiss, R., Zhang, Y., Li, Y., Rothmann, M., & Porrmann, M. (2024, May). FPGA Acceleration of DL-Based Real-Time DC Series Arc Fault Detection. In *2024 IEEE International Parallel and Distributed Processing Symposium Workshops (IPDPSW)* (pp. 92-98). IEEE. 10.1109/IPDPSW63119.2024.00031.

Mellit, A., & Kalogirou, S. (2022). Assessment of machine learning and ensemble methods for fault diagnosis of photovoltaic systems. *Renewable Energy*, *184*, 1074-1090. https://doi.org/10.1016/j.renene.2021.11.125.

Modi, S., Bokkena, B., Avhad, P., Kshirsagar, V., Dahiya, T., & Parikh, T. (2024, September). Automated Synthetic Data Generation Pipeline Using Large Language Models for Enhanced Model Robustness and Fairness in Deep Learning Systems. In *2024 3rd International Conference for Advancement in Technology (ICONAT)* (pp. 1-6). IEEE.

Namatēvs, I. (2017). Deep convolutional neural networks: Structure, feature extraction and training. *Information Technology and Management Science*, *20*(1), 40-47. doi: 10.1515/itms-2017-0007

Osmani, K., Haddad, A., Lemenand, T., Castanier, B., Alkhedher, M., & Ramadan, M. (2023). A critical review of PV systems' faults with the relevant detection methods. *Energy Nexus*, 100257. https://doi.org/10.1016/j.nexus.2023.100257

Rodríguez-Andina, J. J., Valdes-Pena, M. D., & Moure, M. J. (2015). Advanced features and industrial applications of FPGAs—A review. *IEEE Transactions on Industrial Informatics*, *11*(4), 853-864. 10.1109/TII.2015.2431223

Saffari, M., & Khodayar, M. (2024). Spatiotemporal Deep Learning for Power System Applications: A Survey. *IEEE Access*. 10.1109/ACCESS.2024.3424854

Siegel, J. E., Pratt, S., Sun, Y., & Sarma, S. E. (2018). Real-time deep neural networks for internet-enabled arc-fault detection. *Engineering Applications of Artificial Intelligence*, *74*, 35-42. https://doi.org/10.1016/j.engappai.2018.05.009

Singh, D., & Singh, B. (2020). Investigating the impact of data normalization on classification performance. *Applied Soft Computing*, *97*, 105524. https://doi.org/10.1016/j.asoc.2019.105524

Thakfan, A., & Bin Salamah, Y. (2024). Artificial-Intelligence-Based Detection of Defects and Faults in Photovoltaic Systems: A Survey. *Energies*, *17*(19), 4807. https://doi.org/10.3390/en17194807

Thakur, K., Dwivedi, D., Babu, K., Parimi, A. M., Yemula, P. K., Chakraborty, P., & Pal, M. (2023). Advancements in arc fault detection for electrical distribution systems: A comprehensive review from artificial intelligence perspective. *arXiv Preprint, arXiv:2311.16804*. https://doi.org/10.48550/arXiv.2311.16804

Vergura, S. (2018). A statistical tool to detect and locate abnormal operating conditions in photovoltaic systems. *Sustainability*, *10*(3), 608. https://doi.org/10.3390/su10030608

Verhelst, M., & Moons, B. (2017). Embedded deep neural network processing: Algorithmic and processor techniques bring deep learning to iot and edge devices. *IEEE Solid-State Circuits Magazine*, *9*(4), 55-65. 10.1109/MSSC.2017.2745818

Jalal, M., Khalil, I. U., & ul Haq, A. (2024). Deep Learning approaches for visual faults diagnosis of photovoltaic systems: State-of-the-art review. *Results in Engineering*, 102622. https://doi.org/10.1016/j.rineng.2024.102622

Wang, Y., Zhou, J., Paul, K. C., Zhao, T., & Sheng, D. (2024). Explainability Approach-Based Series Arc Fault Detection Method for Photovoltaic Systems. *IEEE Access*. 10.1109/ACCESS.2024.3381530

Wiles, J. (2001). *Photovoltaic power systems and the national electrical code: suggested practices* (No. SAND2001-0674). Sandia National Lab.(SNL-NM), Albuquerque, NM (United States); Sandia National Lab.(SNL-CA), Livermore, CA (United States).

Wu, Y. (2020). Robust learning-enabled intelligence for the internet of things: A survey from the perspectives of noisy data and adversarial examples. *IEEE Internet of Things Journal*, *8*(12), 9568-9579. 10.1109/JIOT.2020.3018691

Ye, J., Giani, A., Elasser, A., Mazumder, S. K., Farnell, C., Mantooth, H. A., ... & Abbaszada, M. A. (2021). A review of cyber–physical security for photovoltaic systems. *IEEE Journal of Emerging and Selected Topics in Power Electronics*, *10*(4), 4879-4901. 10.1109/JESTPE.2021.3111728

Yuan, Z., Xiong, G., & Fu, X. (2022). Artificial neural network for fault diagnosis of solar photovoltaic systems: a survey. *Energies*, *15*(22), 8693. https://doi.org/10.3390/en15228693

CHAPTER VI

A Review on Wearable Antennas and Electronic Textiles

Naciye Sündüz OĞUZ[1]
Bilge ŞENEL[2]

1- Introduction

Using advanced technology in technical textiles has been of great importance for the textile industry as it produces high-performance, easy-to-use, faster-produced, high-value-added products. Mechanical properties such as high strength, reinforcement, and elasticity from technical textiles; switching properties such as filtering, transmission, insulation; human health-related properties such as biodegradable, compatible with the body,

[1] Lecturer Dr. Naciye Sündüz OĞUZ, Kastamonu University, Araç Rafet Vergili Vocational School, Department of Textile, Clothing, Shoes and Leather, Kastamonu/ Turkey, Orcid: 0000-0002-3640-8038, noguz@kastamonu.edu.tr.
2
[2] Assistant Professor Bilge Şenel, Süleyman Demirel University, Faculty of Engineering and Natural Sciences/Department of Electrical-Electronic Engineering, Isparta/Turkey, Orcid: 0000-0003-3612-936X, bilgeturkel@sdu.edu.tr .

non-toxic, non-reactive; to provide protection against heat, radiation, electricity, chemical, biological and mechanical effects are expected (Horrocks and Anand, 2000; Arslan, 2009).

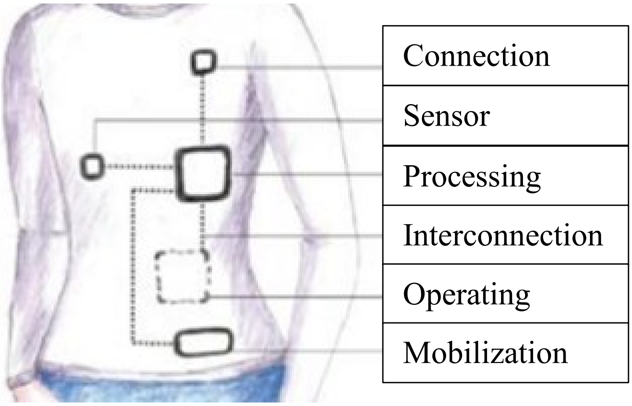

Figure 1: Smart textile product (Schwarz vd., 2010)

As seen in Figure 1, connection, sensor, data processing, interconnection, operation, and activation functions are expected from smart textile products. However, there is no need for all of these functions to be together (Schwarz et al., 2010). Smart textiles: They are the textile products among technical textiles that have high added value, bring together different disciplines and are the most open to development. These products are products that detect environmental changes and react to these change (Gürcüm et al., 2015). Since the 1980s, conductive textile products began to appear on the market, and studies in the fields of health and military began to be carried out (Smith, 1988). Fibers are made conductive or semiconductor from metal sheets and tapes by drawing methods, metal oxides and salts, conductive carbon and polymers (Kim et al., 2004; Anderson & Seyam). Conductivity is achieved in threads conductive filaments, staple conductive fibers, and non-conductive textile fibers by spinning with conductive fibers and wires, and by coating non-conductive threads with conductive materials (Uyanık, 2021).

Conductive fabrics are obtained by using conductive threads and wires and applying conductive materials to the fabric. In these applications, the chemical coating method is the most used method. These products are washable (Gürcüm et al., 2015; Sünter et al., 2010). Thanks to electronic textiles, it has been observed that these products, in which vital functions such as blood pressure, pulse and temperature are measured, recorded, stored, and transmitted via radio waves, provide great convenience to military and healthcare personnel, police officers, firefighters and patients. The aim of such products is to produce smart clothing by integrating circuit elements into the textile surface. The system works by evaluating the signal from the sensor in the processor and displaying the results on the screen. In this way, vital functions of people can be monitored remotely (Gürcüm et al., 2015).

2. Wearable Antennas

In the research conducted by the Turkish Statistical Institute in 2019, it was seen that the highest death rate was caused by diseases originating from the circulatory system. Heart diseases have the largest share among diseases caused by the circulatory system. The methods used today to detect heart diseases have different difficulties and disadvantages. Microstrip antennas are used in medical imaging and diagnostic systems due to their low cost and weight, small size, and multi-band nature. A frequency band that does not harm human health and does not emit ionizing radiation is used. Microstrip antennas are used to detect vascular occlusions and types of cancer by using different base materials such as cotton, denim, and foam (Uyanık, 2021).

Voltage sensors, pressure sensor, electrochemical sensors, planar fashionable circuit board, wearable antenna are conductive materials used as sensors (Erol & Çetiner, 2017). With the rapid progress in conductive textiles, wearable antennas using compatible and flexible smart structures have gained great importance (Giddens et al., 2012). Other electronic parameters can be monitored by transmitting information from the sensors in the clothing via the antenna (Stoppa & Chiolerio, 2014). To obtain good results from wearable antennas, they are required to be robust, light, cheap, thin, low maintenance, and easy to integrate into radio frequency circuits. Wearable antennas integrate clothing into the communication system, making electronic devices less disruptive (Wang et al., 2012; Gupta et al., 2010). Miniaturization of circuits, elastic applications, and the use of nano-sized materials have made wearable technology popular. Wearable textile products, which were initially used for applications that could be considered luxury, have been shown to have great importance in healthcare and military fields over time. Since the antenna size decreases at high frequencies, the antennas used for this purpose are microstrip antennas. It is important to choose comfortable and durable fabric in wearable antenna applications (Albairaqdar, 2018). Thanks to wearable textile products, people's health status can be monitored remotely, and necessary care can be provided.

To avoid undesirable effects while the device is operating, the textile antenna must be placed correctly, it must be made with the correct thickness by stacking different fabrics, the geometric dimensions of the patch must remain constant, the connections between layers must not affect the electrical properties, and the connections of electronic clothing with other parts must be strong and stable (Ouyang & Chappell, 2008; Matthews & Pettitt, 2009). As seen in Figure 2, wearable antennas can be easily integrated into the fabric without causing any discomfort to the human body or restricting the user's mobility. These products become functional by placing them in different parts of the human body such as the head, chest, arms and legs (Bilgin, 2016). Smart helmets, infotainment systems, military clothing on the head; smart glasses, smart contact lenses on the eye; medical smart clothing, physical activity tracker, skin patch, sportswear on the arm; smart shoes, medical devices, military, sports clothing on the leg and foot; hearing aid, smart headset, smart earrings on the ear; smart clothes chest belt (band), medical skin patch, smart bracelet on the wrist, smart bracelet, fitness tracker on the body and multifunctional integrable products are used by users (Kılıç, 2017).

Figure 2: Examples of wearable antennas (Albairaqdar, 2018; Hertleer et al., 2010)

2.1. Microstrip Antennas

Microstrip antennas consist of conductive radiation elements placed on the dielectric material and the metal layer under the insulating material serving as the ground plane. The patch where the radiation process is performed is selected from low-loss metallic materials or textile-based materials such as denim, velvet and felt. The size and thickness of the patch, the thickness of the material used as the insulating base, and the dielectric constant affect the antenna performance (Uyanık, 2021).

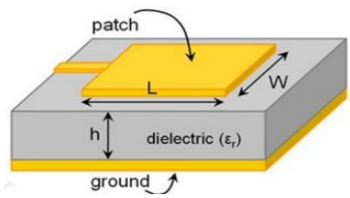

Figure 3. Structure of the microstrip antenna (Farad & Dixit, 2014)

The upper part of the microstrip antenna is the patch. L is the length, W is the width, the bottom part is the ground, and there is h electrical insulator between the patch and the ground. Microstrip antennas are in the form of square, rectangle, circle, triangle, ellipse, and dipole. Generally, circular, or rectangular microstrip antenna patches are preferred in studies (Yousefalturk & Cansız, 2022).

2.1.1. Feeding techniques of microstrip antennas

Microstrip feeding is the feeding method in which the microstrip line is directly connected to the antenna patch. The microstrip line is flush with the patch. The width of the patch is generally larger than the width of the microstrip line. Structurally advantageous microstrip feeding is shown in Figure 4 (Gökdemir, 2022; Balanis, 2005).

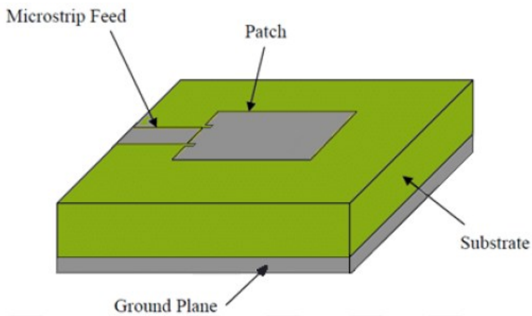

Figure 4: Microstrip antenna feeding (Balanis, 2005)

Microstrip antennas are fed by contact and non-contact methods. With the contact method, the RF signal is transmitted directly to the antenna patch using a connector. In the non-contact method, electromagnetic coupling is used between the radiating patch and the supply line. Many methods have been developed using these two main methods. Coaxial feeding, microstrip line feeding, proximity coupled, and aperture coupled feeding are the most preferred techniques (Balanis, 2016). Microstrip line feed is the easiest and most widely used feed type to connect and produce (Yousefalturk & Cansız, 2022).

2.1.2. Analysis Models of Microstrip Antennas

The cavity model, transmission line model and full wave model are the most used models to analyze microstrip antennas. The microstrip line cross-section is shown in Figure 5 (Yousefalturk & Cansız, 2022).

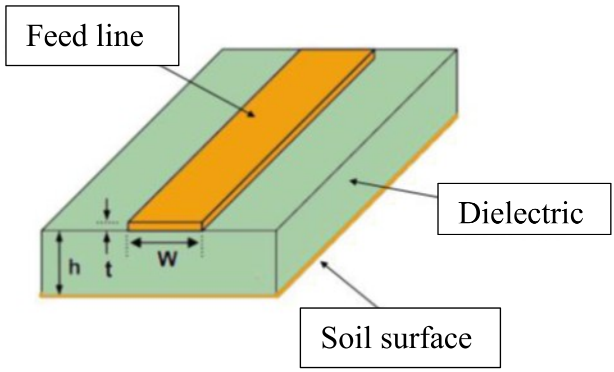

Figure 5. Microstrip line section (Yousefalturk & Cansız, 2022)

For thin dielectric profiles, the transmission line model is a method with a high degree of accuracy (Ataş, 2009). The gap model has higher accuracy than the transmission line model but is complex (Derneryd, 1978; Wang vd., 2008). It is the full wave model that has the most accuracy compared to other models (Patel et al., 2017). With the development of technology, microstrip antennas are used in many areas such as doppler and other radars, mobile communications, guided missiles, biomedical measurements, satellite communications, and the internet of things. Microstrip antennas have many advantages such as being small and light, ease of design, low cost, ease of fabrication, compatibility of their planar structure with the environment, easy integration with microwave integrated circuits, development on the same base material as circuit assemblies, and easy connection to devices requiring precision due to their surface compatibility while preserving their aerodynamic structure. It has disadvantages such as low gain factor, narrow bandwidth, unwanted stray radiation, low power carrying capacity, vulnerability to external excitations in surface waves, and half-plane radiation due to the feed structure. Microstrip antennas are used in areas such as Doppler and other radars, mobile communications, guided missiles, satellite communications, internet of things and biomedical measurements (Balanis, 2016).

Wearable microstrip antennas are integrated into clothing for sensing and processing purposes with improving users' safety and comfort. Cotton, polyester, nylon, insulated wire, foam, conductive paint, liquid crystal polymer, etc. A wearable antenna integrated into the textile surface has been produced. Microstrip patch antennas can be easily integrated into clothing due to their advantages such as low cost, low volume, light weight, can be designed in the desired geometric shape, are easy to install almost maintenance-free, and do not cause electromagnetic damage (Albairaqdar, 2018).

3. Usage Areas of Wearable Textiles

Wearable textiles are used in many sectors such as health, military, sports, entertainment, education, fashion facilitating the user's lifestyle and providing comfort to the user. Studies in this field are increasing day by day.

3.1. Industrial Applications

The first examples in the field of industrial applications were introduced by Boeing in the 1990s. The aim of this head-mounted device is to facilitate and speed up the assembly process of the employee using augmented reality, without the need for reference notes (Thomas & David, 1992).

3.2. Military Applications

Wearable computer systems provide great convenience in the combat training of soldiers by using augmented reality. “Quantum 3D Expedition”, created using augmented reality, is a wearable system used for training soldiers by creating a virtual war environment. This system, which detects sounds and commands coming from outside, protects soldiers against possible dangers, enables them to cooperate with each other, and reduces the cost of preparing training environments (Quantum3D Training, Simulation, Technology, 2024).

3.3. Applications in the Field of Health

Applications in the field of health were developed by NASA in the 1960s with the need to monitor the vital data of astronauts, and then developed with the aim of monitoring the health status of soldiers. The "Personnel Status Monitor" system was designed to detect when soldiers are tired and injured. Health practices are of great importance in monitoring and treating patients and facilitating surgeries (Bilgin, 2016).

3.4. Applications in the Entertainment Industry

Although not as intense as in the military and healthcare fields, three-dimensional (3D) virtual reality is used in the entertainment industry (Bilgin, 2016).

3.5. Applications in the Field of Education

Wearable textiles have been used and developed in the field of education to improve teaching, increase interaction in the classroom environment, and concretize abstract concepts of students (Canbaz & Yalçın, 2021). In Korea, in 2015, an e-textile shirt called BodyVis was aimed to teach primary school students about internal organs (Norooz et al., 2015).

3.6. Applications in Fashion

In fashion applications, wearable textiles are integrated into clothing and accessories, providing users with great comfort and style. Clothes that can measure the wearer's body temperature, adrenaline and stress level, color-changing night dresses, solar-powered jackets, backpacks that react to air pressure, body temperature, touch, wind and sunlight, scarves, phone cases, clothes that change shape by moving and also glow-in-the-dark clothing is used (Olewitz, 2016; Borg, 2015; Tommy Hilfiger Solar Clothing, 2014; Interactive Projects, 2018).

4. Wearable Patient Monitoring Systems

With the development of technology, data analysis can be performed with remote access, portable, low-cost patient monitoring systems. This system is of great importance in the diagnosis and treatment of diseases. Due to the increasing elderly population and the difficulty of the elderly in coping with diseases, the home care services they receive cause more costs and time requirements than wearable health products. Wearable health products that provide great convenience to patients and their relatives are of great importance at this point (Bilgin, 2016).

Wearable products designed to monitor health status can detect vital signals such as heartbeat, body temperature, respiratory rate, blood oxygen rate, blood pressure, electromyogram (EMG), electrocardiogram (ECG). These data detected by sensors are transmitted to the relevant experts in the health center via wireless sensor networks. Experts can identify and treat the disease through this data without the need to meet the patient face to face. In addition, patients are provided with great convenience by being able to monitor the patient's condition and call for emergency help in emergency situations (Bilgin, 2016).

In the 1960s, when NASA sent the first human into space, wearable products were used to examine the health status of astronauts. Later, these products were used to provide health services in rural settlements where there were no doctors (Kumar & Krupinski, 2008).

Wearable patient monitoring systems enable rapid and safe examination of data from patients, as well as responding to possible situations and intervening in emergencies. These systems include patient application systems between the doctor and healthcare institutions, such as telemedicine, teleradiology, teleoncology, telepathology, and between the doctor and the patient, such as home care, mobile health monitoring, telehealth, remote chronic disease monitoring, and teleconsultation. Thanks to these systems, diagnostic information such as ECG and x-ray are transmitted to the relevant person through the existing infrastructure and checked at the patient's home, providing savings in terms of time and cost (McCann & Bryson, 2022). The general structure of patient monitoring systems is shown in Figure 6.

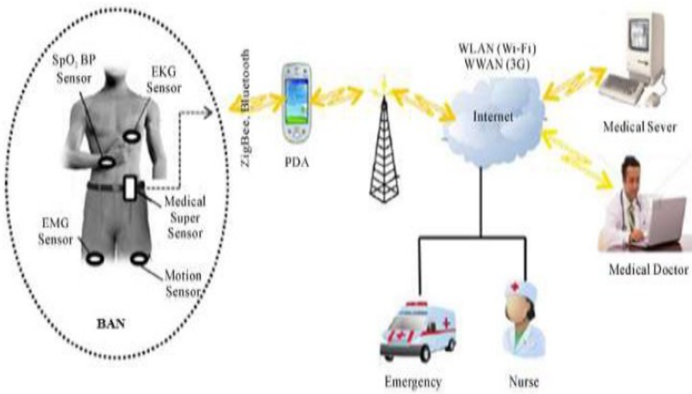

Figure 6: General Structure of Patient Monitoring Systems (Kuzubaşoğlu, 2021)

Sensors that are compatible with wireless body area networks communicate with a personal treatment server or directly via an internet network interrupt, transmitting and recording information to the treatment server where records are kept. Information from the sensors is collected in the network controller in the BAN, sent to the receiver unit and transmitted to the server. These data can also be shared with other units (Bilgin, 2016).

Produced by BodMedia in the 1990s, the wearable device placed on the bicep of the arm can detect information such as the person's pulse rate while asleep or awake, the number of steps taken, the number of calories burned, and transfer it to devices such as tablets and smartphones. Every year, thousands of babies experience sudden infant deaths while they are asleep, so clothes have been produced that convey this situation to the parents when the baby stops breathing, changes in heartbeat and body temperature are observed. A system produced by Kiowk, a Sweden-based company, warns the patient and the staff when there is an unexpected situation in the patient's body, in cases that require early intervention, heartbeat, asthma, diabetes (Virtual Worldlets Network, 2024).

5. Textile Products Used In Wearable Antennas

Since wearable antennas are used in different parts of the human body, they should be designed using flexible, soft materials that are compatible with the human body [65, 66]. With the development of wearable antennas, studies on patch antennas have focused on flexible materials. A suitable textile base material and conductor should be selected not only for providing comfort to the user but also for the performance of the antenna (Gupta et al., 2010; Wang et al., 2016).

Materials such as cotton, denim and felt are very suitable for use as dielectric bases forming a textile antenna (Vallozzi et al., 2016; Lin et al., 2018). Textiles generally offer a very low dielectric constant, reducing surface wave losses and increasing the impedance bandwidth of the antenna. Textile antennas are physically larger than high dielectric based antennas (Elrashidi et al., 2011; Singh et al., 2015; George et al., 2013). The dielectric behavior of textile products depends on frequency, temperature, humidity, the properties of constituent fibers and the structure of the yarns and/or fabrics, and the fiber packing density in the fibrous material (Salvado et al., 2012). Dielectric constant and loss tangent values of some textile products are given in Table 1 (Dhupkariya et al., 2015).

Table 1. Dielectric constant and loss tangent of some textile products (Dhupkariya et al., 2015)

Dielectric material	**Dielectric constant ($\mathcal{E}r$)**	**Loss tangent (tanδ)**
Felt	1,22	0,016
Cotton	1,60	0,040
Denim	1,7	0,025
Polyester	1,90	0,0045
Panama	2,12	0,05
Cordura/Lycra	1,50	0,0093
Cordura	1,90	0,0098
Silk	1,75	0,012
Moleskin	1,45	0,05
Tween	1,69	0,0084
Quartzel Fabric	1,95	0,0004

As seen in Table 1, in general, textile products offer a very low dielectric constant because they are porous materials (Loss, 2017). Although these values vary depending on the manufacturer, they are a guide for antenna design (Ivšić,2013).

In general, for flexible antennas, the conductivity of the radiating part is required to be high. Electrotextile antennas have been shown to have less gain, efficiency and bandwidth compared to their copper tape or foil counterpart. Different conductor materials, such as copper tape, lead to different antenna performance (Paracha et al., 2019). Although it is very easy to stick copper tape or foil to a textile substrate, it may be removed as a result of deformation of the copper tape during bending or due to environmental conditions such as temperature and humidity (Tsolis et al., 2014).

In recent years, electro-textiles (e-textiles) have attracted much attention as promising materials for making wearable antennas fully flexible, enabling smart materials to communicate freely via wireless networks. These fabrics are durable, flexible and suitable for wearability (Ahmed et al., 2018).

Electrical properties and surface resistances of conductive textile products are usually given by expert manufacturers. Therefore, certain commercially available conductive textiles have been successfully used in antennas (Salvado et al., 2012). Some of these are produced with Shieldit Super and FlecTron, both of which have sheet resistances of less than 0.1 Ω/m^2 (Hertleer et al., 2009). These antennas have been successfully used in various WBAN applications for RF communications (Lin et al., 2018).

6. Technological Development of Wearable Antennas

Kurt & Kaya (2022), when the studies were examined, it was seen that wearable antennas are of great importance in the field of health. It has been shown that breast cancer is diagnosed with the use of microwave patch antennas, and microwave imaging is the best method for detecting breast cancer.

Erdem (2017), since electrical nerve stimulation method is an effective method to reduce the pain of diseases, such methods can be integrated into clothing thanks to electronic textiles. A therapeutic knee brace has been developed for knee osteoarthritis patients by integrating electrodes into the knee brace.

Güray (2018), electronic textile-based gloves were designed by integrating TENS (Transcutaneous Electrical Neural Stimulation) feature and textile-based splint application into electronic textiles created with the embroidery method for rheumatoid arthritis patients. As a result of this study, a decrease in pain was observed in the patients. However, difficulties in overlapping finger joints have been observed in patients with deformities due to this disease.

Güler (2007), thanks to the electronic equipment placed on the clothing using a MEMS (Micro Electromechanical Systems) based accelerometer, the vital respiratory rate was measured by determining the forward bending, upright standing, supine positions, walking and running movements of the human body. Problem-free and high-quality data transfer was achieved using the RF method for 8 hours without interruption.

Ercan (2018), it was aimed to create a wearable electronic textile resistant to high temperatures by combining different fabrics with silver, copper and steel conductive threads in sandwich form. It has been observed that silver-coated conductive threads show lower performance and breakage than copper and steel-coated threads. It is thought that these e-textile products, which are resistant to high temperatures and have high data transmission capacity, can be used in different areas such as protective clothing and space suits.

Kuzubaşoğlu (2021), wearable temperature sensors have been studied using the inkjet printing method for health and biomedical applications. It has been observed that the sensor attached to the clothes can monitor body temperature in risky situations.

Acar (2019), wearable electrocardiography (ECG) sensors have been developed for use in personal health monitoring applications. For this purpose, graphene was applied to fabrics by dipping, coating and screen-printing techniques, and heart rate rates were successfully determined. It is foreseed that this study will be effective in the refinement of wearable heart monitoring devices.

Bilgin (2016), by saving time and cost, basic health information such as body temperature, galvanic skin response, pulse rate and breathing rate have been monitored for a long time by designing a wearable mobile health system for people in risk groups such as athletes, patients and the elderly. Vital values were determined with sensors on the patient's body, and a web-based visual interface design was obtained by transferring the obtained data to experts on the internet.

Albairaqdar (2018), to realize a textile dielectric material-based microstrip antenna design, rectangular, circular, and equilateral triangular microstrip antenna designs were carried out in the 2.4, 3 and 5.8 GHz frequency band using denim, velvet and felt textile products. Antenna performances were compared by developing the Equal Patch Area (EAA) method. It has been observed that the EYA method is a successful method in determining performance and that denim, felt and velvet textile products can be used in wearable products.

Arı (2016), The electronic circuit, which enables visually impaired individuals to navigate more easily by detecting obstacles they may encounter through wireless sensors developed using high-frequency sound waves, is applied to the adhesive fabric and can be removed and used with different clothes if necessary. The receiver circuit, which can be carried in a shirt pocket, can be used easily in all clothes, providing convenience to visually impaired individuals.

Uyanık (2021), Due to the disadvantages of the methods used in the detection of heart diseases, microstrip antennas, which have advantages such as small size, weight, narrow, low cost and multi-band, have been used by integrating them with a textile-based surface. Denim and felt were used as textile surfaces in the study. Antenna design and cardiovascular tissue were designed with the simulation method through the HFSS (High Frequency Structural

Simulator) program, and this application was found to be applicable in detecting cardiovascular occlusion.

Mutlu & Kurnaz (2020), a wearable microstrip antenna was designed to detect tumors in organs such as the brain, liver, and kidney. The antenna designed using the CST program is in a wearable form that does not pose a risk to health and allows monitoring of patients with high cancer risk.

Hancılar (2022), to provide early intervention to the patient, the circuit design integrated into the wearable system through a sensor that detects chest/diaphragm movements was tested on 20 volunteers and their breathing rates were calculated. Although the designed velostat sensor is a successful sensor in respiratory monitoring, it poses a problem in daily use when the body is in motion. In this study, the test was performed when the body was motionless.

Çelenk (2022), three different textile antenna designs were designed to design wearable textile antennas by adapting them with metamaterials. In the first study, a planar and curved meta-material TEDK (Base Integrated Waveguide) leakage wave antenna, which operates in a wider frequency band than other antennas in the literature, was designed. The antenna produced in the second study can be used for military applications. It has been found that the proposed antenna is suitable in terms of cost and mass production. When the literature was examined, it was seen that the cavity supported TEDK textile antenna had the highest efficiency compared to similar antennas. In the third study, a fully textile, washable meta-surface antenna was designed. It has been observed that metasurface structures are important in terms of antenna gain and efficiency.

Vallozzi et al. (2009), GPS modules have been integrated to be applied to fire- and water-resistant textile materials and rescue personnel. The effects of the textile layer on the return loss were investigated and it was seen that the antenna was able to fulfill its function.

Roh et al. (2010), by conducting research on the use of textile-based antennas in designs, it has been determined that linear and planar antennas are more suitable for wearable textile products. It has been observed that broadband textile antennas can be used over long distances in military, space, protective and medical fields.

Morrison et al. (2014), An electrocardiographic circuit (flexible electrodes, battery and antenna) is integrated into the textile material. Heart values were monitored and encrypted with a flexible antenna.

Blecha et al. (2014), information was transmitted on the textile surface with printed antennas. This easy-to-use, low-cost system is designed for firefighter clothing and this product provides significant advantages in terms of electronic textiles.

Top et al. (2017), in the modeling developed for the detection of heart diseases using microstrip antenna, 2.45GHz was chosen for the design. By using 42.5 dielectric and 1.40 conductivity values, electromagnetic field simulation values were obtained in cases where there was no vascular occlusion and in cases where there was vascular occlusion, and the differences were examined. When the results were examined, it was seen that the data were different in case of occlusion in the cardiovascular system and that electromagnetic signal data could be used in heart-related disorders.

Patel et al. (2010), a system has been developed to monitor the changes in the motor system of parkinson patients from home. The data obtained from ECG, respiratory and motion sensors are sent to the hospital's central network via a web-based mobile phone and reached the relevant doctor's computer.

Guinovart et al. (2014), the pH level of the wounds is monitored and constantly controlled through wearable electrochemical sensors placed in the bandage.

Varadan (2011), a person's heart health and neurological diseases can be examined by attaching it to clothes called e-Nanoflex. After wearing this garment, the person's health status is transferred to smartphones. This system can perform all the operations that the ECG device does

Frost (2018), developed by Leaf Healthcare for decubitus ulcer patients, the user interface observes the patient's position in order to observe the patient's activities, and allows the nurse and doctor to be informed in which direction the patient should move and when the patient does not move correctly.

Health Care Originals (2024), developed by Health Care Originals, the system that can be worn under clothes provides flexible, comfortable, patch-type smart asthma management and transmits information about the individual's breathing pattern, cough monitoring, body temperature, heart rate and asthma-related conditions.

Muluparti et al. (2024), used denim, cotton, leather, jeans and silk textile materials as a rectangular patch substrate in the antenna design for use in biomedical and healthcare services. Designed to operate at 2.47 GHz, this antenna was found to be promising for healthcare applications, with denim operating smoothly in the intended frequency range and being the most suitable textile material to be used. In the simulation performed using the CST tool, the simulated reflection coefficient was at -28dB, exceeding the -10dB reference point, showing strong performance and robust impedance matching. It provided a solid foundation for the development of textile-based antennas in healthcare applications and demonstrated the applicability of such designs.

Musa et al. (2024), included a SEN11547 pulse sensor and an LM35 temperature sensor to detect heart rate and body temperature data in a health monitoring system for Internet of Things (IoT) applications. Two dual-band microstrip patch antennas, each measuring 41 x 44 mm^2, were built on the Rogers Duroid RO3003™ substrate. One of these antennas is equipped with a PIN diode. An inverted U-shaped slot was added to the existing patch to provide dual-band operation at 2.4 GHz and to create a 5.8 GHz frequency band. The active antenna can switch between a single 5.8 GHz band and a dual-band configuration of 2.4 GHz and 5.8 GHz. Ten samples were collected at 1-minute intervals for 10 minutes from ten participants, ages 18 to 40. To validate the results, measurements were compared with a commercially available Laird Connectivity 2.4 GHz/5.8 GHz dipole antenna. Heart rates ranged from 85 BPM to 92 BPM for the active antennas and from 84 to 90 BPM for the reference antenna, indicating good agreement. Similarly, the body temperature varies between 29 and 37°C for active antennas and between 30 and 36°C for the reference antenna. In conclusion, this study highlights the effective integration of the proposed dual-band active antenna into an IoT-based health monitoring system.

Soni et al. (2024), carried out an antenna design for tumor detection at 2.45 GHz and the antenna was designed on a flexible substrate polyimide with a dielectric constant of 3.5. A tumorous human tissue model is designed for tumor detection and different simulation analyses are performed on the human tissue model. The size of the presented antenna is $43.45\times35\times0.75mm^3$. The reflection coefficient (|S11|), 3D radiation patterns, directionality gain and SAR parameters were analyzed. It was found that this antenna is very suitable for on-body biomedical applications at 2.45 GHz frequency, especially in tumor detection.

Casula et al. (2024), a novel on-body/epidermal antenna is designed on a miniaturized AMC structure. For this purpose, a conventional unit cell is suitably wrapped and a home-made high-permittivity and low-loss thin and flexible silicon doped dielectric substrate is used. The antenna operates at RFID UHF frequencies of approximately 900 MHz and its overall footprint is limited to only 0.03 λ02 (41.4 × 82.8 mm). The proposed device is highly reliable, platform tolerant, and implemented on a very thin, flexible, and biocompatible substrate. There are sufficient holes in both the AMC substrate and the ground plane to allow skin perspiration. These features enable the designed structure to be effectively used as an epidermal antenna, allowing “on-skin” sampling of most typical health parameters such as body temperature, skin impedance, and electrophysiological potentials.

The technology of wearable antennas is advancing rapidly with advances in both material science and textile, computer and electronic engineering. This enables the new generation of wearable devices to become more functional.

7. Conclusion

With the developments in the textile sector, products that meet different needs are produced and offered to the market. Smart electronic textiles, which are among technical textiles; Textile products become functional because of the integration of textile, electronics, medicine, computer and design fields. These products, which are of great importance especially for the healthcare sector, are integrated into the clothing and enable the patient to be monitored without wasting time, thus increasing the patient's quality of life. Wearable antennas, which can be easily integrated into clothing, can be integrated into the fabric to detect diseases, reduce pain, transfer patient data, and monitor basic health information without compromising the elegance of the clothing. Through the optimization algorithm, the wearable textile product that will form the base material of the microstrip antenna can be determined and the most suitable textile product can be used. Wearable antennas used in electronic textiles are very important for the healthcare sector; It seems to provide great convenience for patients, their relatives and healthcare professionals. These products with functional features are expected to have a great future promise in the textile industry.

References

Acar, G. (2019). Graphene textile smart clothing for wearable cardiac monitoring (Doctoral dissertation).

Ahmed, M.I., Ahmed, M.F., Shaalan, A.-E.H., 2018. Novel electro-textile patch antenna on jeans substrate for wearable applications. Progress In Electromagnetics Research, 83: 255–265.

Albairaqdar, O. H. M. (2018). Giyilebilir uygulamalar için eşit yama alanına (EYA) sahip tekstil dielektrik malzeme tabanlı mikroşerit antenlerin 2.4, 3 ve 5.8 GHz frekanslarındaki performansları.

Anderson, K. S. A. M., & Seyam, A. M. (2004). The road to true wearable electronics. Textiles Magazine, 31(1), 17-22.

Arı, S. (2016). Görme engelliler için yüksek frekanslı ses dalgaları kullanılarak giyilebilir mesafe ölçer tasarımı (Master's thesis, Sakarya Universitesi (Turkey)).

Arman Kuzubaşoğlu, B. Development of textile based temperature sensor for wearable electronics. Istanbul Technical University, Graduate School, 2021.

Arslan, K. (2009). Teknik tekstiller genel ve güncel bilgiler. Müsiad Araştırma Raporları, 52.

Ataş, İ. (2019). Yüksek kazançlı mikroşerit antenlerin hfss ile modellenmesi ve tasarımı.

Balanis, C. A. (2015). Antenna theory: analysis and design. John wiley & sons.

Balanis, C.A. (2005). Antenna theory: analysis and design, Wiley-Interscience, 3rd edition.

Bedeloğlu, A. Ç., Sünter, N., & Bozkurt, Y. (2010). Elektriksel Olarak İletken Tekstilyapilari, Üretim Yöntemleri Ve Kullanim Alanlari. 2010 (Cilt: 17), 79.

Bilgin, N. F. (2016). Giyilebilir teknolojiler tabanlı mobil hasta takip sistemi tasarımı ve gerçekleştirilmesi (Master's thesis, Sakarya Üniversitesi).

Blecha, T., Linhart, R., & Reboun, J. (2014, September). Screen printed antennas on textile substrate. In Proceedings of the 5th Electronics System-integration Technology Conference (ESTC) (pp. 1-4). IEEE.

Borg, R. (2015). The biggest thing in wearable tech! Urban Wearables.

Canbaz, B., & Yalçın, N. Giyilebilir Teknolojilerin Eğitim Alanında Kullanımları. 14. International Computer and Instructional Tehcnologies Syposium ICITS-2021, Rize, Türkiye, 26-28 Ekim 2021, ss.49-55.

Casula, G. A., Lestini, F., Chietera, F. P., Muntoni, G., Occhiuzzi, C., Catarinucci, L., ... & Marrocco, G. (2024). Design of On-Body Epidermal Antenna on AMC Substrate for UHF RFID in Healthcare. IEEE Transactions on Antennas and Propagation.

Çelenk, E. (2022). “Textile metamaterials and application / Ph.D Thesis”.

De Rossi, D., Della Santa, A., & Mazzoldi, A. (1999). Dressware: wearable hardware. Materials Science and Engineering: C, 7(1), 31-35.

Derneryd, A. (1978). A theoretical investigation of the rectangular microstrip antenna element. IEEE Transactions on Antennas and Propagation, 26(4), 532-535.

Dhupkariya, S., Singh, V.K., Shukla, A., 2015. A review of textile materials for wearable antenna, Journal of Microwave Engineering & Technologies, 1(3): 7–14.

Elrashidi, A., Elleithy, K., Bajwa, H., 2011. Resonance Frequency, Gain, Efficiency and Quality Factor of a Microstrip Printed Antenna as a Function of Curvature for TM01 mode Using Different Substrates. Journal of Wireless Networking and Communications, 1: 1–8.

Ercan, K. (2018). Giyilebilir Elektronik Uygulamalarına Yönelik Yüksek Sıcaklıklara Dayanıklı Veri İletim Kalitesi Yüksek E-Tekstil Yapılarının Geliştirilmesi.

Erdem, D. (2017). Diz osteoartrit tedavisinde kullanılmak üzere akıllı bir dizlik tasarımı (Master's thesis, Dokuz Eylul Universitesi (Turkey)).

Erol, A. D., & Çetiner, S. (2017). Giyilebilir Elektronik/Akıllı Tekstiller ve Uygulamaları. Kahramanmaraş Sütçü İmam Üniversitesi Mühendislik Bilimleri Dergisi, 20(1), 1-20.

Farad, M. M. M., & Dixit, M. (2014). Bandwidth Enhancement of Microstrip patch Antenna Using Suspended Techniques for Wireless Applications. International Journal of Engineering Research, 3(5).

Frost, S. (2018). North American Pressure Ulcer Prevention New Product Innovation Award.

George, G., Nagarjun, R., Thiripurasundari, D., Poonkuzhali, R., Alex, Z. C., 2013. Design of meander line wearable antenna, 2013 IEEE Conference on Information & Communication Technologies, 11-12 April 2013, Thuckalay, Tamil Nadu, India, IEEE, 1190-1193 pp.

Giddens, H., Paul, D. L., Hilton, G. S., & McGeehan, J. P. (2012, March). Influence of body proximity on the efficiency of a wearable textile patch antenna. In 2012 6th European Conference on Antennas and Propagation (EUCAP) (pp. 1353-1357). IEEE.

Gökdemir, M. (2022). A compact low sar value circularly polarized wearable antenna design for 5G applications/5G uygulamaları için kompakt düşük sar değerli dairesel polarize giyilebilir anten tasarımı. İstanbul Teknik Üniversitesi, Lisansüstü Eğitim Enstitüsü, Elektrik ve Elektronik Mühendisliği, Yüksek Lisans Tezi, 89s., İstanbul.

Guinovart, T., Valdés-Ramírez, G., Windmiller, J. R., Andrade, F. J., & Wang, J. (2014). Bandage-based wearable potentiometric sensor for monitoring wound pH. Electroanalysis, 26(6), 1345-1353.

Guinovart, T., Valdés-Ramírez, G., Windmiller, J. R., Andrade, F. J., & Wang, J. (2014). Bandage-based wearable potentiometric sensor for monitoring wound pH. Electroanalysis, 26(6), 1345-1353.

Güler, M. (2007). Giyilebilir algılayıcılar ile yaşamsal verilerin ölçülmesi iletilmesi ve görüntülenmesi.

Gupta, B., Sankaralingam, S., & Dhar, S. (2010, August). Development of wearable and implantable antennas in the last decade: A review. In 2010 10th Mediterranean Microwave Symposium (pp. 251-267). IEEE.

Gürcüm, B. H., Gök, M. O., & Babaoğlu, S. (2015). Hayati Verileri Tespit Eden Elektronik Tekstiller. Tekstil Trend.

Hancılar, Ü. (2022). “Nefes Takip Sistemi Tasarımı ve Giyilebilir Sisteme Entegresi”.

Health Care Originals. (2024). (Access: https://healthcareoriginals.com/personal/, Date: 06.01.2024).

Hertleer, C., Rogier, H., Vallozzi, L., Van Langenhove, L., 2009. A textile antenna for off-body communication integrated into protective clothing for firefighters. IEEE Transactions on Antennas and Propagation, 57 (4): 919–925.

Hertleer, C., Van Laere, A., Rogier, H., & Van Langenhove, L. (2010). Influence of relative humidity on textile antenna performance. Textile Research Journal, 80(2), 177-183.

Horrocks, A. Richard, and Subhash C. Anand, eds. Handbook of technical textiles. Elsevier, 2000.

Interactive Projects. (2018). Ying Gao. http://yinggao.ca/interactifs/nowhere-nowhere/

Ivšić, B., 2013. Textile Antennas for Body-Centric Communication Systems, University of Zagreb. Faculty of Electrical Engineering and Computing. Department of Wireless Communications, Doctoral Thesis, Zagreb, 241 pp.

Kılıç, H. Ö. (2017). Giyilebilir teknoloji ürünleri pazarı ve kullanım alanları. Aksaray Üniversitesi İktisadi ve İdari Bilimler Fakültesi Dergisi, 9(4), 99-112.

Kim, B., Koncar, V., Devaux, E., Dufour, C., & Viallier, P. (2004). Electrical and morphological properties of PP and PET conductive polymer fibers. Synthetic Metals, 146(2), 167-174.

Kumar, S., & Krupinski, E. (Eds.). (2008). Teleradiology. Springer Science & Business Media.

Kurt, M., & Kaya, M. (2022). Meme Kanseri Teshişinde Mikrodalga Yama Antenlerinin Kullanılması. Avrupa Bilim ve Teknoloji Dergisi, (36), 293-297.

Lin, X., Seet, B. C., & Joseph, F., 2018. Wearable humidity sensing antenna for BAN applications over 5G networks. 2018 IEEE

19th Wireless and Microwave Technology Conference (WAMICON), 9-10 April 2018, Sand Key, FL, USA, IEEE, 1–4 pp.

Loss, C. (2017). Study of the Electromagnetic Properties of Textiles: Development of

Matthews, J. C. G., & Pettitt, G. (2009, March). Development of flexible, wearable antennas. In 2009 3rd European Conference on Antennas and Propagation (pp. 273-277). IEEE.

McCann, J., & Bryson, D. (Eds.). (2022). Smart clothes and wearable technology. Woodhead Publishing.

Morrison, T., Silver, J., & Otis, B. (2014, June). A single-chip encrypted wireless 12-lead ECG smart shirt for continuous health monitoring. In 2014 symposium on VLSI circuits digest of technical papers (pp. 1-2). IEEE.

Mulaparti, M. K., Kumari, U. R., & Sandeep, D. R. (2024, February). A Wearable Textile Antenna for Health Care Applications. In 2024 IEEE Wireless Antenna and Microwave Symposium (WAMS) (pp. 1-5). IEEE.

Musa, U., Shah, S. M., Majid, H. A., Mahadi, I. A., Rahim, M. K. A., Yahya, M. S., & Abidin, Z. Z. (2024). Design and Implementation of Active Antennas for IoT-Based Healthcare Monitoring System. IEEE Access.

Mutlu, M., & Kurnaz, Ç. (2020). Mikrodalga Görüntüleme Sistemleri için Mikroşerit Anten Tasarımı. Avrupa Bilim ve Teknoloji Dergisi, 129-137.

Norooz, L., Mauriello, M. L., Jorgensen, A., Mcnally, B., & Froehlich, J. E. (2015). BodyVis: A New Approach to Body Learning Through Wearable Sensing and Visualization Wearables; interactive body learning; physiological sensing. 1025–1034.

Olewitz, C. (2016). Intel's morphing Adrenaline Dress will transform when it detects elevated stress levels. Digital Trends. (Access: https://www.digitaltrends.com/cool-tech/intel-adrenaline-dress-morphs-based-on-stress/#/1, Date: 02.01.2024).

Ouyang, Y., & Chappell, W. J. (2008). High frequency properties of electro-textiles for wearable antenna applications. IEEE Transactions on Antennas and Propagation, 56(2), 381-389.

Paracha, K.N., Rahim, S.K.A., Soh, P.J., Khalily, M., 2019. Wearable Antennas: A Review of Materials, Structures, and Innovative Features for Autonomous Communication and Sensing. IEEE Access, 7: 56694–56712.

Patel, M., Kuchhal, P., Lal, K., & Mishra, R. (2017). Design and analysis of microstrip patch antenna array using different substrates for X-band applications. International Journal of Applied Engineering Research, 12(19), 8577-8581.

Patel, S., Chen, B. R., Buckley, T., Rednic, R., McClure, D., Tarsy, D., ... & Bonato, P. (2010, August). Home monitoring of patients with Parkinson's disease via wearable technology and a web-based application. In 2010 annual international conference of the IEEE engineering in medicine and biology (pp. 4411-4414). IEEE.

Pormfret, S. J., Adams, P. N., Comfort, N. P., & Monkman, A. P. (1999). Advances in processing routes for conductive polyaniline fibers. Synth Met, 101, 724-725.

Quantum 3D Expedition. (2024). (Access: https://quantum3d.com/, Date: 10.01.2024).

Roh, J. S., Chi, Y. S., & Kang, T. J. (2010). Wearable textile antennas. International Journal of Fashion Design, Technology and Education, 3(3), 135-153.

Salvado, R., Loss, C., Gonçalves, R., Pinho, P., 2012. Textile materials for the design of wearable antennas: a survey. Sensors, 12 (11): 15841–15857.

Schwarz, A., Van Langenhove, L., Guermonprez, P., & Deguillemont, D. (2010). A roadmap on smart textiles. Textile progress, 42(2), 99-180.

Shikder, K., & Arifin, F., 2015. Design and evaluation of a UWB wearable textile antenna for body area network. 2015 2nd International Conference on Electrical Information and Communication Technologies (EICT), 10-12 Dec. 2015, Khulna, Bangladesh, IEEE, pp: 326–330 pp.

Singh, N., Singh, A.K., Singh, V.K., 2015. Design and performance of wearable ultrawide band textile antenna for medical applications. Microwave and Optical Technology Letters, 57 (7): 1553–1557.

Smith, W. C. (1988). Metallized fabrics—techniques and applications. Journal of coated fabrics, 17(4), 242-253.

Soni, G. K., Yadav, D., & Kumar, A. (2024, March). Enhancing Healthcare: Flexible and Wearable Antenna Design for Tumor Detection. In 2024 International Conference on Distributed Computing and Optimization Techniques (ICDCOT) (pp. 1-5). IEEE.

Stoppa, M., & Chiolerio, A. (2014). Wearable electronics and smart textiles: A critical review. sensors, 14(7), 11957-11992.

Textile Antennas for Energy Harvesting Universidade da Beira Interior Doctoral Thesis, Covilhã Portugal, .145 pp

Thomas, P. C., & David, W. M. (1992, January). Augmented reality: An application of heads-up display technology to manual manufacturing processes. In Hawaii international conference on system sciences (Vol. 2, pp. 659-669). ACM SIGCHI Bulletin.

Tommy Hilfiger Solar Clothing. (2014). (Access: http://www.pvilion.com/solar-clothing, Date: 04.01.2024).

Top, R., Gültekin, S. S., & Uzer, D. (2017, May). Modeling congestion of vessel on rectangular microstrip antenna and evaluating electromagnetic signals. In 2017 25th Signal Processing and Communications Applications Conference (SIU) (pp. 1-4). IEEE.

Topcuoğlu Güray, N. (2018). Elektronik tekstil tabanlı romatoid artrit rehabilitasyon eldiveni geliştirilmesi (Master's thesis, Fen Bilimleri Enstitüsü).

Tsolis, A., Whittow, W.G., Alexandridis, A.A., Vardaxoglou, J.C., 2014. Embroidery and related manufacturing techniques for wearable antennas: challenges and opportunities. Electronics, 3 (2): 314–338.

Uyanık, H. (2021). Kalp damar tıkanıklığının tespiti için giyilebilir mikroşerit anten tasarımı (Master's thesis, Konya Teknik Üniversitesi).

Vallozzi, L., Hertleer, C., & Rogier, H. (2016). Latest developments in the field of textile antennas. 599–626, Smart textiles and their applications, (Eds:V. Koncar) Woodhead Publishing.

Vallozzi, L., Vandendriessche, W., Rogier, H., Hertleer, C., & Scarpello, M. (2009). Design of a protective garment GPS antenna. Microwave and optical technology letters, 51(6), 1504-1508.

Varadan, V. K. (2011). An EKG in your Underwear. Mechanical Engineering, 133(10), 34-37.

Virtual Worldlets Network. (2024). (Access: https://www.virtualworldinternet.com/, Date: 06.01.2024).

Wang, H., Fang, D. G., & Wang, X. L. (2008, December). Mutual coupling reduction between two microstrip patch antennas by using the parasitic elements. In 2008 Asia-Pacific Microwave Conference (pp. 1-4). IEEE.

Wang, J. C., Lim, E. G., Leach, M., Wang, Z., Man, K. L., & Huang, Y. (2016, March). Conformal wearable antennas for WBAN applications. In Proceedings of the international multiconference of engineers and computer scientists (Vol. 2, pp. 651-654).

Wang, Z., Zhang, L., Psychoudakis, D., & Volakis, J. L. (2012, March). Flexible textile antennas for body-worn communication. In 2012 IEEE International Workshop on Antenna Technology (iWAT) (pp. 205-208). IEEE.

Wang, J. C., Lim, E. G., Leach, M., Wang, Z., Man, K. L., & Huang, Y. (2016, March). Conformal wearable antennas for WBAN applications. In Proceedings of the international multiconference of engineers and computer scientists (Vol. 2, pp. 651-654).

Xue, P., & Tao, X. M. (2005). Morphological and electromechanical studies of fibers coated with electrically conductive polymer. Journal of applied polymer science, 98(4), 1844-1854.

Yousefalturk, H., & Cansız, M. (2022). RF enerji hasatlama için 915 MHz taşıyıcı frekansında mikroşerit anten tasarımı ve uygulaması. Dicle Üniversitesi Mühendislik Fakültesi Mühendislik Dergisi, 13(3), 531-539.

CHAPTER VII

Design and Analysis of Titanium Nitride-Based Metalens for Efficient Light Focusing at 1550 nm Fiber Optical Wavelength

Yunus UÇAR [1]
Ekin ASLAN [2]
Erdem ASLAN [3]

Introduction

Metasurfaces have introduced groundbreaking innovations in the control of electromagnetic waves, becoming a prominent research field in photonic and electronic device technologies (Meinzer, Barnes, & Hooper, 2014; Yu & Capasso, 2014). These structures offer unique advantages in applications such as wavefront shaping, beam steering, focusing, and holography (Aieta et al., 2012;

[1] PhD Student, Kayseri University, Department of Electrical and Electronics Engineering, yunusucar@kayseri.edu.tr, Orcıd: 0000-0002-9174-4202
[2] Assoc. Prof, Kayseri University, Department of Electrical and Electronics Engineering, ekinaslan@kayseri.edu.tr, Orcıd: 0000-0003-0933-7796
[3] Assoc. Prof, Erciyes University, Department of Electrical and Electronics Engineering, aslanerdem@erciyes.edu.tr, Orcıd: 0000-0001-6829-9000

Khorasaninejad & Capasso, 2017). The core principle of metasurfaces lies in their ability to manipulate properties of light—such as amplitude, phase, polarization, and orientation—through nano-scale structures organized on their surfaces (Kildishev, Boltasseva, & Shalaev, 2013; Lin, Fan, Hasman, & Brongersma, 2014; Schulz et al., 2024). This enables the development of thin and lightweight structures that can replace traditional optical components (Chen, Taylor, & Yu, 2016).

The potential of these metasurfaces, particularly in telecommunications wavelengths, allows for the miniaturization of optical devices and the development of high-precision applications (Aieta, Genevet, Khorasaninejad, Capasso, & Devlin, 2017). Due to their unique structural characteristics, metasurfaces provide extensive application opportunities—from wavefront manipulation and control to holographic imaging systems and quantum information processing (Kuznetsov, Miroshnichenko, Brongersma, Kivshar, & Luk'yanchuk, 2016; Yu et al., 2011).

The choice of materials in the design of metasurfaces significantly affects their performance. Traditionally, noble metals such as gold and silver have been the materials of choice due to their plasmonic properties (Boltasseva & Atwater, 2011). However, the high optical losses and low thermal stability of these metals impose significant limitations, especially in high-temperature applications and broadband optical devices (Naik, Shalaev, & Boltasseva, 2013; Schuller et al., 2010). As a result, the exploration of alternative plasmonic materials has gained great importance (Boltasseva & Shalaev, 2015; Mahajan, Dhonde, Sahu, Ghosh, & Shirage, 2024).

Titanium nitride (TiN) has recently emerged as a promising alternative plasmonic material. TiN stands out with its high melting point, chemical stability, and low optical losses (Mahajan et al., 2024; Naik et al., 2013). Moreover, its compatibility with CMOS fabrication processes facilitates its integration into photonic circuits

(Schuller et al., 2010). The optical properties of TiN demonstrate plasmonic behavior similar to gold and silver in the visible and near-infrared spectral ranges (Boltasseva & Shalaev, 2015; Kuznetsov et al., 2016). These characteristics make TiN-based metasurfaces promising candidates for the development of broadband and highly efficient optical devices (Chen et al., 2016).

The ability of metasurfaces to manipulate wavefronts enhances optical system performance and unlocks new application opportunities (Huang et al., 2016; Yu & Capasso, 2014). Specifically, the control of light phase plays a critical role in achieving functionalities such as focusing and beam steering (Khorasaninejad & Capasso, 2017; Meinzer et al., 2014). The design of meta-cells capable of providing a continuous phase shift between 0 and 2π enables the development of high-precision optical components (Aieta et al., 2012; Lin et al., 2014). Such metasurfaces offer significant advantages in designing compact and integrated optical systems (Kildishev et al., 2013).

The impact of metasurfaces on optical systems has become more pronounced due to their advantages over traditional optical components. In particular, their ability to control the phase, amplitude, and polarization of light positions metasurfaces as pivotal elements in next-generation optical devices (Meinzer et al., 2014; Yu & Capasso, 2014). These advantages, combined with their compact size, lightweight structure, and ease of fabrication, make them ideal for applications ranging from optical communications and holography to imaging and information processing (Aieta et al., 2012; Kildishev et al., 2013).

The high precision of metasurfaces in wavefront manipulation significantly enhances optical system performance. Controlling the wavefront phase is essential for a variety of applications, including light focusing, beam steering, and digital information transfer (Khorasaninejad & Capasso, 2017). For example, in holographic systems, metasurfaces provide thinner and lighter structures than conventional optical elements, resulting in more precise imaging performance (Huang et al., 2016).

In this study, a focusing metasurface designed to operate at a 1550 nm wavelength using TiN as the primary material is developed to achieve focusing functionality. The metasurface design consists of 20 meta-cells capable of providing a continuous phase shift from 0 to 2π. Numerical analyses are conducted using the Finite-Difference Time-Domain (FDTD) method, confirming that the metasurface's focusing performance is within acceptable levels (A. Taflove, S. C. Hagness, 2005). The results demonstrate that TiN-based metasurfaces enable low-loss, high-efficiency, and thermally stable focusing applications.

TiN-based metasurfaces are not limited to focusing applications but also offer innovative solutions in various fields, including optical communication, quantum information processing, laser steering, and imaging (Li, Zhang, & Zentgraf, 2017; Mahajan et al., 2024; Yu & Capasso, 2014). In particular, the precision of wavefront manipulation achieved by metasurfaces provides a powerful tool for quantum optics and information processing systems (Kuznetsov et al., 2016). The developed metasurface combines miniaturization with performance enhancement in optical systems, offering revolutionary contributions to future academic, military, and commercial applications (Aieta et al., 2017; Boltasseva & Shalaev, 2015).

Method

In this study, an alternative plasmonic metasurface capable of focusing light at a specific focal distance f is designed and analyzed. To achieve the intended functionality of the metasurface, a phase profile is initially formulated to enable the focusing effect, followed by the optimization of the meta-cell geometries and the evaluation of their electromagnetic properties through numerical simulations.

The phase profile on the metasurface is determined to produce a spherical wavefront, and it is mathematically modeled using the following equation (Aieta et al., 2012):

$$\varphi_L(x, y) = \frac{2\pi}{\lambda}\overline{P_L S_L} = \frac{2\pi}{\lambda}\left(\sqrt{(x^2 + y^2) + f^2} - f\right) \tag{1}$$

In this equation, φ_L represents the phase shift at the P_L (x, y) position, f=5000 µm is the focal distance of the metasurface, and λ=1550 nm is the operating wavelength. The wavelength is selected due to its low-loss and low-dispersion characteristics, making it ideal for fiber-optic communication systems. The overall size of the metasurface is designed to be 400 µm × 400 µm, composed of meta-cells with a periodicity of 2.5 µm. The phase profile is modeled to span a range of [0–2π] and is designed according to the arrangement shown in Figure 2.

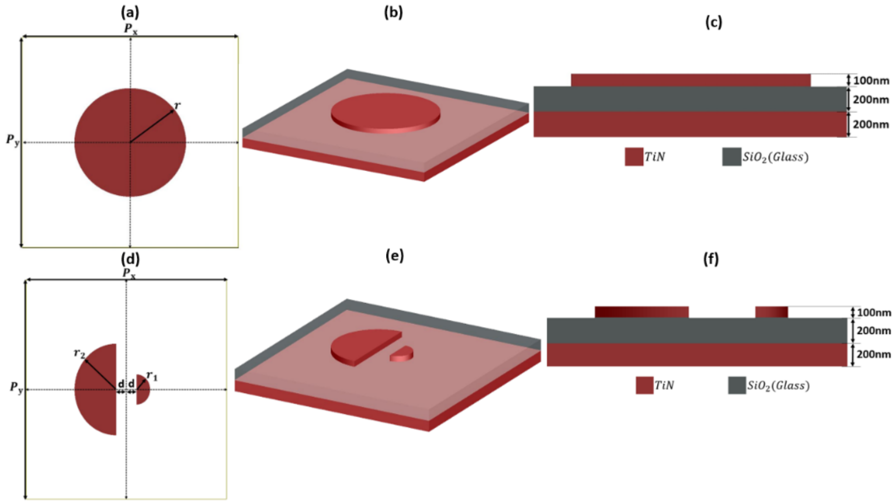

***Figure 1**: The Designed Circle Couple Shape Antenna Structure: (a) top view, (b) perspective (c) side views, The Designed Semi-Circle Couple Shape Antenna Structure: (d) top view, (e) perspective (f) side views.*

The meta-cell structures are optimized to modulate the wavefront with a specific phase shift. The meta-cell structures consist of three layers: the TiN reflective layer, which provides high reflection resonance; the SiO_2 dielectric spacer layer, which functions as an optical insulator and alignment medium; and the TiN nanoantenna layer, which enables electromagnetic phase control. The nanoantenna layer includes two distinct types of geometries as shown in Figure 1 that enable electromagnetic phase control. The dimensions and shapes of these geometries are optimized to cover the phase range of [0–2π]. Moreover, the geometric parameters of the nanoantennas are adjusted to correspond to specific phase values.

The optical properties and phase responses of the designed metasurface are analyzed using the FDTD method. In the simulations, the electromagnetic behavior of periodic meta-cells on the xy-plane, illuminated by a normally incident x-linearly polarized plane wave in the xz-plane, is investigated. The reflection phase and amplitude responses of each meta-cell type are meticulously analyzed. The antenna arrangements required for the first phase ring, with dimensions of 35 μm × 125 μm, are examined within the simulation area and optimized based on the results.

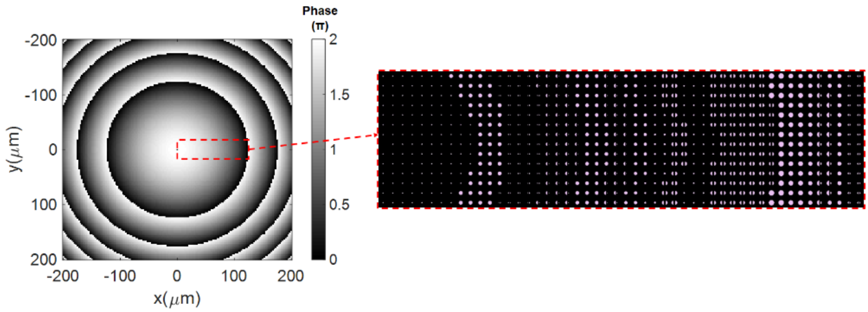

Figure 2: *Required Phase Map for a 5 mm Focal Length Metalens on a 400 μm x 400 μm Surface Composed of Unit Cells with a 2.5 μm Periodicity, with an Inset Representation of the Antenna Arrangement in a 35 μm x 125 μm Area for the First 0-2π Phase Ring.*

The data obtained from the simulations are evaluated in terms of reflection phase, focusing precision, and reflection efficiency. The three-layer structure of the metasurface, composed of TiN and SiO_2 materials, demonstrated high reflection resonances and is optimized for efficient light focusing. This design provides an effective solution with high optical performance.

Results

The phase and reflection responses of each meta-cell were thoroughly analyzed to investigate the influence of geometric parameters on the electromagnetic behavior of the metasurface. This analysis focused on evaluating the performance of meta-cells with antenna layers designed with varying geometrical configurations.

As presented in Table 1, the phase and reflection responses demonstrate that a smooth phase transition is achieved across the 0–2π range, meeting the desired phase shift criteria. Furthermore, it is noted that the reflection coefficient remained relatively stable during the phase transition process, indicating reliable performance.

Table 1: *Geometric Parameters of Designed Antenna Array.*

Antenna	Antenna Type	Geometric Parameters							
		Reflection	Phase (π)	r (nm)	d (nm)	r_1 (nm)	r_2 (nm)	Px (nm)	Py (nm)
1	Semi-Circle Couple	0,8889	0,0349	-	150	250	250	2500	2500
2	Semi-Circle Couple	0,8784	0,1216	-	125	250	250	2500	2500
3	Circle	0,7895	0,2286	525	-	-	-	2500	2500
4	Semi-Circle Couple	0,8105	0,3206	-	150	300	650	2500	2500
5	Circle	0,8353	0,4243	550	-	-	-	2500	2500
6	Circle	0,7947	0,5488	625	-	-	-	2500	2500
7	Circle	0,8667	0,6423	700	-	-	-	2500	2500
8	Semi-Circle Couple	0,7247	0,7495	-	225	450	450	2500	2500
9	Semi-Circle Couple	0,7151	0,8250	-	225	475	475	2500	2500
10	Semi-Circle Couple	0,7343	0,9305	-	250	475	475	2500	2500
11	Circle	0,8502	1,2087	200	-	-	-	2500	2500
12	Semi-Circle Couple	0,7316	1,2588	-	250	500	500	2500	2500
13	Circle	0,8673	1,3815	250	-	-	-	2500	2500
14	Circle	0,8393	1,4305	425	-	-	-	2500	2500
15	Semi-Circle Couple	0,8400	1,5233	-	125	150	475	2500	2500
16	Circle	0,7685	1,6290	475	-	-	-	2500	2500
17	Semi-Circle Couple	0,8363	1,7272	-	175	175	500	2500	2500
18	Semi-Circle Couple	0,9013	1,8342	-	150	175	175	2500	2500
19	Circle	0,7401	1,9018	500	-	-	-	2500	2500
20	Circle	0,8775	1,9624	100	-	-	-	2500	2500

Graphical representations of the phase and reflection responses as a function of antenna configurations are given Figure 3 (a) and (b), respectively. These results show that the phase shift is achieved with high precision, while the reflection coefficient stabilizes around an average value of 0.8. This consistency highlights the effectiveness of the meta-cells in controlling phase transitions while maintaining an optimized reflection efficiency.

Overall, the findings underline the importance of carefully tailoring geometric parameters to achieve targeted electromagnetic properties in meta-cell design. The smooth phase modulation and consistent reflection performance contribute significantly to the metasurface's optical functionality, making it a highly effective solution for the intended applications.

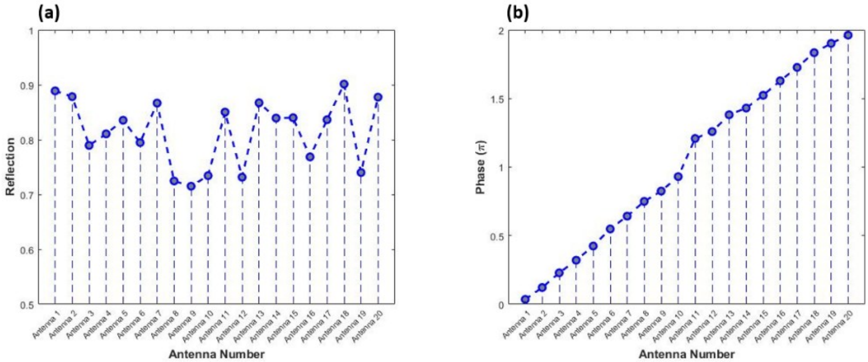

Figure 3: *(a) Antenna Reflection Values and (b) Antenna Phase Values.*

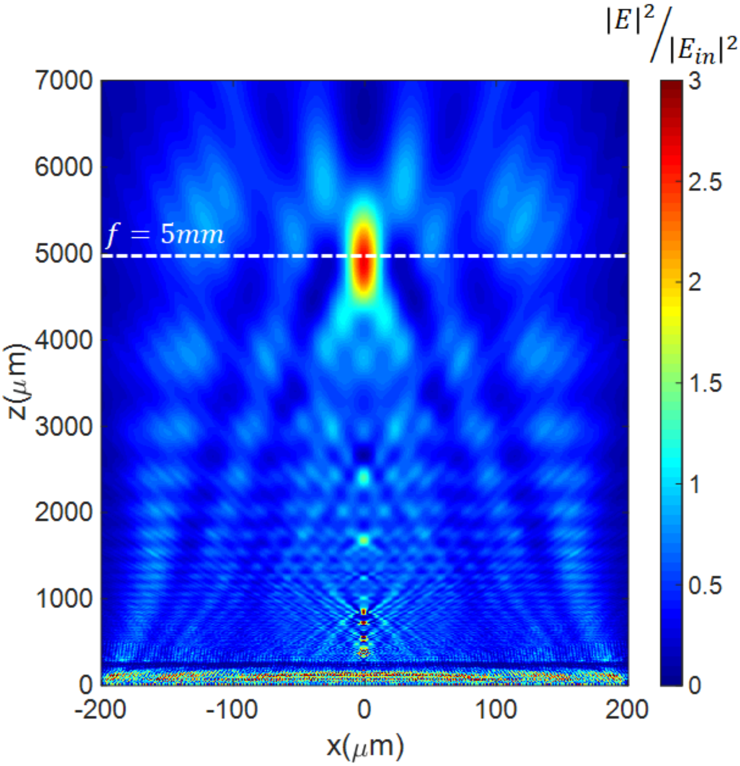

Figure 4: *Normalized Light Intensity Distribution in the xz-plane with Respect to the Source.*

In Figure 4, it is demonstrated that focusing can be achieved at the planned focal distance of 5 mm, as determined by the focusing equation in Equation 1 through numerical analyses. The figure also reveals the presence of multiple focal points. These additional focal points may result from scattering caused by factors such as phase map tolerances of the unit cells, fill factor variations due to periodicity, and similar effects. Achieving a sufficiently distant focal length of 5 mm aligns with the objectives of this study, and the normalized light intensity at the focal point indicates a high focusing efficiency.

Conclusion

This study presents the design and analysis of a metalens operating at a wavelength of 1550 nm, utilizing TiN as the nanoantenna material. TiN demonstrates considerable promise for advanced photonic applications, with its low-loss properties, high thermal stability, and alternative plasmonic character. The design incorporates 20 meta-cells, each capable of inducing a continuous phase shift from 0 to 2π, facilitating precise control over the wavefront and enabling effective light focusing at a focal length of 5 mm.

The rigorous numerical analysis using FDTD method validates the high precision of phase control and reflection efficiency achieved by the metalens. The results indicate that the phase shift is finely tuned, and the reflection coefficient maintains an optimized value of around 0.8, confirming the stability and efficiency of the metasurface design. Additionally, the observation of multiple focal points, likely due to scattering effects and phase map tolerances, suggests areas for further optimization. However, the achieved focusing efficiency at the intended focal length meets the design objectives, marking a significant step forward in the development of metasurface-based optical components, in terms of the use of alternative plasmonic materials.

In conclusion, this work highlights the potential of TiN-based metalenses for future optical systems, where precise manipulation of light can be achieved in a highly integrated, scalable manner. Further refinements in the design and fabrication processes, especially concerning scattering and fill factor variations, will enhance the performance and applicability of these devices in advanced photonic technologies.

Acknowledgement

This study was supported by Scientific and Technological Research Council of Turkey (TUBITAK) under the Grant Number 121E518. The authors thank to TUBITAK for their supports

References

A. Taflove, S. C. Hagness, M. P.-M. (2005). Computational electromagnetics: the finite-difference time-domain method. In *The Electrical Engineering Handbook* (pp. 629–670).

Aieta, F., Genevet, P., Kats, M. A., Yu, N., Blanchard, R., Gaburro, Z., & Capasso, F. (2012). Aberration-free ultrathin flat lenses and axicons at telecom wavelengths based on plasmonic metasurfaces. *Nano Letters*, *12*(9), 4932–4936. https://doi.org/10.1021/NL302516V

Aieta, F., Genevet, P., Khorasaninejad, M., Capasso, F., & Devlin, R. (2017). Recent advances in planar optics: from plasmonic to dielectric metasurfaces. *Optica, Vol. 4, Issue 1, Pp. 139-152*, *4*(1), 139–152. https://doi.org/10.1364/OPTICA.4.000139

Boltasseva, A., & Atwater, H. A. (2011). Low-Loss Plasmonic Metamaterials. *Science*, *331*(6015), 290–291. https://doi.org/10.1126/SCIENCE.1198258

Boltasseva, A., & Shalaev, V. M. (2015). All that glitters need not be gold. *Science*, *347*(6228), 1308–1310. https://doi.org/10.1126/SCIENCE.AAA8282

Chen, H. T., Taylor, A. J., & Yu, N. (2016). A review of metasurfaces: physics and applications. *Reports on Progress in Physics*, *79*(7), 076401. https://doi.org/10.1088/0034-4885/79/7/076401

Huang, Y. W., Lee, H. W. H., Sokhoyan, R., Pala, R. A., Thyagarajan, K., Han, S., … Atwater, H. A. (2016). Gate-Tunable

Conducting Oxide Metasurfaces. *Nano Letters*, *16*(9), 5319–5325. https://doi.org/10.1021/ACS.NANOLETT.6B00555

Khorasaninejad, M., & Capasso, F. (2017). Metalenses: Versatile multifunctional photonic components. *Science*, *358*(6367). https://doi.org/10.1126/SCIENCE.AAM8100

Kildishev, A. V., Boltasseva, A., & Shalaev, V. M. (2013). Planar Photonics with Metasurfaces. *Science*, *339*(6125), 12320091–12320096. https://doi.org/10.1126/SCIENCE.1232009

Kuznetsov, A. I., Miroshnichenko, A. E., Brongersma, M. L., Kivshar, Y. S., & Luk'yanchuk, B. (2016). Optically resonant dielectric nanostructures. *Science*, *354*(6314). https://doi.org/10.1126/SCIENCE.AAG2472

Li, G., Zhang, S., & Zentgraf, T. (2017). Nonlinear photonic metasurfaces. *Nature Reviews Materials 2017 2:5*, *2*(5), 1–14. https://doi.org/10.1038/natrevmats.2017.10

Lin, D., Fan, P., Hasman, E., & Brongersma, M. L. (2014). Dielectric gradient metasurface optical elements. *Science*, *345*(6194), 298–302. https://doi.org/10.1126/SCIENCE.1253213

Mahajan, U., Dhonde, M., Sahu, K., Ghosh, P., & Shirage, P. M. (2024). Titanium nitride (TiN) as a promising alternative to plasmonic metals: a comprehensive review of synthesis and applications. *Materials Advances*, *5*(3), 846–895. https://doi.org/10.1039/D3MA00965C

Meinzer, N., Barnes, W. L., & Hooper, I. R. (2014). Plasmonic meta-atoms and metasurfaces. *Nature Photonics 2014 8:12*, *8*(12), 889–898. https://doi.org/10.1038/nphoton.2014.247

Naik, G. V., Shalaev, V. M., & Boltasseva, A. (2013). Alternative Plasmonic Materials: Beyond Gold and Silver. *Advanced Materials*, *25*(24), 3264–3294. https://doi.org/10.1002/ADMA.201205076

Schuller, J. A., Barnard, E. S., Cai, W., Jun, Y. C., White, J. S., & Brongersma, M. L. (2010). Plasmonics for extreme light concentration and manipulation. *Nature Materials 2010 9:3*, *9*(3), 193–204. https://doi.org/10.1038/nmat2630

Schulz, S. A., Oulton, R. F., Kenney, M., Alù, A., Staude, I., Bashiri, A., … Fernandez-Corbaton, I. (2024). Roadmap on photonic metasurfaces. *Applied Physics Letters*, *124*(26). https://doi.org/10.1063/5.0204694/3300335

Yu, N., & Capasso, F. (2014). Flat optics with designer metasurfaces. *Nature Materials 2014 13:2*, *13*(2), 139–150. https://doi.org/10.1038/nmat3839

Yu, N., Genevet, P., Kats, M. A., Aieta, F., Tetienne, J. P., Capasso, F., & Gaburro, Z. (2011). Light propagation with phase discontinuities: Generalized laws of reflection and refraction. *Science*, *334*(6054), 333–337. https://doi.org/10.1126/SCIENCE.1210713

CHAPTER VIII

Innovative Approach in Technical Education: Hands-on Learning with KNX Building Automation Experiment Set for Students

Zühal POLAT[1]
Kübra Nur AKPINAR[2]

1. Introduction

With their remarkable comfort and energy-saving advantages, smart home systems have swiftly established themselves as a mainstay of contemporary living. By seamlessly integrating several sensors and gadgets, these systems optimize energy use, accommodate personal preferences, and improve home security. Smart homes reduce energy waste and improve quality of life by

[1] Asst.Prof., Marmara University, Vocational School of Technical Sciences, Department of Electricity and Energy, Istanbul /Türkiye, Orcid: 0000-0002-0234-4662, zuhalpolat@marmara.edu.tr
[2] Dr., Marmara University, Vocational School of Technical Sciences, Department of Electricity and Energy, Istanbul /Türkiye, Orcid: 0000-0003-4579-4070, knur@marmara.edu.tr

automating energy-intensive duties like lighting, heating, and cooling(Majeed et al., 2020). Internationally accepted standards that guarantee these systems' dependability, adaptability, and scalability are at their foundation. The KNX protocol is a well-known name in this industry and has established the benchmark for innovation in smart home technologies.

The KNX protocol is an internationally recognized open standard for home and building automation, enabling seamless communication among diverse systems such as lighting, HVAC, security, and energy management. As an ISO/IEC 14543-3-certified protocol, KNX guarantees interoperability across devices from different manufacturers, making it a cornerstone in smart home and industrial automation. It is a key enabler in integrating various building automation technologies into a cohesive, reliable system (Malhi & Apopei, 2022). At its core, KNX utilizes a decentralized communication architecture, ensuring that devices operate autonomously while maintaining network-wide synchronization. This decentralized nature enhances system reliability, allowing for robust control even if individual devices fail. Moreover, KNX supports various communication media—including twisted pair, RF, powerline, and IP—enabling broad adaptability to different building types and infrastructures (Kraus et al., 2020). Integrating Internet of Things (IoT) technologies has elevated KNX's relevance by facilitating real-time monitoring, control, and automation. IoT integration enables dynamic interactions between sensors, actuators, and cloud services, providing users with enhanced control through mobile applications and web platforms(Swathika, 2022) (Srividya, 2021). For instance, in smart homes, KNX systems allow users to remotely adjust lighting, monitor energy consumption, or manage HVAC systems to optimize comfort and efficiency(Conceic'ão et al., 2022). Additionally, KNX plays a vital role in advancing energy efficiency and sustainability. It supports the integration of renewable energy sources, such as solar panels, and enables predictive maintenance through IoT-based analytics. This capability is critical for reducing energy consumption and promoting environmentally friendly practices in smart buildings(Satheeskanth et al., 2022). By bridging traditional building control systems with cutting-edge IoT technologies, the KNX protocol offers a scalable and future-proof solution for building automation. Its robust architecture, compliance with international standards, and integration with IoT platforms underscore its pivotal role in modern smart environments(Hakiri et al., 2020).

In summary, the KNX protocol is more than just a communication standard; it is a transformative technology that underpins the evolution of smart buildings and cities. Its emphasis on interoperability, real-time control, and sustainability positions it as an indispensable tool for modern building automation.

The extensive application of KNX necessitates the development of educational activities and practical opportunities, particularly for students pursuing technical education. This enables future professionals to comprehend the dynamics of building automation systems, enhancing their ability to utilize or improve such systems efficiently.

This study has developed an experimental setup to allow associate degree students to design and implement applications related to smart home systems. The developed setup introduces KNX simulator modules and the KNX software programming tool, ETS. Learning the KNX system offers numerous advantages for students. First, as KNX is an internationally recognized standard, it allows students to work with globally acknowledged technology. This increases their employability prospects after graduation and will enable them to participate in international projects.

2. KNX Protocol and Integration with Other Technologies:

Integration of KNX Protocol with Other Technologies The KNX protocol is widely recognized for its flexibility and capacity to integrate diverse technologies, enabling seamless communication between various building automation systems. Its role in enhancing system efficiency and improving user experience is significant, as it bridges traditional automation methods with modern digital frameworks. One fascinating application of KNX is the simulation of KNXnet/IP telegrams. Using tools like MATLAB/Simulink, researchers have been able to simulate and analyze the behavior of building automation systems. For instance, (López-Aguilar et al., 2018) demonstrated how tools like Wireshark can monitor and optimize data packets. This approach has gained popularity for its ability to simplify troubleshooting and improve overall system reliability (Bergmann et al., 2012). (Kraus et al., 2020) developed a prototype gateway that allows seamless communication between KNX and service-oriented device connectivity (SDC) to address the growing need for interoperability. By enabling integration with protocols like BACnet, Modbus, and Zigbee, this innovation provides a unified framework for diverse automation technologies. In another breakthrough, (Bovet & Hennebert, 2013) introduced a

Web of Things gateway for KNX networks, integrating web-based technologies through HTTP and RESTful APIs. This advancement enables KNX systems to operate within modern IoT ecosystems, enabling remote monitoring and controlling of devices. Research by (Guinard et al., 2009) supports this, showing how RESTful APIs simplify IoT integration and enhance system scalability. On the hardware side, (Han et al., 2010) developed KNX device nodes and binary output actuators using a Bus Interface Module (BIM). This design reduces device complexity, improves efficiency, and lowers costs. Similarly, (Pérez-Lombard et al., 2008) explored innovations to improve energy efficiency and make KNX systems easier to deploy in residential and commercial settings. User-friendly interfaces are another key focus area for KNX systems. (Wünsche, 2019) highlighted the importance of creating intuitive interfaces for managing devices like lighting and HVAC systems. These interfaces make automation accessible to a broader audience, even those without technical expertise. Similarly, (Page et al., 2016) emphasized how graphical user interfaces (GUIs) improve user interactions with building systems, simplifying the operation of complex technologies. (Neugschwandtner et al., 2007) developed a method to map KNX data to oBIX (Open Building Information Exchange) entities to bridge the gap between traditional automation systems and modern IT frameworks. This approach facilitates better communication between KNX systems and IT-based solutions. (Kastner et al., 2005) also emphasized the importance of aligning building automation protocols with IT systems for enhanced functionality and interoperability. Energy management is one of KNX’s most impactful contributions. By incorporating energy meters, motion sensors, and automated timers, KNX systems help reduce energy consumption and promote sustainability(Pérez-Lombard et al., 2008). Finally, integrating KNX with IoT technologies has significantly expanded its capabilities. (Bergmann et al., 2012) demonstrated how lightweight IoT protocols like MQTT and CoAP can enhance KNX's scalability and responsiveness. This hybrid architecture enables advanced IoT applications, such as predictive maintenance and AI-powered automation, further solidifying KNX's position as a cornerstone of modern building automation. Through these advancements, KNX proves its adaptability, facilitating the creation of more innovative, sustainable, and user-friendly building automation systems. Its ability to integrate with emerging technologies positions it as a vital tool for addressing the challenges of modern clever building design.

3. KNX ETS 5: Infrastructure for Modern Building Automation

Based on the globally accepted KNX protocol, KNX ETS 5 software is essential for contemporary automation and intelligent building systems. The benefits of the KNX protocol, such as flexibility, system integration, and energy efficiency, have made it a global standard. With its flexible and intuitive interface, KNX ETS 5 makes it easier to develop, configure, and manage building automation projects. In residential and commercial buildings, it efficiently executes a range of automation scenarios, such as lighting, climate control, energy management, and security systems.

KNX ETS 5 is essential to education because it gives engineering students practical experience. Students can apply their theoretical knowledge to real-world situations using KNX-based automation simulators created for educational reasons. These simulators aim to provide aspiring engineers with a thorough understanding of intelligent control systems, system integration, and energy efficiency. KNX ETS 5 promotes increased comprehension and adoption of building automation systems among wider audiences by aiding in the teaching process(Toylan & Cetin, 2019).

Technically speaking, current research focuses on improving KNX technology's performance and adaptability. Improvements in KNX device nodes and bus interface modules are especially significant. These modules increase system dependability and efficiency by optimizing communication between KNX devices and central control units. By focusing on efficiency and sustainability, these advancements guarantee quicker and more energy-efficient system operations, helping to shape the future of building automation systems(Han et al., 2010).

4. Home Automation Project Simulation with KNX

Control Panel for Automation of Smart Buildings Based on KNXA KNX-based control panel intended for intelligent building automation is shown in Figure 1. Lighting, switching, heating-cooling, and other vital systems can be controlled with the help of the popular KNX protocol, which allows various devices to communicate with each other without any problem (Association). How does the experiment set equipment work:

- *Power Source (640mA PSU),* the KNX system's power supply is its central component, providing all linked devices with the energy they require. It guarantees that the entire KNX bus line remains powered and functional with its 640 mA capacity.

- *IP Router,* remote access is made possible by the IP router, which links the KNX bus to an IP network. This allows you to keep an eye on and manage KNX.

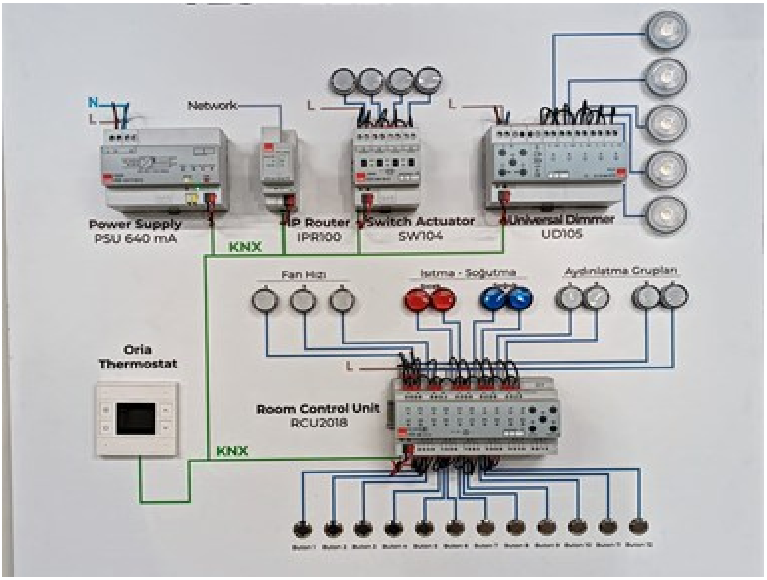

Figure 1. Experiment set panel (test elements)

This allows you to use an IP-based system or the internet to monitor and manage KNX devices from any location.

- *Switch Actuator*, the connected circuits' on/off switching is managed by this relay-based device. Its four channels offer dependable and effective control over lighting, outlets, and other loads (Jung, 2019).
- *Universal Dimmer, w*hether the lights are halogen, LED, or another dimmable variety, the dimmer controls their brightness. Its six channels allow for exact control of illumination levels, saving energy and producing the ideal atmosphere.
- *Oria Thermostat, b*y controlling the heating and cooling systems, the thermostat controls the ambient temperature. It

guarantees effective and comfortable climate control and is fully integrated with the KNX network.

- *Room Control Unit, t*his multipurpose device serves as the brains behind a room's automation requirements. It manages a number of tasks, including climate management, curtain and lighting control, and more. The proper actions are performed once commands from buttons or other inputs are analyzed.
- *Climate Control and Fan Speed, i*n order to ensure ideal airflow and temperature regulation, these sections concentrate especially on controlling fan speeds and climate systems, such as VRF or fan-coil units.
- *Lamps and Buttons,* users can interact with the system by turning lights or devices on and off using the buttons at the bottom of the panel. As indicators, the bulbs at the top display the state of several outputs.

The KNX bus line allows seamless communication between all devices. Remote access and control are made possible by the IP router, which connects the system to the IP network. Lighting functions like turning lights on and off and dimming them are handled by devices like the Switch Actuator and Universal Dimmer. Comfort and climate are expertly controlled thanks to the Oria Thermostat and Room Control Unit. The system offers the highest level of flexibility and usability by allowing users to engage with it remotely or through physical buttons.

By improving energy efficiency, enabling remote control, and providing a smooth, user-friendly experience, this KNX-based technology intelligently automates buildings. This system offers comfort, control, and convenience whether it is controlling the lighting, controlling the temperature, or automating everyday chores.

4.1 Building Structure:

Figure 2 shows the ETS5 software interface for configuring and managing a KNX-based building automation project. This interface provides information about the building structure and group address organization used for communication between devices.

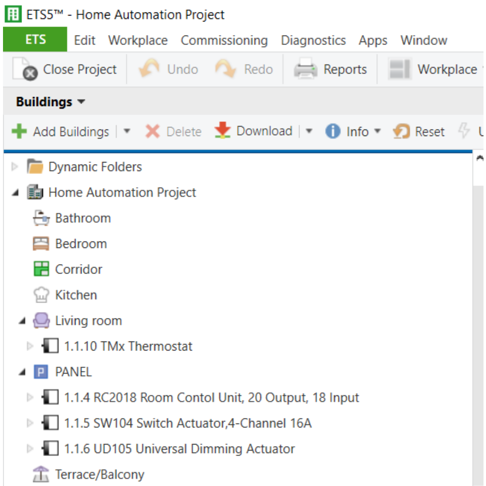

Figure 2. ETS5 software interface

This section represents the hierarchical organization of the building and its devices. The main project structure organizes different zones (rooms) and their devices. The zones are defined as the bathrooms, bedrooms, corridors, kitchen, living rooms, and terrace/balcony.

The TMx Thermostat in the living room controls the temperature. The panel contains three devices: the Room Control Unit, the Switch Actuator, and the Universal Dimming Actuator. The Room Control Unit is a central controller with 20 outputs and 18 inputs to manage multiple systems. The Switch Actuator is a 4-

channel actuator that switches high-current circuits (16A). The Universal Dimming Actuator controls dimmable lights in the living room.

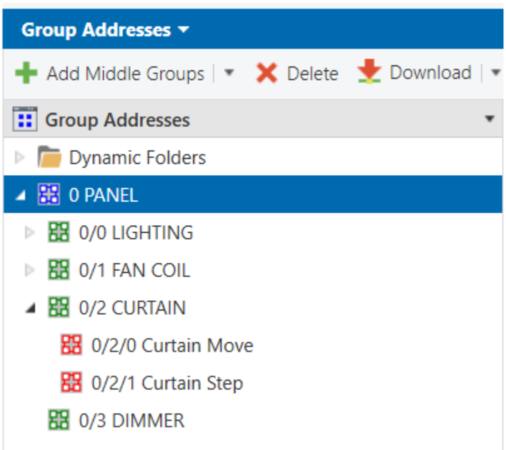

Figure 3. ETS5 group addresses the interface

4.2 Group Addresses:

This section organizes KNX group communication logic. Group Addresses represent logical links that allow devices to interact.

Figure 3 shows the ETS5 (Engineering Tool Software) interface in the Group Addresses section of a KNX building automation project. In KNX systems, Group Addresses represent the logical connections facilitating communication between devices.

In KNX systems, Group Addresses are organized using a three-level structure, Main Group, Middle Group, and Sub Group, to categorize control operations systematically. This structure ensures that communication is organized in an orderly and systematic manner. Here, Panel (Main Group: 0) is used for general system-wide control addresses. Lighting (Middle Group: 0/0) is the address used for lighting control. Lights connected via KNX are controlled via this group address. Fan Coil (Middle Group: 0/1) is reserved for controlling HVAC fan coil units. This group is used to manage temperature and climate systems. Blind (Middle Group: 0/2) is the group address reserved for curtain and blind control. Blind Movement (Subgroups) sends commands to open and close blinds. Blind Step (Subgroups) set blinds to a specific position or step. The dimmer (Middle Group 0/3) is the address for lighting dimmer control. Dimmer actuators allow adjustment of the brightness levels of lights.

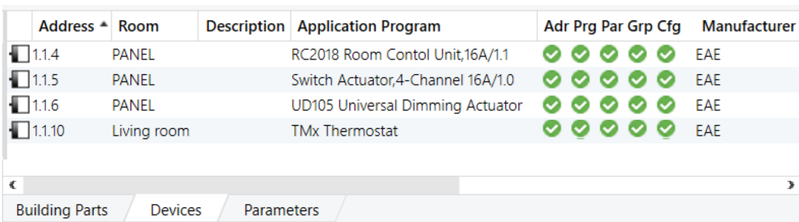

Address	Room	Description	Application Program	Adr	Prg	Par	Grp	Cfg	Manufacturer
1.1.4	PANEL		RC2018 Room Contol Unit,16A/1.1	✓	✓	✓	✓	✓	EAE
1.1.5	PANEL		Switch Actuator,4-Channel 16A/1.0	✓	✓	✓	✓	✓	EAE
1.1.6	PANEL		UD105 Universal Dimming Actuator	✓	✓	✓	✓	✓	EAE
1.1.10	Living room		TMx Thermostat	✓	✓	✓	✓	✓	EAE

Figure 4. Addressing, programming, and configuring the interface of devices in ETS

Figure 4 provides detailed information about the devices' addressing, programming and configuration status in the ETS. Each device in the KNX system has a unique physical address. For example, 1.1.4 and 1.1.5 represent the physical addresses of the devices in the network. The room column indicates the physical location or room where the devices are installed. For example, "PANEL" and "Living Room" are mentioned. This helps you understand which zone or area the devices belong to.

The description column describes the functions of the devices. For example, the RC2018 Room Control Unit is a room control unit that is usually used to manage lighting and blinds.

The application program column shows the name and version information of the programs running on the devices. For example: RC2018 Room Control Unit, 16A/1.1, is the program version of the room control unit. Switch Actuator, 4 Channel 16A/1,0, is the program version of the 4-channel switching actuator. The programs are used to configure the functionality of the devices.

Adr, Prg, Par, Grp, Cfg (Addressing, Programming, Parameterization, Group Objects, Configuration), these columns indicate whether certain operations in the KNX system have been completed:

- ✓ Adr: Physical address assignment completed.
- ✓ Prg: Programming completed.
- ✓ Par: Parameter configuration completed.
- ✓ Grp: Group objects set.
- ✓ Cfg: Device fully configured.

The Manufacturer column indicates the manufacturer of the device. EAE manufactures all devices in the image. Building parts, devices, and parameter tabs are used to manage and configure devices in the ETS software.

Conclusion

Learning the KNX system provides students with valuable skills in building automation and innovative building technologies. These skills offer technical knowledge and prepare students to design and implement creative solutions that increase energy efficiency, comfort, and safety.

Students develop a solid foundation in electrical and electronic principles that enable them to install and connect KNX devices. They learn how components such as sensors, actuators, and power supplies work and gain knowledge on how to install power and signal lines properly. Since KNX is an open standard for building automation, it provides its users with expertise in data communication, device addressing (physical and group addresses), and system topology.

Understanding KNX certification standards also helps them understand the importance of compliance. With these experimental setups, students become proficient in using ETS (Engineering Tool Software), an essential tool for programming KNX devices. They learn to handle tasks such as addressing devices, creating group objects, and configuring parameters. Over time, they gain confidence in installing, testing, and commissioning complete KNX systems. Additionally, users discover how to integrate various systems such as lighting, HVAC (heating, ventilation, air conditioning), security systems, energy management, and blinds control.

This allows them to design intuitive user interfaces and create imaginative scenarios such as automatic lighting for energy saving. Students develop the ability to plan KNX network topologies, whether linear, star, tree, or hybrid. They learn to scale and adapt KNX devices for large projects, analyze system needs, and select the proper devices for specific applications. Troubleshooting becomes second nature as they learn to diagnose and fix problems in KNX systems. They practice debugging, data analysis, and reviewing system logs to optimize performance. They also gain skills in system updates and maintenance. Students understand how KNX systems contribute to energy efficiency. They gain the ability to design solutions that reduce energy consumption, such as implementing timers, motion sensors, or energy meters for intelligent control. Users also learn how to integrate KNX systems with IoT devices and ensure seamless communication between different systems. Their ability to work with APIs and protocol converters (for example, for KNX-Zigbee integration) prepares them for modern, connected building environments.

Learning KNX is about acquiring technical knowledge and designing intelligent systems that make buildings more efficient, comfortable, and future-proof. Whether working on a small residential project or an extensive commercial integration, a skilled KNX expert plays a vital role in shaping the buildings of tomorrow.

References

Association, K. *KNX: The worldwide standard for home and building control*. KNX Association. https://www.knx.org

Bergmann, O., Hillmann, K., & Gerdes, S. (2012). A CoAP-gateway for smart homes. https://doi.org/10.1109/ICCNC.2012.6167461

Bovet, G., & Hennebert, J. (2013). *A Web-of-Things Gateway for KNX Networks*.

Conceic'ão, A. A. d., Ambrosio, L. P., Leme, T. R., Rosa, A. C. S., Ramborger, F. F., Aquino, G. P., & Boas, E. C. V. (2022, 22-22 Jan. 2022). Internet of Things Environment Automation: A Smart Lab Practical Approach. 2022 2nd International Conference on Information Technology and Education (ICIT&E),

Guinard, D., Trifa, V., Pham, T., & Liechti, O. (2009). Towards physical mashups in the web of things. 2009 Sixth International Conference on Networked Sensing Systems (INSS),

Hakiri, A., Sellami, B., Yahia, S. B., & Berthou, P. (2020, 28-30 Oct. 2020). A SDN-based IoT Architecture Framework for Efficient Energy Management in Smart Buildings. 2020 Global Information Infrastructure and Networking Symposium (GIIS),

Han, N., Wu, Y.-H., & Tang, Y. (2010). Research of KNX device node and development based on the bus interface module. Proceedings of the 29th Chinese Control Conference,

Kastner, W., Neugschwandtner, G., Soucek, S., & Newman, H. M. (2005). Communication systems for building automation and control. *Proceedings of the IEEE*, *93*(6), 1178-1203.

Kraus, N., Viertel, M., & Burgert, O. (2020, 10-12 June 2020). Control of KNX devices over IEEE 11073 service-oriented device connectivity. 2020 IEEE Conference on Industrial Cyberphysical Systems (ICPS),

López-Aguilar, A., Navarro Tuch, S., Bustamante-Bello, R., Curiel-Ramirez, L., & Izquierdo-Reyes, J. (2018). *Interpretation and Emulation for Telegrams of the KNX Standard on MATLAB Simulink*. https://doi.org/10.1109/ICMEAE.2018.00031

Majeed, R., Abdullah, N. A., Ashraf, I., Zikria, Y. B., Mushtaq, M. F., & Umer, M. (2020). An intelligent, secure, and smart home automation system. *Scientific Programming*, *2020*(1), 4579291.

Malhi, A., & Apopei, V. (2022, 30 May-3 June 2022). Open Platform for Rapid Prototyping of Smart Environment Applications. 2022 International Wireless Communications and Mobile Computing (IWCMC),

Neugschwandtner, M., Neugschwandtner, G., & Kastner, W. (2007). *Web services in building automation: Mapping KNX to oBIX* (Vol. 1). https://doi.org/10.1109/INDIN.2007.4384736

Page, A., Hijazi, S., Askan, D., Kantarci, B., & Soyata, T. (2016). Research directions in cloud-based decision support systems for health monitoring using Internet-of-Things driven data acquisition. *Int. J. Serv. Comput*, *4*(4), 18-34.

Pérez-Lombard, L., Ortiz, J., & Pout, C. (2008). A review on buildings energy consumption information. *Energy and*

Buildings,*40*(3),394-398. https://doi.org/https://doi.org/10.1016/j.enbuild.2007.03.007

Satheeskanth, N., Marasinghe, S., Rathnayaka, R., Kunaraj, A., & Joy Mathavan, J. (2022). IoT-based integrated smart home automation system. Ubiquitous Intelligent Systems: Proceedings of ICUIS 2021,

Swathika, O. V. G., Karthikeyan, K., & Padmanaban, S. (Eds.). . (2022). *Smart Buildings Digitalization: Case Studies on Data Centers and Automation* CRC Press. https://doi.org/https://doi.org/10.1201/9781003240853

Toylan, M. Y., & Cetin, E. (2019). Design and application of a KNX-based home automation simulator for smart home system education. *Computer Applications in Engineering Education*, *27*(6),1465-1484. https://doi.org/https://doi.org/10.1002/cae.22162

Wünsche, I. (2019). *The Routledge Companion to Expressionism in a Transnational Context*. Routledge.

BÖLÜM IX

Hydroelectric Power Plants and Their Environmental Impacts

Erşan Ömer YÜZER[1]

Introduction

Hydraulic energy is an energy source that is indirectly generated by solar radiation. Water in seas, lakes, or rivers evaporates under the influence of solar energy, and the resulting water vapor is carried by winds to mountain slopes, where it returns to the surface as rain or snow, feeding rivers. This process makes hydraulic energy a continuously renewable energy source. To utilize the kinetic and potential energy of water, hydroelectric power plants (HPPs) have been and continue to be established. In this way, a highly durable and cost-effective energy source is made available for electricity generation (Olgun, 2009; OMU, 2024).

HPPs can be built not only on rivers, lakes, or streams but also on canals or systems designed to utilize water

[1] Lect. Dr., Hakkari University, Çölemerik Vocational High School, Çölemerik Vocational High School, Hakkari/Turkey, Orcid: 0000-0002-9089-1358, ersanomeryuzer@hakkari.edu.tr

accumulated from tidal movements. The energy produced in these plants generally depends on the water head and flow rate. Based on these factors, HPPs can be classified as follows: (Serencam, 2007; Oral, Behçet & Aykut, 2017; Süme & Fırat, 2020).

- According to Storage Structures:
  - ✓ Reservoir HPPs (with storage)
  - ✓ Run-of-river HPPs (regulator type)
- According to Head (Water Drop):
  - ✓ Low-head HPPs (H < 10 m)
  - ✓ Medium-head HPPs (H = 10–50 m)
  - ✓ High-head HPPs (H > 50 m)
- According to Installed Capacity:
  - ✓ Very small (micro) capacity (<100 kW)
  - ✓ Small (mini) capacity (100–1,000 kW)
  - ✓ Medium capacity (1,000–10,000 kW)
  - ✓ Large capacity (>10,000 kW)
- According to Contribution to the National Grid Load:
  - ✓ Base-load HPPs
  - ✓ Peak-load HPPs
  - ✓ Combined base-load and peak-load HPPs
- According to Dam Structure Type:
  - ✓ Gravity concrete dam HPPs
  - ✓ Arch concrete dam HPPs
  - ✓ Rock-fill dam HPPs
  - ✓ Earth-fill dam HPPs
- According to Power Plant Location:
  - ✓ Above-ground HPPs
  - ✓ Underground HPPs
  - ✓ Semi-buried or submerged HPPs

HPPs offer numerous advantages compared to other types of power plants. However, their primary advantage is that, unlike thermal power plants, they do not cause any air pollution

(Kasirga, 2024). Some of their other advantages can be summarized as follows (Koçak, 2011; ETKB, 2024):

- There are no fuel costs,
- Losses are negligible, even when the plant is on standby,
- Efficiency does not decrease over time,
- Requires a minimal workforce,
- The unit cost of energy is very low,
- Adapts quickly to load changes.
- Maintenance costs are low, and the structure is simple and robust.

HPPs provide benefits beyond electricity generation. These can be outlined as follows:

- Irrigation of large areas,
- Prevention of floods,
- Fisheries,
- Utilization of water transport (e.g., cargo and passenger transportation),
- Water sports,
- Afforestation,
- Promotion of tourism.

Water stored or naturally accumulated in a specific location possesses potential energy. When this potential energy is released from a height at a certain velocity, it is converted into kinetic energy, which then transforms into mechanical energy (shaft energy) through the turbine blades. The shaft energy is subsequently converted into electrical energy using generators, making it usable (Özbay & Gençoğlu, 2009; Dinçer & ark., 2017; Erkin, 2019). The process and sequence of energy conversion in HPPs are illustrated in Figure 1.

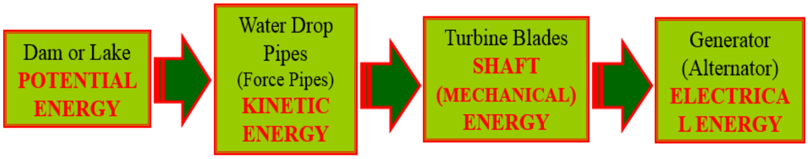

Figure 1. *Energy Conversion in HPPs*

The Relationship of HPPs with the Natural Environment

With the increasing applications of HPPs, the environmental damage they cause has become a topic of debate, particularly in the last 30 years. Projects that have significant economic and socio-cultural consequences have begun to face resistance in implementation areas. The issue, initially framed as an environmental problem concerning the protection of nature and the image of women, has later evolved into a political issue due to its position in the media (Çevik, 2022).

The development of water resources for various purposes, including energy production, involves several stages and a long process. This includes planning and project studies to determine the technical specifications and potential socioeconomic impacts, followed by the implementation phase. Additionally, it encompasses the ongoing operational and management activities throughout the project's economic lifespan, with a focus on monitoring the interaction between the natural environment and these activities (DPT, 2001).

In order to avoid experiencing another energy crisis like the one faced in Turkey in 1973, which was partially mitigated in the short term through domestic resources, it is essential to implement long-term energy policies. A critical factor that must not be overlooked while formulating these policies is the "environment." In our country, which has yet to reach the development threshold of 2000 kWh/year per capita, fossil fuel-based electricity generation facilities have caused, and continue to cause, environmental pollution in many regions. Considering this context, it is highly beneficial to prioritize the construction of hydraulic energy plants in the coming years, in line with a protection-use balance, with the goal of both avoiding future energy crises and minimizing damage to the natural environment (DPT, 2001).

Energy production facilities (thermal, hydro, nuclear) have varying degrees of impact on the environment. Similarly, the measures required to mitigate potential negative effects vary based on the technology, size, and cost involved. It would be beneficial to reassess energy production facilities from the perspective of their environmental impacts. (Şahin, 1989).

The most significant environmental risk associated with nuclear energy is the waste disposal issue, which has only been partially addressed and remains costly, even if technically resolved. The lifespan of nuclear power plants is also limited to just a few decades (Tüylüoğlu & Türkan, 2023). On the other hand, hydraulic energy does not increase carbon dioxide levels or contribute to acid rain. When making a comparison in this context, it can be said that the risks associated with hydraulic energy are much lower. Furthermore, considering the importance of energy in the national economy and the protection of the environment, hydroelectric power plants are among the most environmentally friendly energy production facilities (Şenpınar & Gençoğlu, 2006).

The highest efficiency in electricity generation from hydroelectric energy depends on the suitability of geographical conditions. In Turkey, the variation in rainfall across regions and seasons, as well as the differences in riverbed slopes, prevent equal utilization of water power across all regions. Hydroelectric energy, which has the highest potential among renewable energy sources, is directly influenced by factors such as terrain and elevation. For example, in the Marmara Region, the limited flow rate and gentle slopes of rivers restrict the hydroelectric potential, whereas the more favorable terrain in the Eastern Anatolia Region makes it highly suitable for hydroelectric power plants (Kenet, 2020).

The environmental impacts caused by a reservoir-type hydroelectric power plant (HPP) can now be more easily prevented and mitigated compared to the past. Furthermore, other energy sources that serve as alternatives to hydroelectric energy are significantly riskier from an environmental perspective (for example, atmospheric carbon dioxide accumulation and acid rain caused by the burning of fossil fuels). However, the major environmental advantage of hydraulic energy is that it is a highly efficient, environmentally friendly renewable energy source (Şavkar, 2024). If constructed and managed properly, a hydraulic project can produce continuous electricity through the hydrological cycle. Additionally, renewable hydroelectric energy has very low operational costs compared to thermal power plants that rely on imported fuel, due to the absence of fuel costs (Bülbül & Çokluk, 2017; Oral, Behçet & Aykut, 2017). Moreover, hydroelectric power plants are cleaner than some coal-fired thermal projects that release tons of sulfur and dust into the atmosphere every day.

In general, hydroelectric energy is considered to be the energy technology with the least environmental risk among known energy technologies. Although, from a social risk perspective, it has been concluded that "hydroelectric energy is more dangerous than nuclear energy" due to past hydroelectric power plant accidents, it should not be overlooked that the effects of hydraulic energy accidents are localized and do not pass from generation to generation. Additionally, as a result of the impact of hydroelectric power plant reservoirs on the hydrological cycle, positive changes in climate and vegetation are generally observed. However, even though hydroelectric energy is considered a renewable resource, its production facilities do have impacts on both the natural and socio-economic environment, with the scale of these effects varying from project to project (Özdemir, Özaydın & Yılmaz, 2023). Surface water resources are not only used for hydroelectric energy production, but they also constitute the water potential that is essential for a country's survival, and future generations have a right to it. To ensure that the planning, management, and use of water resources for various purposes is conducted in a healthy and rational manner, it is essential to predict the impacts of projects that could disrupt the natural structure in a timely manner and to take necessary precautions. In this context, it is beneficial to examine the environmental impacts of hydroelectric facilities.

Hydroelectric power plants have microclimatic, hydrological, biological, socioeconomic, and cultural impacts. Climatic effects stem from the larger surface area of a reservoir-type HPP compared to the river, which leads to increased evaporation. As a result, the humidity in the air rises, atmospheric mass movements change, and temperature, precipitation, and wind patterns differ. This situation creates dynamic and cascading effects on natural environmental parameters. The local natural vegetation (forests, meadows, endemic species), economic species (agricultural crops), and certain species of aquatic-terrestrial animals may change, adapt, or new species may emerge (Onüçyıldız, Büyükkaracığan & Erkmen, 2013). Additionally, changes in water temperature and levels can lead to agricultural and climatic risks (Bars, Akbay & Uçum, 2016).

Hydrological impacts arise from changes in the river's flow regime and physicochemical parameters. As water transitions from the river to the lake, the natural purification capacity decreases due to reduced water velocity, diffusion, and oxygen uptake capacity, and the lake enters the eutrophication process due to the nitrogen-phosphorus load from the river. Changes in lake water quality alter both the aquatic life within the lake and the downstream aquatic ecosystems, as well as water usage patterns (Çeliker & ark., 2019).

Ecological impacts arise from the physical structure of a reservoir-type HPP blocking migration routes, submerging habitats, and resulting in the decline of certain key species. At first glance, the reduction of fish and plant species and the emergence of new species may be balanced by the economic benefits of energy production. However, in the long term, the potential impacts of this situation on natural ecosystems should be carefully examined, and measures should be taken to minimize these effects (Aydın, 2019).

Socioeconomic and cultural impacts emerge from the construction phase of a reservoir-type HPP and are felt, either positively or negatively, throughout the lifespan of the plant. During the construction phase, the land that is submerged and the scale of the land expropriation process lead to internal and external migration, and the value of the land changes. Additionally, the demand for labor during the construction phase stimulates the local economy, and infrastructure services, particularly in integrated projects, have a positive impact on social services (Oğuz, 2016; Üçüncü & Demirel, 2020).

The storage component of a hydropower plant also serves as a resource for recreation and aquaculture production. However, the inability to preserve the natural and historical assets in the region leads to the loss of cultural values. In this context, the budget for hydraulic energy production facilities should include provisions for the preservation, protection, and/or documentation of these cultural assets. The existence of projects such as the Aswan and Atatürk dams in the world and in our country highlights the scale of the issue and points to the need for measures to be taken depending on the nature of the project (Kocabaş & ark., 2013; Üçüncü & Demirel, 2020).

The methods for mitigating the impacts of hydropower plants worldwide primarily vary in terms of downstream water usage rights, as well as considering the protection of downstream water quality and aquatic life, and the preservation of cultural heritage, all of which are incorporated into the project design (Kocabaş & ark., 2013).

The most significant impact of river-type power plants during the operation phase is on aquatic life. In these types of plants, all necessary technical measures must be taken to protect fish species. If these measures are not implemented in a timely and proper manner, the survival of fish species may be adversely affected (Alkan, Birinci & Bulut, 2022).

The most significant impact of river-type power plants on aquatic life is the reduction of water in certain sections of the river, and even the complete drying up of the riverbed, due to the diverted stream flows. As a result, there may be ecological changes in the species that rely on these sections of the river. In this context, habitat loss may occur due to the reduced water levels in specific parts of the river, and these sections may become inaccessible to fish. To mitigate this, the first measures that should be taken include ensuring that natural water is left in the riverbed and the construction of fish passages. Additionally, fish breeding stations for endangered species should be established in suitable locations, and illegal fishing activities should be controlled (Yılmaz & ark., 2012).

Although there are many sources in the global literature regarding the environmental measures of hydraulic plants, adapting the technologies used to the specific conditions of our country on a "one-to-one" basis is not easy. However, based on the general principles of these technologies, projects can be designed that are suitable for the country's conditions.

Conclusion

In conclusion, hydroelectric energy ranks first among renewable energy sources and is a high-potential renewable energy resource. In this context, assuming that all environmental precautions are taken, when compared to coal based thermal, nuclear, and hydraulic energy production facilities, it is observed that hydraulic plants remain the cleanest technology, followed by nuclear, natural gas, and coal-fired thermal power plants, respectively. However, when planning resources, the contribution of these facilities to meeting demand, their construction periods, and lifespans are significant factors. The accepted energy policy for the future, however, should focus on preventing natural resource and environmental waste, including all factors in planning and project development, with the environmental aspect also considered. Thus, during the establishment phase of hydroelectric energy investments, all necessary precautions should be taken to minimize potential environmental damage.

References

Aydin, F. (2019). Yenilenebilir enerji kaynaklarının Türkiye’de kullanımı ve sürdürülebilirliği (Master's thesis, Sosyal Bilimler Enstitüsü).

Alkan, S., Birinci, S., & Bulut, İ. (2022). Nehir Tipi HES’lerin Çevresel Etkilerine Bir Örnek: Katıklı Çayı Havzası. Dünya Coğrafyası ve Kalkınma Perspektifi Dergisi, 1(2), 44-54.

Bars, T., Akbay, C., & Uçum, İ. (2016). Türkiye’de Hes’ lerin varlığı, çevreye ve tarıma olan etkileri. 12. Ulusal Tarım Kongresi, 25-27.

Bülbül, S. E., & Çokluk, Y. (2017). Türkiye’de Gelişen Enerji Sektörü Hes’ler Ve Kâr Kaybı Sigortaları. Finansal Araştırmalar ve Çalışmalar Dergisi, 9(17), 89-114.

Çeliker, M., Öztürk, M., Parlakyıldız, N., & Güler, C. (2019). Çevresel İzotoplar (Δ18o, Δd Ve 3h) Kullanılarak Hazar Gölü Havzası Yeraltı Suyu Sisteminin Karakterizasyonu. DSİ Teknik Bülteni, (134), 26-36.

Çevik, S. N. (2022). Suyun Metalaşması Bağlamında Türkiye’de Hidroelektrik Santraller: Fındıklı Örneği. İşletme Ekonomi ve Yönetim Araştırmaları Dergisi, 5(2), 397-410.

Dinçer, F., Atik, İ., Yılmaz, Ş., & Çıngı, A. (2017). Hidrolik enerjisinden yararlanmada ülkemiz ve gelişmiş ülkelerin mevcut durumlarının analizi. Dicle Üniversitesi Mühendislik Fakültesi Mühendislik Dergisi, 8(3), 555-561.

DPT, S. (2001). Elektrik Enerjisi Özel İhtisas Komisyonu Raporu. DPT Yayını, Ankara.

Erkin, E. (2019). Yenilenebilir enerji kaynaklarının kullanımı ve Karabük ili hidroelektrik enerji potansiyelinin araştırılması (Master's thesis, Fen Bilimleri Enstitüsü).

https://enerji.gov.tr/bilgi-merkezi-enerji-hidrolik Erişim Tarihi: 02 Aralık 2024.

https://www.academia.edu/9125385/H%C4%B0DROELEKTR%C4%B0K_SANTRALLER%C4%B0N_%C3%9CST%C3%9CNL%C3%9CKLER%C4%B0_Hidroelektrik_Santrallerde_Termik_Santrallerde?email_work_card=view-paper Erişim Tarihi: 03 Aralık 2024.

https://avys.omu.edu.tr/storage/app/public/atalayt/105461/Hidroelektrik%20Santraller.pdfErişim Tarihi: 04 Aralık 2024.

Kenet, S. (2020). Türkiye'de Hidroelektrik Santrallerin Çevresel ve Ekonomik Değerlendirmesi, Marmara üniversitesi Sosyal Bilimler Enstitüsü.

Kocabaş, M., Başçınar, N., Kutluyer, F., & Aksu, Ö. (2013). HES'ler ve Balıklar. Türk Bilimsel Derlemeler Dergisi, (1), 128-131.

Koçak, M. E. (2011). Yenilenebilir enerji kaynakları, hidroelektrik santraller ve sırakonaklar HES projesi. Yayımlanmış Yüksek Lisans Tezi). Kayseri: Erciyes Üniversitesi Fen Bilimleri Enstitüsü.

Oğuz, S. P. (2016). Trabzon solaklı vadisi: Ogene halklarının HES'lere karşı mücadelesi. Aksu, C. Erensü, S. ve Evren, E.(Der.), Sudan Sebepler: Türkiye’de Neoliberal Su-Enerji Politikaları ve Direnişler, İstanbul: İletişim Yayınları.

Olgun, H. (2009). Küçük hidroelektrik santraller. Bilim ve Teknik, 498, 50-53.

Onüçyıldız, M., Büyükkaracığan, N., & Erkmen, M. E. (2013). Küçük Hidroelektrik Santrallerin Enerji Potansiyelleri ve Çevresel Etkileri. Selçuk Üniversitesi Sosyal ve Teknik Araştırmalar Dergisi, (6), 37-59.

Oral, F., Behçet, R., & Aykut, K. (2017). Hidroelektrik santral rezervuar verilerinin enerji üretimi amaçlı değerlendirilmesi. *Bitlis Eren Üniversitesi Fen Bilimleri Dergisi*, 6(2), 29-38.

Özbay, E., & Gençoğlu, M. T. (2009). Hidroelektrik santrallerin modellenmesi. Yenilenebilir Enerji Kaynakları Sempozyumu, 19-21.

Özdemir, O., Özaydın, Ö., & Yılmaz, V. (2023). Hidroelektrik Santrallerin Kabulüne Etki Eden Faktörlerin Araştırılması: Van Yüzüncü Yıl Üniversitesi Erciş Meslek Yüksekokulu Öğrencileri Örneklemi. Süleyman Demirel Üniversitesi Fen Bilimleri Enstitüsü Dergisi, 27(3), 447-456.

Serencam, U. (2007). Doğu Karadeniz Bölgesindeki küçük akarsuların hidroelektrik potansiyellerinin analizi (Master's thesis, Sakarya Universitesi (Turkey)).

Süme, V., & Fırat, S. S. (2020). Hidroelektrik Santraller ve Rize İlinde Bulunan Hidroelektrik Santrallerin Şehir ve Doğu Karadeniz Havzası İçin Önemi. *Türk Hidrolik Dergisi*, *4*(2), 8-23.

Şahin, A. (1989). Enerji Üretiminde Nükleer Enerji Alternatifi. İstanbul Üniversitesi İktisat Fakültesi Mecmuası, 47(1-4).

Şavkar, E. (2024). Yenilenebilir Enerji Zemininde Hidroelektrik Enerji Ve Türkiye Potansiyeli. Oğuzhan Sosyal Bilimler Dergisi, 6(1), 51-58.

Şenpınar, A., & Gençoğlu, M. T. (2006). Yenilenebilir Enerji Kaynaklarının Çevresel Etkileri Açısından Karşılaştırılması. Fırat Üniversitesi Doğu Araştırmaları Dergisi, 4(2), 49-54.

Tüylüoğlu, E. H., & Türkan, N. Nükleer Güç Santrallerinin Çevresel Etkileri. OHS ACADEMY, 6(1), 50-58.

Üçüncü, O., & Demirel, Ö. (2020). HES Projelerinin Olumsuz Çevresel Etkileri Üzerinde Alınacak Önlemler Ve Koruma Eylemleri, Kılıçlı Regülatörü Ve HES Projesi Örneği. Türkiye Peyzaj Araştırmaları Dergisi, 3(1), 31-39.

Yılmaz, C., Uzun, A., Zeybek, H. İ., & Kaya, M. (2012). Nehir Tipi Hidroelektrik Santrallerinin Coğrafi Ortam Üzerine Etkilerine Bir Örnek: Ayancık HES. Nature Sciences, 7(3), 50-67.

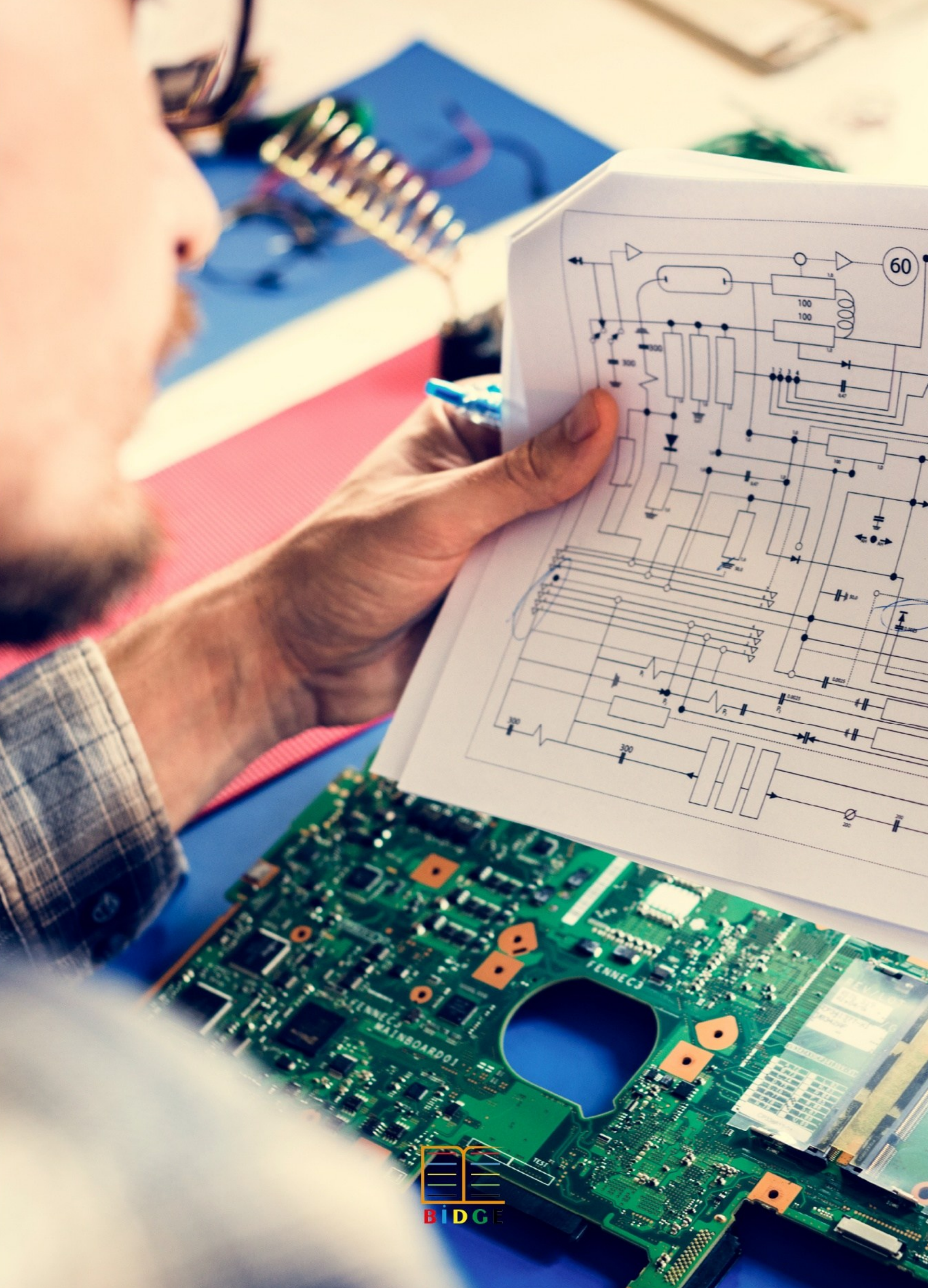
60
100
100
FENNEC3
BIDGE